Raman and EXAFS Studies of the Low-Doped Superconductor $YBa_2(Cu_{(1-x)}Ni_x)_3O_{(7-\delta)}$

by

Michael C. Baxa

Honors Thesis Submitted in Partial Fulfillment of the Departmental Requirements for the Illinois Centennial Honors College

Department of Physics
Western Illinois University
May, 2002

This Honors thesis by Michael C. Baxa is approved in its present form by the Department of Physics at Western Illinois University as satisfying the requirements for graduation as a Physics Honors Scholar.

_____
Dr. Mark S. Boley, Honors Thesis Advisor

_____
Date

Abstract

A comparative study of the results of Raman spectroscopy and Extended X-ray Absorption Fine Structure (EXAFS) spectroscopy, along with in-field critical current density determinations, was performed to ascertain the structural changes associated with low levels of nickel doping in polycrystalline $YBa_2Cu_3O_{7-\delta}$ (YBCO). Four samples were doped with molar-proportional percentages (0.32%, 0.64%, 0.96%, and 3.3%) of Ni (nickel) replacing the Cu (copper) in the starting materials, along with a control sample of pure YBCO. The Raman spectra were collected over multiple averaged scans with a GaAs PMT and a Triax 550 spectrometer equipped with a holographic Super-Notch Plus filter and were excited with 150 mW of 514.5 nm argon-ion laser radiation at the sample surface. The Raman studies indicated the increasing presence of NiO impurity in the sample as the doping level increased, but also clearly indicated that some of the Ni substitutes in the Cu sites of the Cu-O chains in the material, breaking their symmetry and allowing them to become Raman-active. This finding is especially significant in view of the fact that earlier studies in the literature have been inconclusive as to the exact site of the substituting Ni atoms. This effect is largest in the sample with the lowest dopant level (0.32%), which also demonstrated the optimal enhancement of the in-field transport critical current density for the lower field ranges. The EXAFS spectra were collected using the Advanced Photon Source (APS) at Argonne National laboratory, and exhibited little, if any detectable changes in the local atomic structure across the three lowest doped samples, but did exhibit a peak of increasing intensity with higher doping levels that indicated the increasing presence of NiO impurities, and delineating the reason for the drastic reduction in critical current densities for the larger nickel doping levels.

Table of Contents

List of Figures

Figure Page

Chapter 2. Theory and Present Work in High-T_c Superconductors

Chapter 3. Sample Preparation and Experiment

Chapter 4. Discussion of Results

List of Tables

1. Introduction

1.1. Motivation

Since the discovery of superconductivity above liquid nitrogen temperatures, $YBa_2Cu_3O_{7-\delta}$ has been one of the most thoroughly investigated systems [1]. The fact that impurity phonons can be easily observed in the Raman spectra of materials serves as a natural motivation to study the optical properties of nominally pure materials in comparison to materials into which impurities have been selectively doped. In addition, it is primarily because of some of the magnetic effects occurring below T_c that many optical studies of impurities in $YBa_2Cu_3O_{7-\delta}$ have focused on nickel doping.

One of the primary concerns for potential applications of high-T_c superconductors is the enhancement of the relatively low critical transport current density (J_c). Several experiments at WIU have focused on studying the effects of low-nickel doping on the J_c of $YBa_2Cu_3O_{7-\delta}$ polycrystalline superconductors. Several earlier studies conducted elsewhere have predicted a wide range of values of the suppression of T_c with *x*, and these have also likely contributed to the uncertainty of the substitution site for Ni in Y-123. We have recently carried out Raman scattering measurements in our spectroscopy laboratory on several sets of low-doped samples along with a control sample, all of which were produced in our sample preparation laboratory. Furthermore, Extended X-ray Absorption Fine Structure (EXAFS) spectroscopy measurements have been conducted on the Ni-doped Y-123 samples during a summer (2000) internship at the advanced photon source at Argonne National Laboratory, near Chicago, Illinois.

In addition, we have analyzed the Raman-active electronic spectra and compared them with the previous literature to obtain further knowledge about the physical properties and how the phonons are affected by the crystalline and chemical structure, and the temperature, which was primarily done by a graduate student in our research group, No Soung Myoung. We also hope to learn how much of the Ni actually incorporates into the structure and to further pin-point its location, or to identify any NiO impurities and their location.

1.2. History of Conventional and High-T_c Superconductivity

1.2.1. History of Conventional Superconductivity

Superconductivity was first discovered in 1911 by the Dutch physicist, Heike Kammerlingh Onnes, who initiated the field of low-temperature physics by liquefying helium below 4 K in his laboratory. Onnes investigated the electrical properties of metals at extremely low temperatures. It was well-known that the resistance of metals dropped when cooled below room temperature, but it was not known what limiting value the resistance would approach if the temperature were reduced to near 0 K. Some scientists, such as William Kelvin, had previously believed that electrons flowing through a conductor would come to a complete halt as the temperature approached absolute zero. However, Onnes found that below 4.5 K, the dc resistance of mercury dropped to zero [2]. In 1913, lead was found to be superconducting at 7.2 K. In 1933, Meissner and Ochsenfeld found that the magnetic field is completely expelled from the interior of the superconductor, in contradiction with the classical expectation [3]. But other scientists, like Onnes, now felt that a cold wire's resistance would dissipate. The theory of Landau

and Ginzburg in 1950 developed the theoretical properties of superconductors. It described superconductivity in terms of an ordering parameter and a highly ordered phase transition, and provided a derivation for the London equations as will be shown in one of the following sections (**1.2.3**). The transition temperature was observed to decrease as the average isotopic mass increases, as was predicted theoretically by Herbert Frohlich [4], and then was later discovered experimentally by E. Maxwell [5].

Three American physicists, John Bardeen, Leon Cooper, and Robert Schrieffer, won the Novel prize in physics in 1972 for the development of a model that electrons in a superconductor condense into a quantum ground state and travel together collectively. This theory of superconductivity is now well-known as the BCS theory. In 1986, Georg Bednorz and Alex Műller were experimenting with a particular class of metal oxide ceramics called perovskites, such as $YBa_2Cu_3O_{7-\delta}$. They found indications of superconductivity at 35 K, a startling 12 K above the previously established record for a superconductor. In 1987, a perovskite ceramic material was found to superconduct at 90 K [6]. These materials are referred to as high temperature superconductors because they enter the superconducting state at much higher temperatures than the conventional superconductors discovered prior to 1986.

1.2.2. BCS Theory

In 1957, Bardeen, Cooper, and Schrieffer explained the occurrence of superconductivity and predicted its properties in elemental superconductors. Two electrons near the Fermi level could couple to form an effective new particle, even under a very weak attractive force. This attraction leads to the formation of the Cooper pair [7].

BCS theory predicts the instability of the normal state of an otherwise free electron gas. BCS theory also predicts that the electron gas is unstable to the formation of a coherent many-body ground state in the presence of an attractive interaction between electrons. This does not provide a description of the superconducting state, however, or even demonstrate that superconductivity exists at all. The interaction of two electrons due to lattice dynamics occurs by virtue of the Coulomb attraction to the ions in the lattice and is mediated via phonons.

A second electron can experience the disturbance created by a first and then reacts in a way to reduce the potential energy, thus causing an effective attraction which overcomes the Coulomb repulsion between the two electrons. As a result of the Pauli exclusion principle, the electrons cannot all inhabit the states of lowest kinetic energy because they are already occupied by other electrons. In conventional superconductors, the mechanism for pair formation is thus the electron-phonon interaction, but other mechanisms are also possible, for instance, polarons or excitons [8].

In addition, the BCS theory predicts that, first of all, the energy gap E_g between the BCS ground state and the first excited state is proportional to the transition temperature. Second, it predicts that the energy gap E_g is the minimum energy required to create a single electron excitation from the superconducting ground state. And third, the London equations arise as a natural consequence of BCS theory, which allows for a state of perfect diamagnetism to exist below T_c with $\chi = -\frac{1}{4\pi}$ (CGS), or $\chi = -1$ (SI), where χ is the magnetic susceptibility that the Meissner effect implies.

1.2.3. London Equation

The Meissner effect also implies that superconductivity will be destroyed by a critical magnetic field H_c, which is related thermodynamically to the free-energy difference between the normal and the superconducting states in the zero-field state. F. London and H. London, who proposed two equations to govern the microscopic electric and magnetic fields, described the basic electrodynamic properties of superconductivity in 1935. We can write the London equations (1–1) and (1–2) as

$$\vec{E} = \mu_0 \lambda_L^2 \frac{d}{dt} \vec{J} \tag{1–1}$$

$$\vec{B} = -\mu_0 \lambda_L^2 \vec{\nabla} \times \vec{J} \tag{1–2}$$

where $\lambda_L \left(= \sqrt{\frac{m^* c^2}{4\pi n_s q^2}} \right)$ is the London penetration depth, n_S is the density of superconducting electrons which would have an upper bound of the total density of conduction electrons, and m^* is the effective mass of the electron. Since the superconducting transition is a continuous transition, the density of superconducting electrons will be directly related to the order parameter for the superconductor, and hence the London penetration depth will be temperature dependent [3].

These two equations give a current density for the induced supercurrents which decreases exponentially with the distance into the bulk of the superconducting sample. Hence, the induced current density is mostly restricted to the surface of the sample.

2. Theory and Present Work in High-T_c Superconductors

2.1. Meissner Effect

Superconductivity can be defined as a state of perfect diamagnetism. The perfect diamagnetism of the material implies that the superconducting material does not permit an externally applied magnetic field to penetrate into its interior. For instance, the Type-II superconductors which we measured, $YBa(Cu_{1-x}Ni_x)_3O_{7-\delta}$, are both perfect conductors of electricity as well as perfect diamagnets in their superconducting state. They totally exclude magnetic flux when the applied magnetic field is low, but only partially exclude it when the magnetic field becomes higher. In addition, if the field is applied after the sample has been cooled below its critical temperature, the magnetic flux is excluded from the superconductor [9]. Hence, a superconductor acts like a perfect diamagnet. Both Meissner effects are shown in Fig. 2-1. This phenomenon is called the Meissner effect and was discovered by Meissner and Oschenfeld in 1933. It was also found that $\mathbf{H}_c$, the critical magnetic field strength, is quite well approximated by a parabolic law as can be seen in Fig. 2-2 (a), and is given as a function of temperature, $\mathbf{H}_c(T)$, as follows :

$$H_c(T) \cong H_c(0)\left[1 - \left(\frac{T}{T_c}\right)^2\right] \qquad (2\text{–}1)$$

where $\mathbf{H}_c(0)$ is the critical magnetic field at 0 K. While the transition in zero field at T_c is of second order, the transition in the presence of a field is of first order since there is a discontinuous change in the thermodynamic state of the system and an associated latent heat [10].

FIGURE 2-1. The Meissner effects are shown with (a) changing temperature and (b) changing field.

(a) Holding **H** Constant while Decreasing T

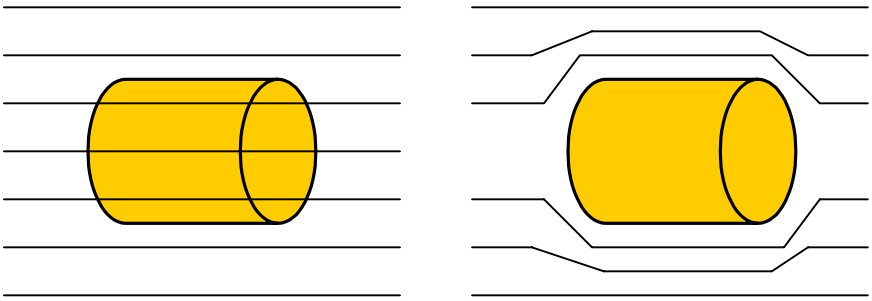

$H \neq 0, T > T_c$ **$H \neq 0, T < T_c$**

(b) Holding T Constant while Increasing **H**

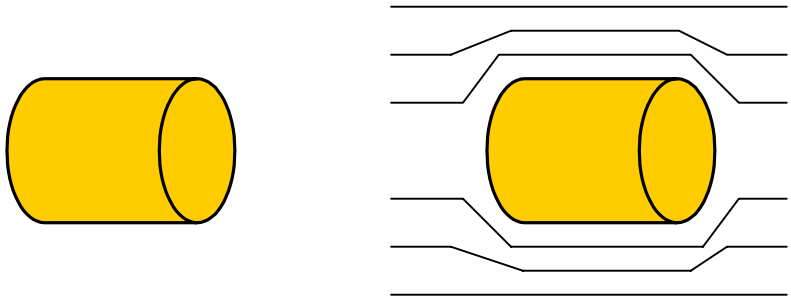

$H = 0, T < T_c$ **$H \neq 0, T < T_c$**

In Fig. 2-2(a), the critical magnetic field strength $\mathbf{H}_c$ depends on the temperature, decreasing when the temperature is raised and falling to zero at the transition temperature T_c. It is known that the flux density **B** outside the sample is always equal to $\mu_0\mathbf{H}$, where **H** is the magnetic field strength, so we may equally well refer to the critical magnetic field strength, $\mathbf{H}_c$, as a critical magnetic flux density, $\mathbf{B}_c$, given by the equation

$$H_c = \frac{B_c}{\mu_0} \tag{2–2}$$

where μ_0 is the permeability of free space. Furthermore, a Type-I superconductor remains superconducting throughout its whole interior when a magnetic field of strength less than $\mathbf{H}_c$ is applied [11].

In Fig. 2-2(b), when a gradually increasing magnetic field is applied to a Type-II superconductor, it goes into the mixed state at a "lower critical field", $\mathbf{H}_{c1}$, less than $\mathbf{H}_c$. A Type-II superconductor in the mixed state has, however, a lower free energy than if it were Type-I. Therefore, a magnetic field stronger than $\mathbf{H}_c$ must be applied to drive a Type-II superconductor normal. The highest magnetic field strength up to which the mixed state can persist in a Type-II superconductor is known as the upper critical field, $\mathbf{H}_{c2}$ [11].

In our research, the critical current density (J_c) for the $YBa(Cu_{1-x}Ni_x)_3O_{7-\delta}$ was measured with most of the applied magnetic field (**H**) values in the range between $\mathbf{H}_{c1}$ and $\mathbf{H}_{c2}$ which implies that our sample was in the vortex (intermediate) state during the majority of the experiment to determine $J_c(\mathbf{H})$.

FIGURE 2-2. Simplified magnetic phase diagrams showing Type-I and Type-II superconductors are depicted below (Note that H_c is zero when the temperature T equals the critical temperature T_c).

(a) Magnetic Phase Diagram showing the Superconducting State for Type-I.

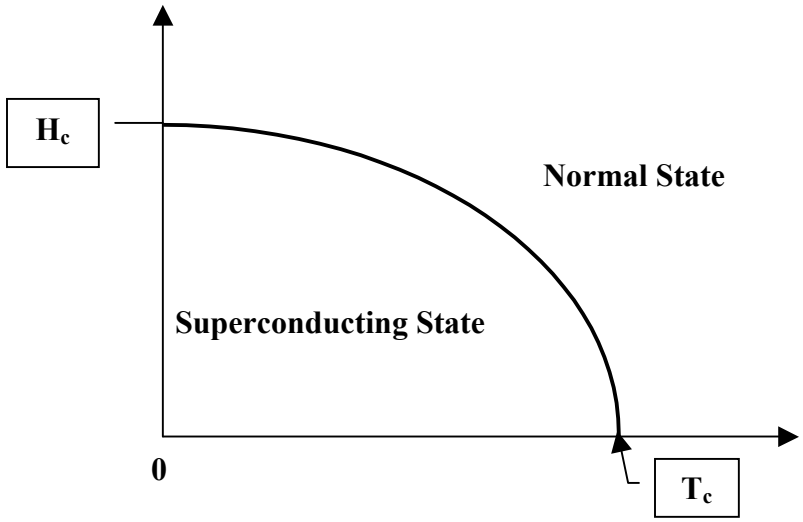

(b) Magnetic Phase Diagram showing the Vortex State and the Superconducting State (Meissner state) for Type-II.

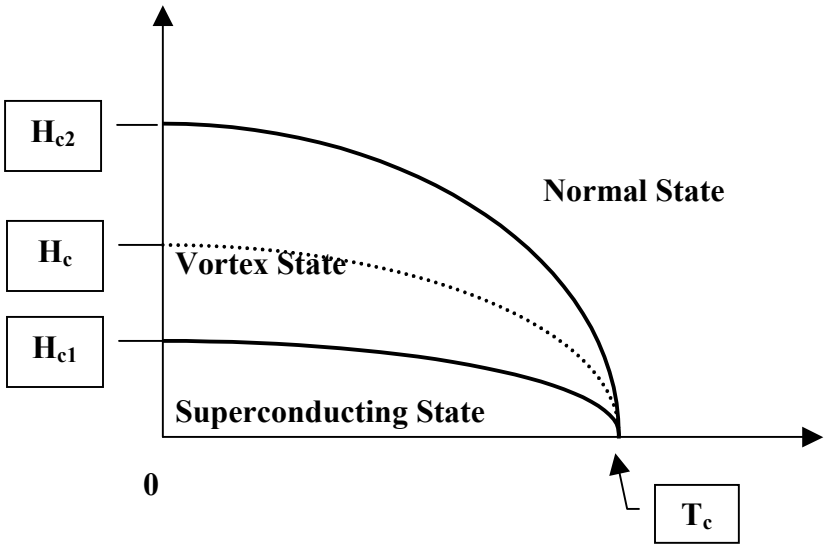

2.2. Critical Temperature (T_c) and Critical Current Density (J_c)

Superconducting metals and alloys have a characteristic transition temperature, at which they undergo the conversion from a normal conductor to a superconductor, which is called a critical temperature, T_c. Although the theoretical transition from the normal to the superconducting state can be very sharp, experimentally it sometimes occurs more or less gradually and sometimes quite abruptly. Below the transition temperature the resistivity of a sample is zero. The sharpness of the drop to zero resistivity can prove as a good relative measure of the purity of the sample and its level of oxygenation, and its structural integrity. On the other hand, narrow and broad superconducting resistivity transitions have both been seen to depend primarily on the level of sample oxygenation. However, it is also clear that when high temperature superconductors are doped with paramagnetic ions at the copper sites, that the transition temperature both shifts to lower values and also broadens.

When the critical current in a sample exceeds a value that is called the critical current density, J_c, the superconductivity is destroyed. This is called the Silsbee effect [8]. If too much current is applied to a superconducting sample, it will revert to the normal state even though it is yet below its transition temperature at zero current. Therefore, we can say that the critical current density is a function of the temperature, as well as of the externally applied magnetic field.

In addition, the value of critical current density increases from zero at $T = T_c$ to a maximum value, $J_c(0)$, at $T = 0$ K. As the samples are cooled down through and below the transition temperature, T_c, the critical current density gradually increases. The explicit

temperature dependence of J_c on T is given by the Ginzburg-Landau theory. This temperature dependence takes the form of the following equation,

$$J_c = J_c(0)\left[1-\left(\frac{T}{T_c}\right)^2\right]\left[1-\left(\frac{T}{T_c}\right)^4\right]^{\frac{1}{2}} \qquad (2\text{–}3)$$

and is plotted in Fig. 2-3.

2.3. Theory of Extended X-ray Absorption Fine Structure (EXAFS)

EXAFS is actually one region of x-ray absorption fine structure (XAFS) studies. XAFS spectroscopy is concerned with the probability that a x-ray will be absorbed by an atom. When a x-ray photon is absorbed, the photon's energy is transferred to a core electron that becomes an excited photoelectron. This excited photoelectron is then promoted from a ground state to a higher energy level [12]. The energy at which the probability of absorption is greatest is known as the absorption edge for the particular electron. For electrons in the n = 1 shell (the most tightly bound shell), the edge is known as the K-edge, and for the n = 2 shell, there are corresponding L-edges, as well as M-edges for the n = 3 shell [13,14]. This absorption edge is also the binding energy of this electron, and therefore the absorption of the x-ray photon results in the ejection of the excited photoelectron from the atom [12,14]. In most XAFS measurements the most basic information learned is the absorption coefficient of the material. The derivation of the coefficient is actually straightforward starting with the fact that as a collimated x-ray with intensity *I* is transmitted through a material of thickness *X*, the loss in intensity is a function of the intensity and the change in thickness, or:

FIGURE 2-3. This is the temperature dependence of the critical current density $J_c(T)$ in accordance with Eq. (2–3).

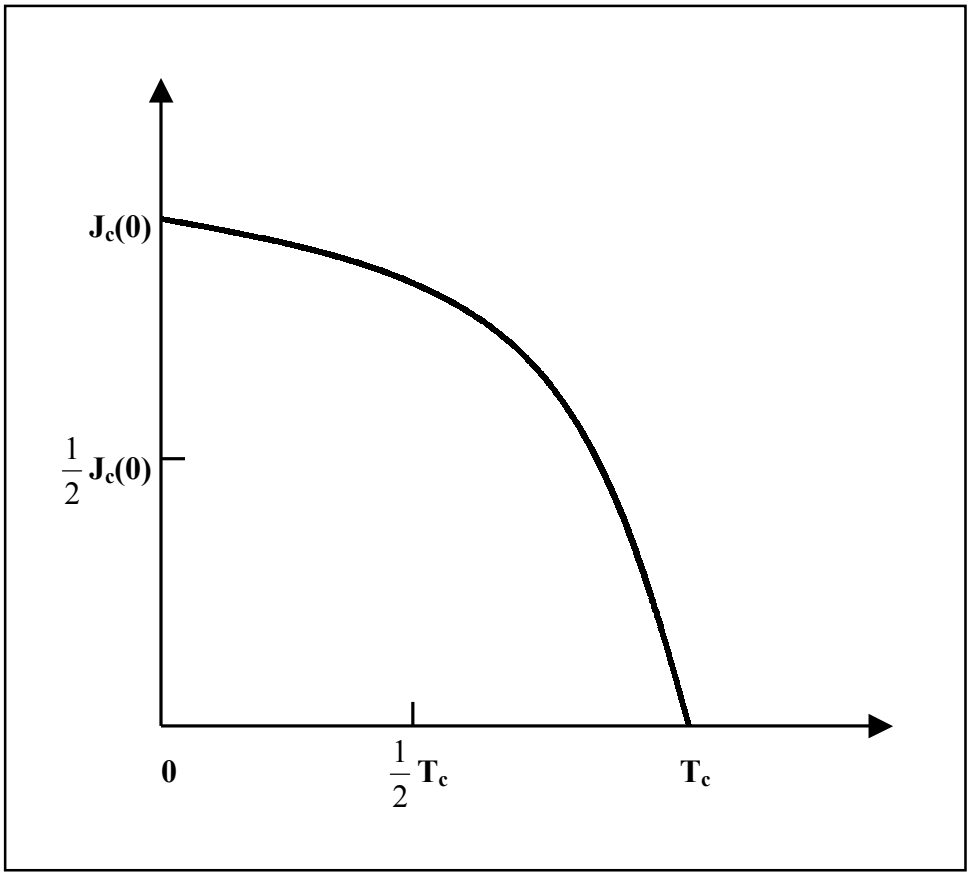

$$dI = -\mu I dx \tag{2–4}$$

$$\frac{I}{I_0} = e^{-\mu X} = T \tag{2–5}$$

where T is the transmission through the material. μ serves as a constant of proportionality, and is defined as the linear absorption coefficient in units of cm^{-1}. However, μ is dependent on the density of the material as well. To make up for this, the absorption coefficient is often referred to as the mass absorption coefficient. For a given material with mass density ρ, the mass absorption coefficient is defined by $\frac{\mu}{\rho}$ and has units of $\frac{cm^2}{g}$. In actuality, this constant is not 100% independent of the physical state of the material but for all practical purposes it is close enough. The constant $\frac{\mu}{\rho}$ can be approximated with the summation:

$$\frac{\mu}{\rho} = \sum_j g_j (\frac{\mu}{\rho})_j \tag{2–6}$$

where g_j represents the mass fraction of the element *j* that has a mass absorption coefficient $\left(\frac{\mu}{\rho}\right)_j$ [13]. Regardless of its actual approximation, the mass absorption coefficient is considered to be the standard constant used in XAFS measurements.

At a point past the absorption edge, there begins a fine structure that extends for usually another 1000 to 1500 eV further. This fine structure is the EXAFS region, and on a plot of the x-ray absorption coefficient vs. photon energy, this region is depicted as a line oscillating with a pseudoperiod and amplitude that gradually fades away [12-14]. Information about the local neighborhood surrounding the absorbing atom can be derived

using numerical methods that have been developed over and over throughout the entire existence of EXAFS studies. H. Fricke [15] and G. Hertz [16] were first to discover the presence of a fine structure past the absorption edge of materials. At the time, there was no way to explain quantitatively this fine structure that extended so far past the edge.

The first explanation incorporated quantum mechanics by Kronig [17]. However, his explanations depended on the long-range order (LRO) of the material. This LRO theory eventually proved to be incorrect [18], but Kronig did develop a short-range order (SRO) theory that worked from the molecular level of the material [19]. The theory that he proposed captured the basic physics behind EXAFS, which will be explained later, but was lacking some of the modern theory. Petersen [20] took Kronig's SRO theory and made adjustments by proposing that the potentials of the excited atom and backscattering atoms would cause a phase shift in the photoelectron wave function. Kostarev [21] was the first to note that what Petersen and Kronig proposed in molecules could be carried over into condensed matter. One remaining issue at this point was the lifetime of the electron. Obviously there was a limit as to how far the electron would interact, and Sawada *et al* [22] resolved this issue as well as to calculating of the lifetime of the core hole state in the late 1950s using the concept of mean free path. The theory of EXAFS was finally resolved by Schmidt [23] in 1961 and 1963 reports where he explained a Debye-Waller type factor to correct for disorder due to thermal vibrations among backscattering atoms [14].

Even though the theory behind EXAFS had been worked out, confusion still existed in applying it experimentally. The main problem was that, for the most part, the theory did not match up with experimental results. What gave the SRO theory

difficulties was not what it stated, but rather it was the inaccurate atomic parameters that were entered into the theory for calculations. Because of the disagreement between theory and experiment, EXAFS remained nothing more than a scientific enigma. However, Sayers *et al* [24] proposed an idea in 1971 that has since become the key to converting EXAFS into a quantitative field of science. Sayers *et al* stated that if one were to take a Fourier transform of the EXAFS with respect to the photoelectron wave number, *k*, the resulting plot would show peaks that in fact related to the distances of the nearest-neighbor coordination shells of atoms. This quantum leap allowed scientists to use EXAFS directly to find local structure information and to experimentally calculate the necessary atomic parameters. The Fourier transform also verified the EXAFS theory in that it is a SRO theory because the transform only shows the first few nearest neighbor shells of atoms [14].

The practicality of EXAFS was increased dramatically with the use of synchrotron radiation. By the mid-1970s, synchrotron sources could produce x-rays three decades or greater in intensity as those produced using standard x-ray tube sources. Because of these more brilliant sources, the time required to measure the spectrum of a concentrated sample went from a week [25] to a matter of minutes [26]. In addition to this, the higher brilliance allowed for more dilute samples to be measured that could not have been measured before the synchrotron [14]. In fact, this experiment requires measuring the Ni-edge in a sample that has at most 0.96% concentration of Ni (relative to Cu). Fortunately, the measurements could be performed at the Advanced Photon Source at Argonne National Laboratory, which produces the most brilliant x-rays in the United States. EXAFS as a science is so effective that it has begun to be used in the past decade

to study the local environment of materials with long-range order, for example, crystals. The power of EXAFS became apparent when it was able to detect the presence of local distortions in crystals going through structural phase transitions. Researchers believe that it is these distortions that are responsible for these structural and possibly other phase transitions [12].

Since EXAFS does not occur with isolated atoms, but rather for condensed clusters or groups, the basic physics for it goes beyond that of the previously described atomic absorption. EXAFS focuses on how the ejected photoelectron interacts with the nearest-neighbor atomic shells. If one assumes that all of the x-ray photon's energy is transferred into one core electron, then the ejected photoelectron has kinetic energy that is the difference of the photon energy and the core electron's atomic binding energy. The EXAFS region does not begin usually until 15 eV or more beyond the edge, because then the photoelectron will have enough kinetic energy to be measurable from the inter-atomic interaction energy that is approximately 3 eV [14]. The ejected photoelectron can be of course treated as a wave using the basic de Broglie relation:

$$\lambda = \frac{h}{p} = \frac{hc}{E} \tag{2–7}$$

where h is Planck's constant, p is the momentum of the photoelectron, and E is the energy of the x-ray photon. The momentum p can also be expressed in the EXAFS region by:

$$\frac{p^2}{2m} = h\nu - E_0 \tag{2–8}$$

where ν is the frequency of the incident x-ray, and E_0 represents the electron's atomic binding energy. The absorbing atom would have coming out of it a spherical wave. Backscattering occurs when the outgoing wave interacts with the surrounding atoms, and the outgoing wave is scattered in such a way that the surrounding atoms produce spherical waves of their own. The backscattered waves will interfere either constructively or destructively with the initial outgoing wave depending on the relative phase difference. The change in amplitude of the electron will cause a change in the probability of x-ray absorption. As the energy changes in the EXAFS measurement, obviously the wavelength will change inversely, which will in turn change the relative phases between the outgoing wave and the backscattered waves. Therefore, the amplitude changes, which changes the overall probability of absorption. In a plot of absorption vs. energy, this process is reflected by the periodic oscillations in the EXAFS region. The peaks correspond to the outgoing wave being in phase with the backscattered waves, while the valleys reflect out of phase waves. The diagram in Fig. 2-4 is a recreation of a simple Stern [14] model that shows the outgoing electron wave from the absorbing atom interacting with neighboring atoms and the creation of backscattered waves as well.

The basic EXAFS equation is an approximation that describes $\chi(k)$, which is approximately the difference of the actual absorption and the absorption of the embedded probe atom that is normalized to the smooth atomic absorption [12], e.g. $\chi(k)$ is the oscillation or interference in the absorption defined by:

$$\chi(k) = \sum_{\Gamma} \frac{S_0^2}{kR_\Gamma^2} \left| f_{eff}^{\Gamma}(k) \right| \sin\left[2kR_\Gamma + \phi^{\Gamma}(k) + 2\delta_c(k)\right] e^{-2\sigma_\Gamma^2 k^2} e^{-2R_\Gamma/\lambda(k)} \qquad (2\text{–}9)$$

Figure 2-4: Stern model of EXAFS with outgoing and backscattered waves

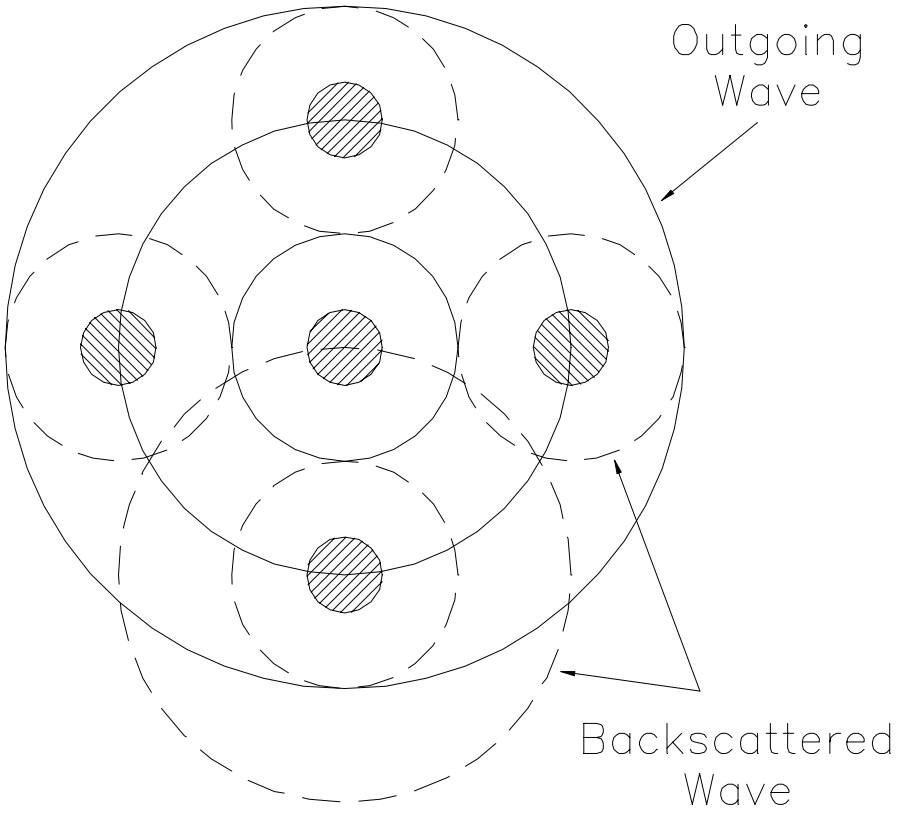

where the summation includes all possible scattering paths Γ. The change in the passive electron overlap is factored in with an amplitude correction of S_0^2. As can be seen, χ is a function of the photoelectron wave number k, which can be defined by $\lambda = \frac{2\pi}{k}$. This equation, along with equations (2–7) and (2–8), gives us the equation for the energy ($E = h\nu$) of the incident x-ray photon as:

$$\hbar k = \sqrt{2m(E - E_0)} \tag{2–10}$$

where E_0 is the core electron's atomic binding energy. R represents half of the scattering path length, while $|f_{eff}|$ accounts for the effective scattering amplitude. The phase shift in the electron wave is factored in by ϕ, and δ_c adjusts for the probe atomic phase shift. Finally, the error adjustment through the mean squared relative displacement (MSRD) is added using σ^2, while λ is, of course, the photoelectron's coherent wavelength [12]. One can note that $\chi(k)$ is essentially a summation of sine functions, with different amplitudes for each sine function. Therefore, the beauty of the Fourier transform with respect to k becomes more and more apparent. In an EXAFS experiment, once one finds $\chi(k)$, it is relatively straightforward to arrive at the distances of the nearest-neighborhood shells of atoms, and this is why EXAFS has become a popular method for investigating the structure of a material.

2.4. Theory of Raman Spectroscopy

The Indian physicist, C.V. Raman, discovered the Raman effect, which can yield important information about molecular quantum states and material phonon modes, in 1928. This is the scattering of light by molecules with a resulting frequency change, that

is, the visible wavelength of a small fraction of the radiation scattered by certain molecules differs from that of the incident light. If the incident radiation is fairly intense and is monochromatic light of ultra-violet, visible, or infrared frequency ν, it is found that the scattered light contains not only radiation of frequency ν (Rayleigh scattering), but also weaker radiation of frequency ν ± ν' (Raman scattering). The frequency difference ν' between the incident and the scattered light in the Raman effect, as shown in Fig 2-5, is characteristic of vibrational transitions in the scattering molecule, or of the phonon mode energies associated with a particular material's structure [27].

The energy difference between the initial and final vibrational levels, or the Raman shift in wave numbers (cm^{-1}), is calculated through equation (2–11),

$$\nu = \frac{1}{\lambda_i} - \frac{1}{\lambda_s} \tag{2–11}$$

where λ_i is the incident photon wavelength of 514.5 nm in all cases, and λ_s is the Raman scattered photon wavelength. The vibrational energy is ultimately dissipated as heat. Because of the low intensity of Raman scattering, the heat dissipation does not cause a measurable temperature rise in most samples.

The important features of the Raman scattering intensity can be explained by the classical electromagnetic field associated with the incident wave in Raman spectroscopy. An electric dipole moment, **P**, is induced within a molecule when an electromagnetic wave having an electric field **E** is impinging upon the molecule. This induced dipole moment **P** is proportional to the field as shown in equation (2–12),

$$\mathbf{P} = \alpha \mathbf{E} \tag{2–12}$$

FIGURE 2-5. Energy level diagram for Raman scattering is shown below.

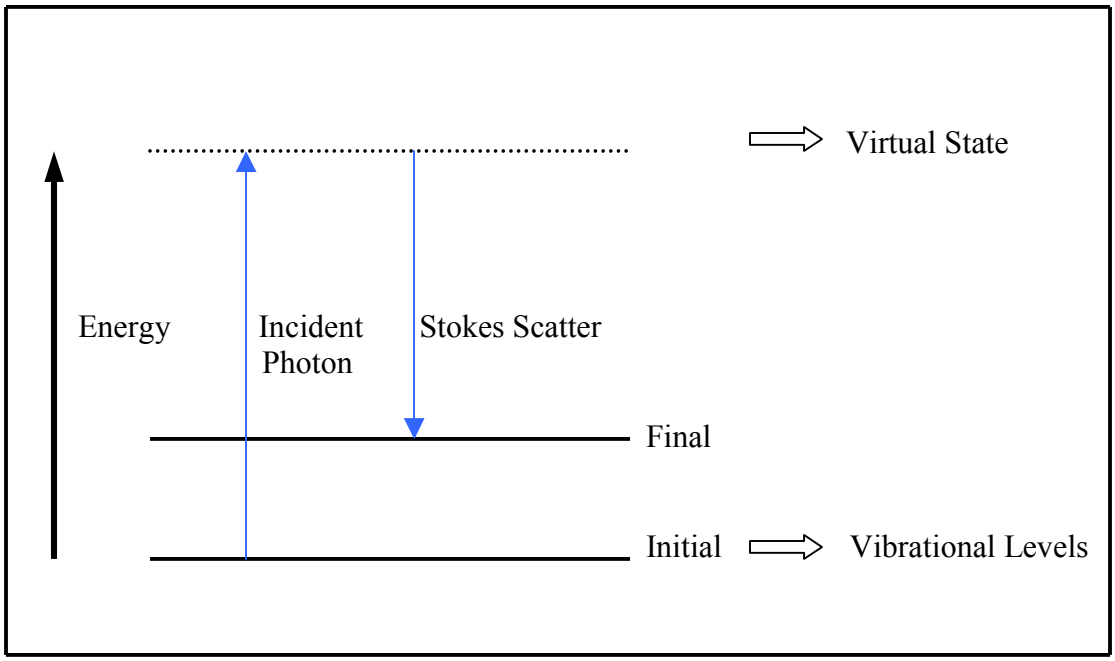

where α is the polarizability of the molecule [27]. The induced dipole scatters light at the optical frequency of the incident light wave. Then, Raman scattering occurs because a molecular vibration could change the polarizability. In general, the molecular polarizability will be a function of the nuclear coordinates of the molecule. Hence, the change in the polarizability, α', is written by the polarizability derivative,

$$\alpha' = \frac{\partial \alpha}{\partial Q} \tag{2–13}$$

where Q is the normal coordinate of the vibration.

This equation implies that the relationship between the **P** and the **E** vectors can be placed into the matrix form,

$$\begin{pmatrix} P_x \\ P_y \\ P_z \end{pmatrix} = \begin{pmatrix} \alpha_{xx} & \alpha_{xy} & \alpha_{xz} \\ \alpha_{yx} & \alpha_{yy} & \alpha_{yz} \\ \alpha_{zx} & \alpha_{zy} & \alpha_{zz} \end{pmatrix} \begin{pmatrix} E_x \\ E_y \\ E_z \end{pmatrix} \tag{2–14}$$

This symmetric matrix represents $\alpha_{xy} = \alpha_{yx}$, $\alpha_{xz} = \alpha_{zx}$, and $\alpha_{yz} = \alpha_{zy}$. The directional relationship between **P** and **E** is determined by non-zero polarizability components. From the point of view of classical electromagnetism, the electromagnetic field can be expressed in terms of the linear induced electric dipole.

$$\overline{P} = \overline{P}(\nu_0) + \overline{P}(\nu_0 - \nu_k) + \overline{P}(\nu_0 + \nu_k) \tag{2–15}$$

These three frequency components are present in this molecular dipole, and give rise to radiation from the dipole at the excitation frequency ν_0 (Rayleigh scattering) as well as to radiation frequency shifted by an amount ν_K on either side of the excitation frequency (Raman scattering). As also shown in equation (2–15), the frequencies on the right hand

side imply the presence of Stokes Raman scattering at frequency (ν_0 - ν_K), and the presence of anti-Stokes Raman scattering at frequency (ν_0 + ν_K). Only the former has been analyzed in our experiments, because normally the anti-Stokes radiation is of much lower intensity by an amount of the Boltzman thermal factor, and can only be observed under rare circumstances and usually at high temperatures.

In addition, the molecular polarizability, as a function of the nuclear coordinates of the molecule, can be presented in terms of a Taylor series expansion. The polarizability of the xy component can be described by:

$$\alpha_{xy} = (\alpha_{xy})_0 + \sum_k \left(\frac{\partial \alpha_{xy}}{\partial Q_k} \right)_0 Q_k + \frac{1}{2} \sum_{kl} \left(\frac{\partial^2 \alpha_{xy}}{\partial Q_k \partial Q_l} \right)_0 Q_k Q_1 + ... \qquad (2\text{–}16)$$

where associated with vibration k, l,… are normal coordinates Q_k, Q_l,…, that describe the vibration with their derivative taken at their equilibrium position, Q_0. Hence, if the vibration produces a change of the molecular polarizability, i.e., if $(\frac{\partial \alpha}{\partial Q}) \neq 0$, then it will be active in the Raman spectrum. This implies that even if the particular crystalline lattice symmetry provides a number of possible normal modes of vibration (phonon modes), only a fraction of these will be Raman-active and exhibit corresponding peaks in the Raman scattering spectra of the material.

3. Sample Preparation and Experiment

3.1. Sample Preparation

In order to produce a control sample of pure $YBa_2Cu_3O_{7-x}$, we weighed the stoichiometric amount of each component that was needed for ½ mole of Y_2O_3, 2 moles of $BaCO_3$, and 3 moles of CuO. The reaction formula for $YBa_2Cu_3O_{7-\delta}$ is then given as,

$$\frac{1}{2}Y_2O_3 + 2BaCO_3 + 3CuO \quad \rightarrow \quad YBa_2Cu_3O_{7-\delta} + CO_2 \uparrow$$

This amounted to 1.12896 grams of Y_2O_3, 3.946663 grams of $BaCO_3$, and 2.386182 grams of CuO. The pure $YBa_2Cu_3O_{7-\delta}$ was synthesized under the same conditions as the doped samples to ensure that the oxygen composition x remained the same and that the nickel concentration was the only parameter responsible for any structural changes. The other samples were doped with low molar-proportional percentages (0.32%, 0.48%, 0,64%, 0.96%, 3.3%) of nickel replacing the copper. The amounts of each sample are summarized as can be seen in Table 1.

We then ground the ingredients with the mortar and pestle until they were in the form of a uniform fine gray powder by passing through a 90 μm filter. This mixture of the ingredients was then placed in an alumina crucible, and underwent a first heat treatment in the high-temperature furnace for 3 hours at 930 ^oC. This was followed by a slow cooldown to room temperature with the furnace power shut off. The homogeneous dispersion of gray particles became black in color following the high-temperature chemical reaction with decreasing amounts of unreacted greenish-black patches following the second and third heat treatments, which were identical to the first treatment but helped to ensure a more complete and thorough reaction of all components.

TABLE 1. The stoichiometric amounts of each component are measured by an electric scale as below.

	Y_2O_3 (225.792g/mol)	$BaCO_3$ (197.33315g/mol)	CuO (79.5394g/mol)	NiO (74.7094g/mol)
0.00%	1.12896g	3.946663g	2.386182g	0
0.32%	1.12896g	3.946663g	2.383796g	0.002241g
0.48%	1.12896g	3.946663g	2.376168g	0.007165g
0.64%	1.12896g	3.946663g	2.360960g	0.014284g
0.96%	1.12896g	3.946663g	2.338295g	0.021289g
3.30%	1.12896g	3.946663g	2.261131g	0.070086g

Intermediate re-grindings of the sample helped to ensure maximal surface exposure to sufficient oxygen. Then, the YBCO samples doped with molar-proportional percentages of nickel, including the control sample, were measured out in amounts of 0.35 grams each and a steel ram and die with a 0.25 inch diameter was then used to fabricate the pellets. Pressure was then applied via the hydraulic press up to 4000 psi. When we removed the pellets from the die, they were usually quite brittle; therefore, great care was required in the removal. We fabricated five pellets for each compound, and then placed them into a crucible for sintering. The final pelletized samples of the polycrystalline superconductors were then obtained by sintering for 4 hours at 950 degrees Celsius in air. The full oxygenation of the pellets was then ensured by a follow-up annealing in an oxygen-rich atmosphere for 18 hours at 400 degrees Celsius, immediately following the sintering process. For both of these processes, the quartz tube furnace was programmed for a heating and cooling rate of 120 ^{o}C per hour.

3.2. The Critical Temperature (T_c) and Critical Current Density (J_c) Measurement

For the measurements of the critical state parameters, we used the same samples as were prepared for the Raman scattering measurements. The dimensions of the sample pellets were 0.635 cm in diameter (1/4″) and of 0.15 cm thickness, yielding a cross-sectional area for current flow of 0.033 cm^2. In order to measure the electrical resistivity of the sample, four leads are electronically linked to the sample surface via mechanical pressure contacts. This four point probe, using mechanical pressure contacts, was designed in the WIU Physics Department Superconductivity Research Laboratory, and is

a very versatile device for the investigation of electrical phenomena in superconducting materials. A schematic of the four point probe is shown in Fig. 3-1. The four point probe device has been designed without any ferromagnetic parts to eliminate any potential interference. Typically, the resistance of the points of contact (the so-called contact resistance) is eliminated from the sample voltage measurement, since the voltage leads lie between the outside current supply leads. Our HP power supply has a digital readout of the current in amperes, as well as the supply voltage in mV necessary to maintain that level of current. The voltage drop across the inside voltage leads is measured by the Keithley digital nano-voltmeter. Then the device is placed inside a low temperature cryostat, between the poles of a large magnet, that allows for slow uniform cooling without contact of the sample with the liquid nitrogen. A constant 3 mA current is provided through the cross-section of the sample pellet, and the sample voltage is continuously monitored as the sample temperature is gradually lowered. Then *Ohm's Law,* $R = \frac{V}{I}$, is used to calculate the sample resistance R in *Ohms*. Then the sample resistivity, $\rho = \frac{RA}{L}$, where A is the cross-sectional area of the sample and L is the length between the voltage leads, is calculated and plotted as a function of the sample temperature. The resistance of the portion of the sample between the voltage probes is the ratio of the voltage registered on the voltmeter to the value of the output current of the power supply. The temperature dependence of resistivity for the pure Y-123 and the

FIGURE 3-1. This is a schematic of the four point probe to measure the critical temperature and the in-field critical current.

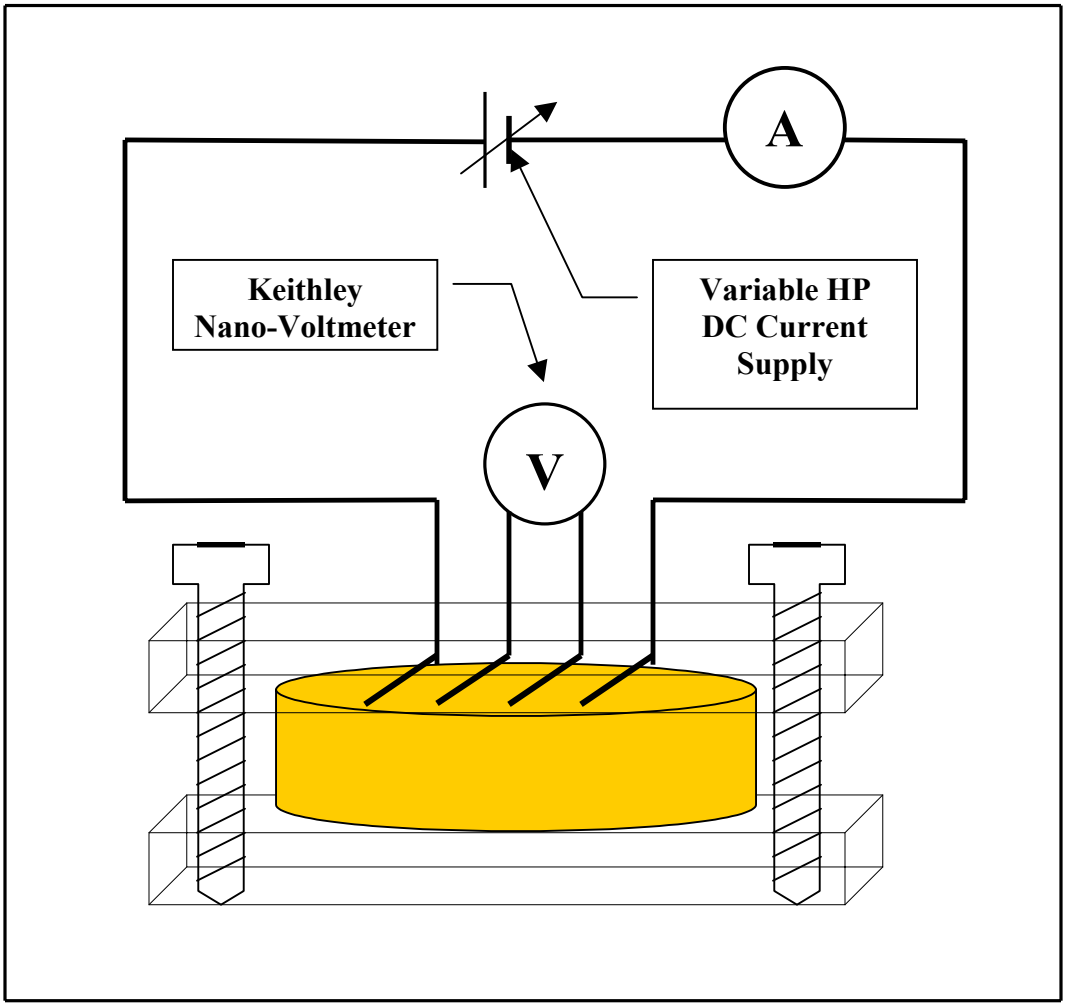

nickel-substituted $YBa_2(Cu_{1-x}Ni_x)_3O_{7-\delta}$ are all plotted by the computer from room temperature to the liquid nitrogen temperature of 77 K. Then the critical current density, as a function of the applied magnetic field of the superconducting materials, can also be measured using the same four point probe as described above. The critical current density, J_c, is an important parameter for the characterization of high-T_c superconductors, especially in determining their technological applications. The critical current, I_c, of a superconductor can be defined as the maximum current that the superconductor can carry at a particular value of temperature and applied magnetic field [28]. At each value of applied magnetic field, the current is automatically ramped by the HP-DC current supply under computerized control by a C^{++} program [29], until a transition to the non-superconducting state occurs. The measured I_c versus the magnetic field over the range of 0 to 12000 Gauss can then be recorded and plotted. Before plotting, the critical current density, J_c, is calculated by applying the formula, $J_c = \frac{I_c}{A}$, where A is the cross-sectional area ($A = 0.033\ cm^2$) of the pellet through which the applied current passed.

In order to measure the critical current associated with the presence of an externally applied magnetic field, a liquid nitrogen cryostat equipped with a 1.4 Tesla magnet has been used. A schematic diagram of the cryostat is shown in Fig. 3-2. The cryostat consists of an inner cylindrical sample chamber A surrounded by three chambers. Chamber A contains the four point probe with the sample, and both chamber A and B can be back-filled with helium gas to accelerate the warming or cooling processes. Chamber C is filled with liquid nitrogen to indirectly cool down the chamber A, thus allowing chamber B to play the role of insulating the chamber A, while chamber D is a

FIGURE 3-2. This is a schematic of the liquid nitrogen cryostat used for critical state measurements in the WIU physics department superconductivity research laboratory.

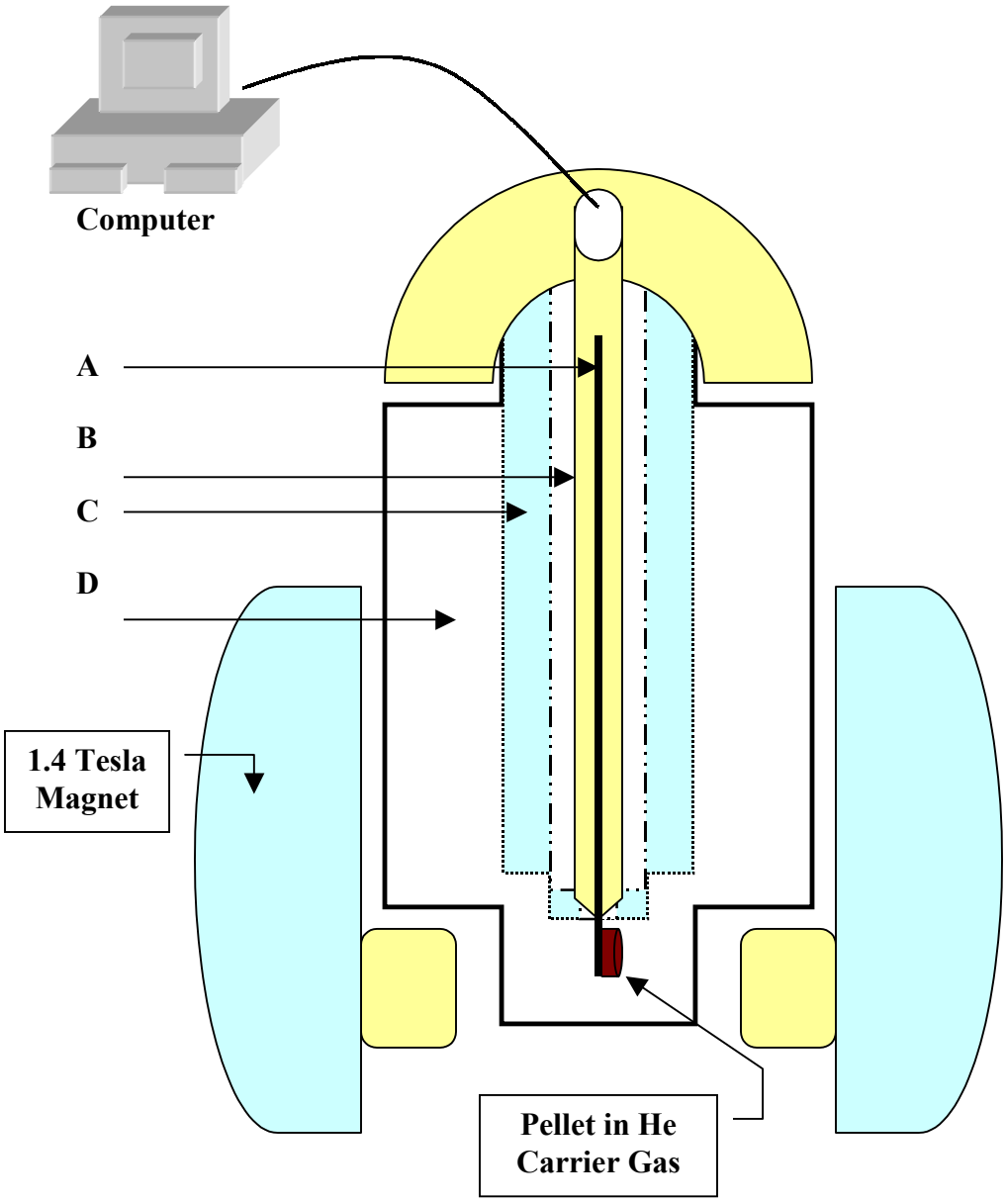

A : Sample Temperature (He Carrier Gas Vacuum)
B : Temperature Between Sample and Nitrogen (Vacuum / He Carrier Gas)
C : Liquid N_2
D : Vacuum

large vacuum jacket to insulate the liquid nitrogen in chamber C from the exterior. By continuously supplying liquid nitrogen into chamber C, the sample temperature of 77 K can be easily achieved. Then the temperature of 60 K as attained during part of our data collection process can be reached by using a large vacuum pump to produce a partial vacuum over a finite closed reservoir of the liquid nitrogen surrounding the sample cryostat, as chamber C is closed off and vacuum sealed.

3.3. EXAFS Measurement

3.3.1. Experimental Setup

In the EXAFS measurements, it was decided that the samples would be measured at the Ni-edge of 8.333 keV rather than the Cu-edge at 8.979 keV because of the overwhelming amount of Cu versus Ni. It would be extremely difficult to detect the effects from the minute amount of Ni in the sample. Therefore, no EXAFS spectra of the undoped YBCO sample was recorded. The samples in the EXAFS measurements were not pressed into pellets, but rather left in powder form, because the pellets were unnecessary for the measurements. The final sintering and annealing cycle was excluded, as well, since this cycle would have no effect on the local atomic environment of the samples.

Prior to the preparation of the samples, it had been determined that the $YBa_2Cu_3O_{7-\delta}$ was itself too dense. In order for the transmission to be between 33% and 66% the samples would have to have a thickness on the order of 10 μm [30]. This that been done by using equations (2–5) and (2–6) and some algebra to find the linear absorption coefficient for $YBa_2Cu_3O_{7-\delta}$. Unfortunately, the mass absorption coefficient

for YBCO could not be found. However, it was possible to use the additive nature of the linear absorption coefficient. All that was necessary was to find the linear absorption coefficient for the Y, Ba, Cu, and O. In an undoped molecule of $YBa_2Cu_3O_{7-\delta}$ there were 13 atoms present (assuming $\delta = 0$). Multiplying the mass density of $YBa_2Cu_3O_{7-\delta}$ by the fractional amount of each element in the $YBa_2Cu_3O_{7-\delta}$ would yield the mass density of each element in the molecule. The mass absorption coefficients for the elements were found in reference tables for energies around the Ni-edge (8.333 keV), and using (2–5) resulted in the linear absorption coefficient for each element present. Table 2 shows these values along with the densities calculated as well as the reference mass absorption coefficients. All the elements' values were found for 9 keV except for Cu, because it goes through its edge at 8.979 keV. Once past the edges, its absorption increases dramatically. Incidentally, the EXAFS measurements had to be cut short due to the Cu-edge. Rather than measuring for another 1000 eV past the edge, measurements went out to only about 8.9 keV.

The next step was to determine the thickness of a Ni-doped $YBa_2Cu_3O_{7-\delta}$ sample such that the transmission changed by 20% at the Ni-edge. It was believed that this would still be enough of a change in signal to acquire measurements. The 0.32% sample was chosen for this calculation as it contained the most dilute amount of Ni. Using the same process above, two values of the Ni linear absorption coefficient were calculated, one pre-edge (0.261 cm^{-1}) and one post-edge (1.5 cm^{-1}). The following system of

TABLE 2. These are the fractional densities of the total density and absorption coefficients.

	Y (1/13)	Ba (2/13)	Cu (3/13)	O (7/13)	$YBa_2Cu_3O_{7-\delta}$
Proportional Constant [μ (cm^{-1})]	38	217	64.6	23	343
Mass Density [ρ (g/cm^3)]	.423	.846	1.27	2.96	5.5
Mass Absorption Coefficient [μ/ρ (cm^2/g)]	89.72	256.5	50.85	7.747	---

equations was produced using T and X as the respective transmission and sample thickness:

$$T = e^{-43X} \tag{3–1}$$

$$.8T = e^{-330X} \tag{3–2}$$

It was not noticed till later that an error had been made in writing these equations. The mass absorption coefficient values had been substituted into the equations rather than the linear coefficients. Using the incorrect coefficients had resulted in an ideal thickness of 7.8 μm, while the correct linear coefficients of 343.261 cm^{-1} and 344.5 cm^{-1} (pre-edge and post-edge respectively) yield a thickness of 1.8 mm, a much thicker sample. As large as this error was, it fortunately turned out to be a moot point for a couple of reasons. First of all, this algebraic process had been to find at what thickness did a *change* in the transmission occur at the Ni-edge, which ignored then what the actual transmission was before and after the edge. Using (2–5) and the correct coefficients, it turns out that the ideal thickness of 1.8 mm would have resulted in a change in transmission from 1.47E-27 to 1.17E-27. Even though this is a 20% change in the transmission, there would have been not enough signal to make an adequate measurement. The other reason why this error is not as severe as it should have been, and for that matter why it was not noticed, is because the EXAFS measurements were performed using fluorescence rather than transmission, for which the reason will be explained later. When the x-rays strike a material, some of the photons are transmitted while some are absorbed by exciting a core electron. The transition back to the ground state results in fluorescence. In fluorescence measurements, the thickness of the sample is irrelevant.

The equipment setup for the EXAFS measurement was far from elaborate, which is another reason why EXAFS is an attractive method of study. Fig. 3-3 shows the basic schematic of the EXAFS equipment as they are arranged relative to one another. The detectors were Lytle ion detectors using Argon gas to fill the chamber. Adjustments in the energy were performed by a double crystal monochromator using (111) diamonds as its crystals. The mirror was rhodium, and the I_0 detector, where I_0 is the initial photon intensity, had cobalt filters which cut the beam intensity by about a factor of 3. As can be seen in Fig. 3-3, the sample holder was set at a 45° angle to the incident in order to somewhat reduce the intensity while also providing the opportunity for a fluorescence measurement.

Several methods were tried in placing the sample in the aluminum plates. The first method was similar to that of flouring a pan in baking where the powder was smeared onto the Kapton™ tape, and the excess powder was shaken off and discarded. However, this did not produce a uniform spread across sample holder. In addition to the sporadic holes, there was also a problem with the adhesive not holding onto the powder very well, which resulted in a thicker sample towards the bottom of the plate. A trial-and-error process then was done by simply pouring in certain masses, first with 100 mg. By this point, it was realized that the combination of higher than desired density and dilute presence of the metal being measured made it all but impossible to measure EXAFS via transmission. It was then decided to use fluorescence, which quickly resolved the problem in preparing the samples. The samples, one of which is shown in Fig 3-4, were prepared by placing a piece of Kapton™ tape over one side of the plate and

FIGURE 3-3. This is the schematic of the EXAFS equipment setup.

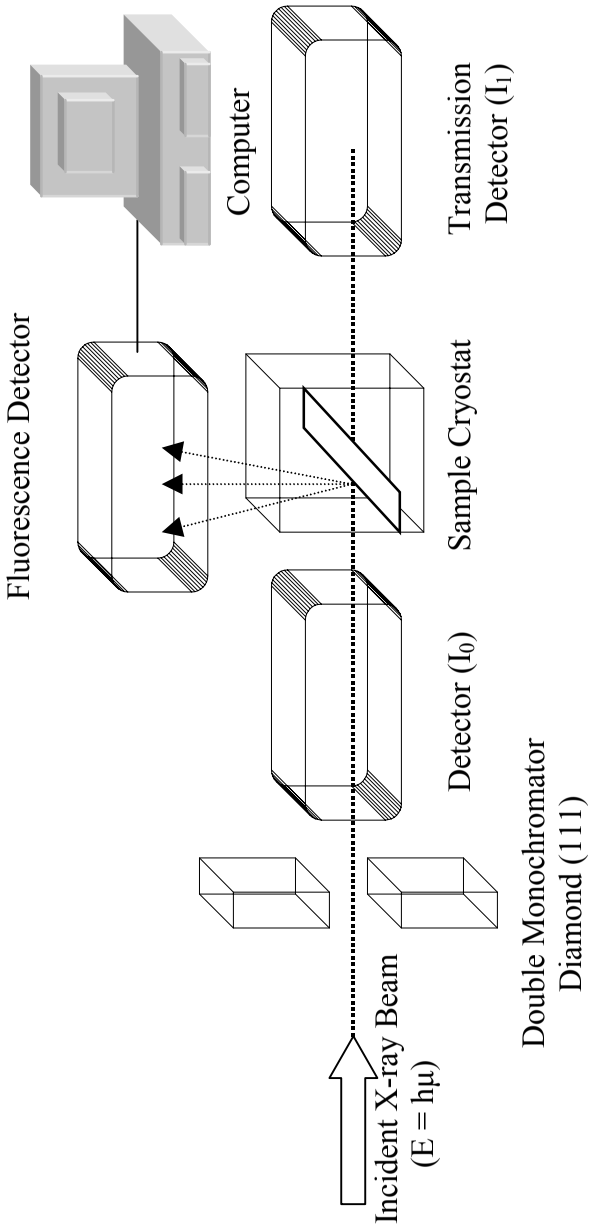

Figure 3-4: This is a picture of the Ni-sample trapped inside the holder plate by Kapton™ tape.

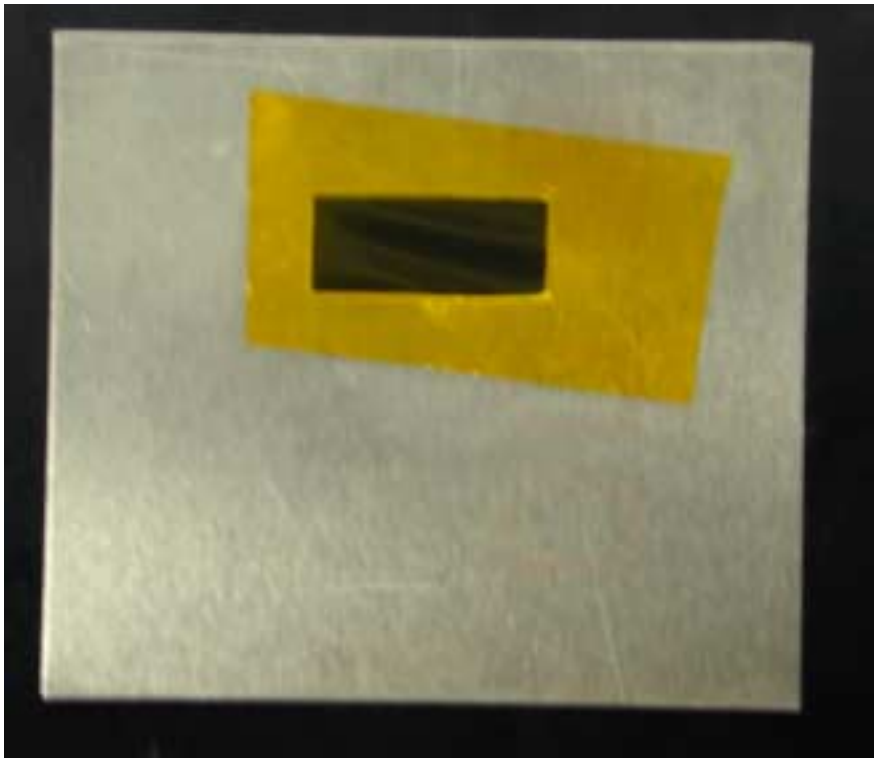

then pouring enough powder into the holder in order to be even with the plate. The other piece of Kapton™ tape was carefully placed over the sample, and the tape was manually pressed to try and even out the powder even further, while also maximizing on the amount of powder captured by the adhesive. It should be noted, though, that the 0.32% sample was thicker than the other two samples. This difference was neglected since the measurements were going to be performed with fluorescence.

3.3.2. Data Analysis

The experiment was run so that several measurements of each sample were made. Due to what appeared to be random noise, eight measurements for each sample were selected and then averaged together. This way, the random noise could be averaged out of the graphs. The data had been saved as an ASCII text file and then plotted in WinXAS 97 version 1.3, a program by T. Ressler, which was downloaded off the internet at http://ourworld.compuserve.com/homepages/t_ressler/. Figure 3-5 shows the various stages of the analysis in WinXAS 97v1.3 for the 0.32% Ni sample. Using WinXAS 97v1.3, the graphs for each sample were then analyzed. As the energy increased past the Ni-edge, it was approaching the Cu-edge, which resulted in the pre-edge of the Cu to begin to appear, hence the sudden curve at the end of the plot. To counter this, each graph was truncated resulting in a plot over an energy range of 8.2-8.8 keV.

In order to analyze the data, a few further statements should be made about the absorption spectra. Equations (2–4) and (2–5) are true for EXAFS using transmission. As it turns out, in fluorescence measurements, the relationship of absorption, intensity, and sample thickness are such that:

Figure 3-5: Stages of EXAFS analysis from (a) truncation and linear fitting, (b) two-polynomial fitting, (c) conversion to *k*-space, and (d) μ_0-fit of the χ function are shown below.

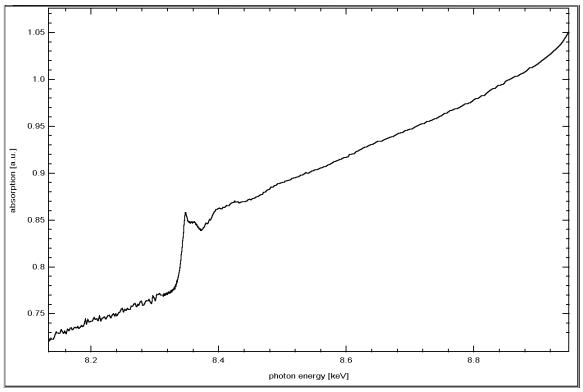

(a)

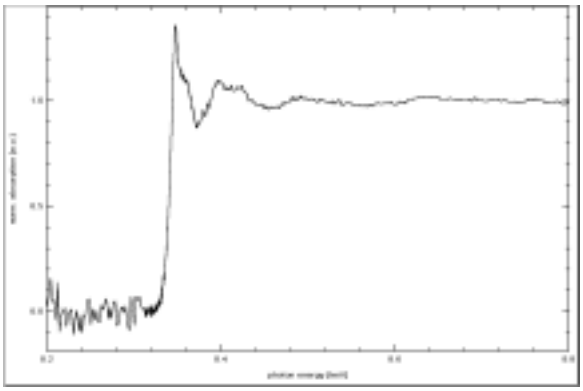

(b)

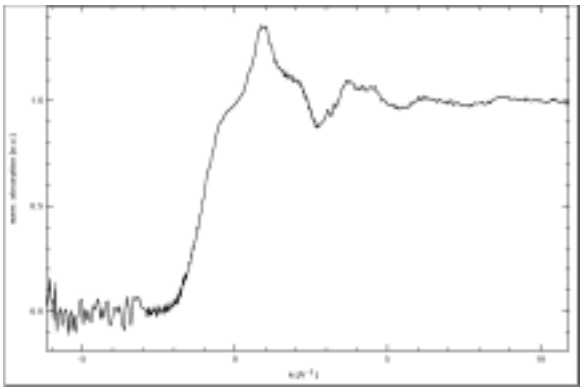

(c)

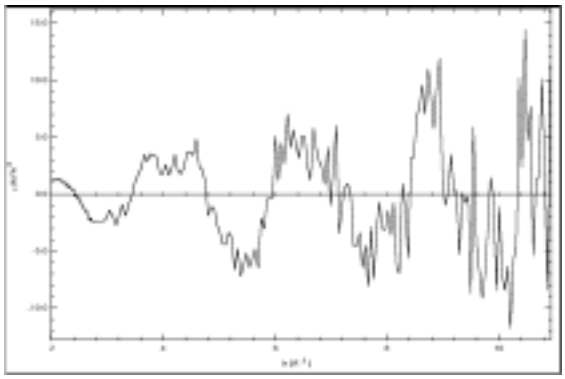

(d)

$$\mu(E)x = \frac{F}{I_0} \tag{3–3}$$

where $\mu(E)$ is the total linear absorption as a function of the energy E, x is the sample thickness, and F and I_0 are the respective fluorescence and initial intensities [13]. As can be seen in Fig. 3-5(a), an absorption spectrum has a general positive slope, which is typical of fluorescence measurements. As the energy increases, the x-ray photons are able to penetrate further into the sample thus producing an increase in fluorescence signal [13]. In addition to this, the 0.32% sample has a general absorption that is approximately twice that of the other two samples. This factor difference was attributed to the previously mentioned thickness difference between the samples. To resolve both of these problems, the plots must be normalized, where the edge jump is set equal to 1. WinXAS 97v1.3 is capable of selecting the edge for a given spectrum using the principle that the edge occurs at the inflection point along the spike, which is where, in a mathematical sense, a change in concavity occurs, e.g. the second derivative of a plot is equal to zero. WinXAS 97v1.3 is able to do this using two different methods, the first of which involves fitting a zero-order polynomial to a region past the edge, after which the program then normalizes the spectrum to the polynomial's ordinate value [31]. The other possible option is the one that was used in this experiment, and it is known as a two-polynomial fit. The degrees chosen for the polynomial were a 1st degree polynomial for the pre-edge, and a 3rd degree for the post-edge region. A section of the pre-edge is selected, and a line is then fitted to the region. Then, a cubic polynomial is fitted to a selected post-edge region. Afterwards, WinXAS 97v1.3 extrapolates the fitted line to extend across the entire graph, and then takes the difference between the two plots. Then,

WinXAS 97v1.3 normalizes to unity the resulting plot to the cubic polynomial fit [32], the result of which is shown in Fig. 3-6(b). The theory behind this process goes back to the fact that χ, the interference function as a function of E, is defined by:

$$\chi(E) = \frac{\mu(E) - \mu_0(E)}{\mu_0(E)} = \frac{\mu(E)}{\mu_0(E)} - 1 \qquad (3\text{–}4)$$

where $\mu(E)$ is the absorption measured experimentally, and $\mu_0(E)$ is the absorption that would be expected from an isolated atom and based on the experimental positioning of the edge [13]. Graphically, $\mu_0(E)$ would appear as a straight line of slope 0, after normalization, with a discontinuity at the absorption edge of the material. In other words, $\mu_0(E)$ past the edge graphically represents the equilibrium of the absorption oscillations, because it represents zero interactions physically. The χ function of interest is that of χ as a function of the wave number, k. Using equation (2–10), where $\hbar k = \sqrt{2m(E - E_0)}$ or approximately:

$$k = \sqrt{262.5(E - E_0^{\exp})} \qquad (3\text{–}5)$$

for k in $Å^{-1}$ and E in keV [13], the plots for each sample are converted from absorption vs. energy to $\chi(k)$ versus k. WinXAS 97v1.3 does this automatically, and the converted graph is shown in Fig. 3-6(c). The threshold or absorption-edge energies, E_0, that WinXAS 97v1.3 determined was 8.34483, 8.345125, and 8.345345 keV for the respective 0.32%, 0.64%, and 0.96% plots.

After conversion into k-space, the data can be fitted somewhat further in WinXAS 97v1.3 by using a $\mu_0(E)$-fit. In this analysis, an advanced form of the $\mu_0(E)$-fit was used where the k-space was divided into 3 sections and a 2nd degree spline is used in each

section with a *k*-weight of 3. The region for the fit was selected by using equation (3–5) along with the concept that EXAFS did not begin until approximately 0.015 keV past the edge [14], which resulted in a region beginning at $k = 1.984$. The $\mu_0(E)$-fit is to come as close as possible to running through the middle of the oscillations. The parameters chosen in the experiment yielded the best $\mu_0(E)$-fit possible for the data. Typically in EXAFS measurements, the resultant function, $\chi(k)$, consists of some oscillations that are very large in amplitude compared to other oscillations. To better view the interference function, scientists have developed a method by which $\chi(k)$ is multiplied by k^n where the *k* weight *n* is typically 1, 2, or 3. According to Teo and Lee [33], using a *k* weight of 3 works well for backscatterers in elements with atomic numbers less than 36 (nickel's is 28). Since the impending determination of atomic spacing and the Fourier transformation depends only on frequency and not amplitude, noting but graphical appearance is affected by *k* weighting [13]. After the $\mu_0(E)$-fit, WinXAS 97v1.3 is able to plot of $\chi(k)\cdot k^3$ vs. *k*.

The Fourier transform with respect to *k* results in peaks that correspond to the distances of the nearest-neighborhood shells of atoms. The transform for the weighted function $\chi(k)\cdot k^n$ from *k* space is defined by the integral over a maximum and a minimum value of *k* such that:

$$\rho_n(r') = \frac{1}{(2\pi)^{1/2}} \int_{k_{\min}}^{k_{\max}} w(k) k^n \chi(k) e^{i2kr'} dk \qquad (3\text{–}6)$$

where equation (3–6) is a modified radial distribution function $\rho_n(r')$ in space now defined by r'. However, Sayers, Stern, and Lytle discovered in 1971 that the resulting distances from Fourier transforms in early EXAFS meausurements did not agree with

known values for the atomic distances. What they discovered was that peaks in the Fourier transform had a common shift on the order of tenths of angstroms. It turns out that in $\rho_n(r')$, each distance peak is shifted by a distance α from the true distance *r*, where $\alpha = r - r' \approx 0.2 \sim 0.5$ Å. The peak shift α is dependent on the *k* weight, the elements in the measurement, the threshold energy E_0, as well as other parameters in the measurement [13]. In the summation for $\chi(k)$ in equation (2–9), the phase function $\phi(k)$ can be approximated as a linear function where $\phi(k) = p_0 + p_1 k$. In this case, the phase shift α would be $\alpha = p_1/2$. The phase shift is small enough such that it can be factored in later. The Fourier transform works best when $\chi(k) \cdot k^n$ is periodic, and therefore it is best if the graph of $\chi(k) \cdot k^n$ begins and ends at zero. For this reason, a window function ($w(k)$) is used where the endpoints of the window go to zero, thus making $\chi(k) \cdot k^n$ go to zero as well. A common window function, the Hanning function, was used in this analysis where $w(k)$ is defined as:

$$w(k) = \frac{1}{2}\left[1 - \cos 2\pi\left(\frac{k - k_{\min}}{k_{\max} - k_{\min}}\right)\right] \tag{3–7}$$

and one can see that for $k = k_{min}$ *or* k_{max}, $w(k) = 0$, which is the desired result [13].

3.4. The Raman Scattering Measurement

As mentioned in Section 2.1, the energy levels and transitions related to the Raman effect can be recorded via conventional Raman spectroscopy using visible lasers. Raman scattering has been extensively used to study the vibrational, electronic, and magnetic properties of high-temperature superconductors [34]. Many theoretical and experimental

studies of high temperature superconducting materials have been carried out in weakly doped materials [35-37]. We have studied the Raman scattering for pure and nickel substituted Y-123, that is, $YBa_2(Cu_{1-x}Ni_x)_3O_{7-\delta}$, which has an O-deficient perovskite structure whose superconducting properties depend critically on both x and δ, the latter of which approached zero in our case. In our experiments, as can be seen in the schematic of Fig. 3-6, the Raman scattering measurements were taken in a backscattering subtracted configuration utilizing the 514.5 nm line of an Argon-Ion Laser with an incident power of approximately 150 mW at the surface of our annealed superconducting pellets, which were mounted on the cold finger of a closed-cycle Leybold helium refrigeration system. The temperature stability during an experimental run was ±0.5°C and the temperature was monitored by the use of a Carbon-Glass Resistor. The scattered beam was analyzed by a TRIAX-550 (550 mm focal length) imaging spectrometer possessing a 0.025 nm specified resolution and equipped with a 1200 grooves/mm selective single diffraction grating, an air-cooled GaAs PMT (Photo-Multiplier Tube), and a holographic super-notch plus filter. The purpose of the super-notch plus filter was to shield out the unwanted background laser radiation, thus protecting the sensitive PMT, as well as increasing the signal-to-noise ratio for the data. The remaining specifications of the TRIAX –550 imaging spectrometer are provided in Table 3. Spectral data were taken in the superconducting phase of the material at a temperature of 20 K with an automated data collection system, utilizing a Spectra Max data acquisition device interfaced to a Gateway computer operating under a Lab-View software environment. Data thus collected were then analyzed and plotted according to their intensity as a function of their frequency shift in cm^{-1} from the incident laser line.

FIGURE 3-6. This shows a schematic of the Raman scattering experimental setup in the WIU physics department optical spectroscopy research laboratory.

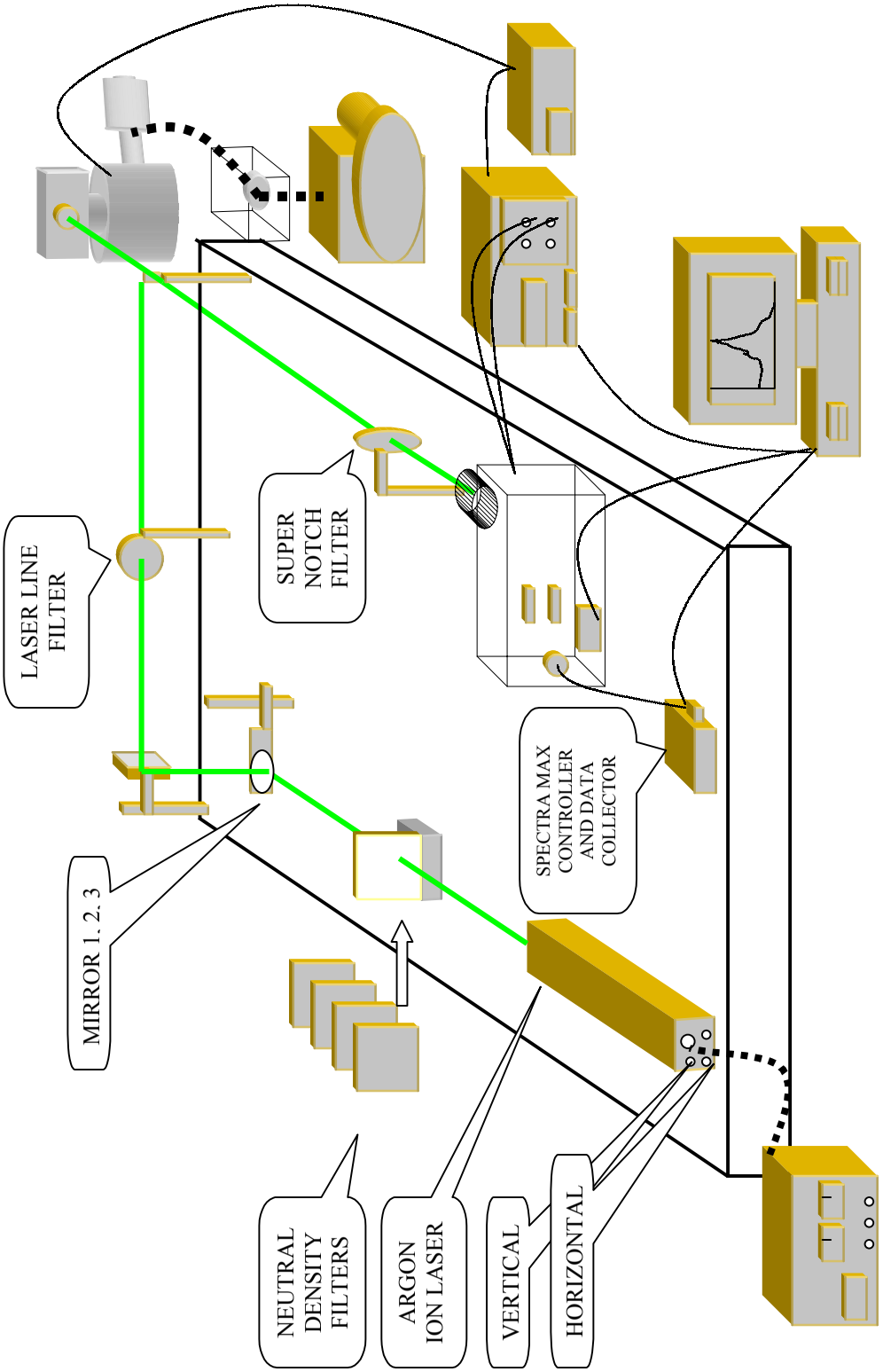

For the LabView Program used in the Raman Scattering Measurement, Fig. 3-7 depicts the spectral data collection program of LabView [38], which contains the information about the control system of the laser wavelength, the spectrometer scanning wavelength, and the detector settings. And Fig. 3-8 shows a diagram of the slit controller program that determines the widths of the axial entrance and exit slits of the spectrometer. In order to observe the sample temperature in the cold finger, a temperature monitoring program, as can be seen in Fig. 3-9, was constructed by Tom Boyle (an undergraduate student) and Laurie Pichla (a graduate student) in the WIU physics department. This environment is useful for obtaining and plotting the data from the spectrometer. LabView is a virtual instrument (VI) program, which utilizes a fully featured programming language G. It is a graphical language quite unique in the method by which code is constructed and saved. It plays a role in a diagrammatic view of how the data flows through the program. G is the "native" language of LabView, which is the code produced under the LabView system. The basic schematic as can be seen in Appendix A is that the passage of data through nodes within the program determines the order of execution of the functions of the program. LabView VI's have inputs, process data, and produce outputs. By chaining together VI's that have common inputs and outputs it is possible to arrange the functions in the order by which the programmer wants the data to be manipulated. Often a single input is used as a common "thread" running through several VI's and the program to force the order of operations.

TABLE 3. Specifications of the TRIAX –550 imaging spectrometer are below.

Focal Length	550mm
Spectral Range	0-1500nm mechanical range (1200g/mm grating) 0-40μm spectral range with appropriate gratings
Aperture	F/6.4
Dispersion	1.55nm/mm
Resolution	0.025nm(single channel)
Flat Field	30 x 15mm
Grating Turret	Triple automated on-axis grating turret
Accuracy	+/- 0.3nm
Repeatability	+/- 0.05nm
Slits	High precision motorized Optional motorised side entrance and exit slits
Dimensions	400 x 565 x 190mm
Control	Motorised with built in RS232/IEEE488 interfaces Windows or DOS software

FIGURE 3-7. This is a diagram of the spectral data collection program written in our laboratory operating in the LabView environment.

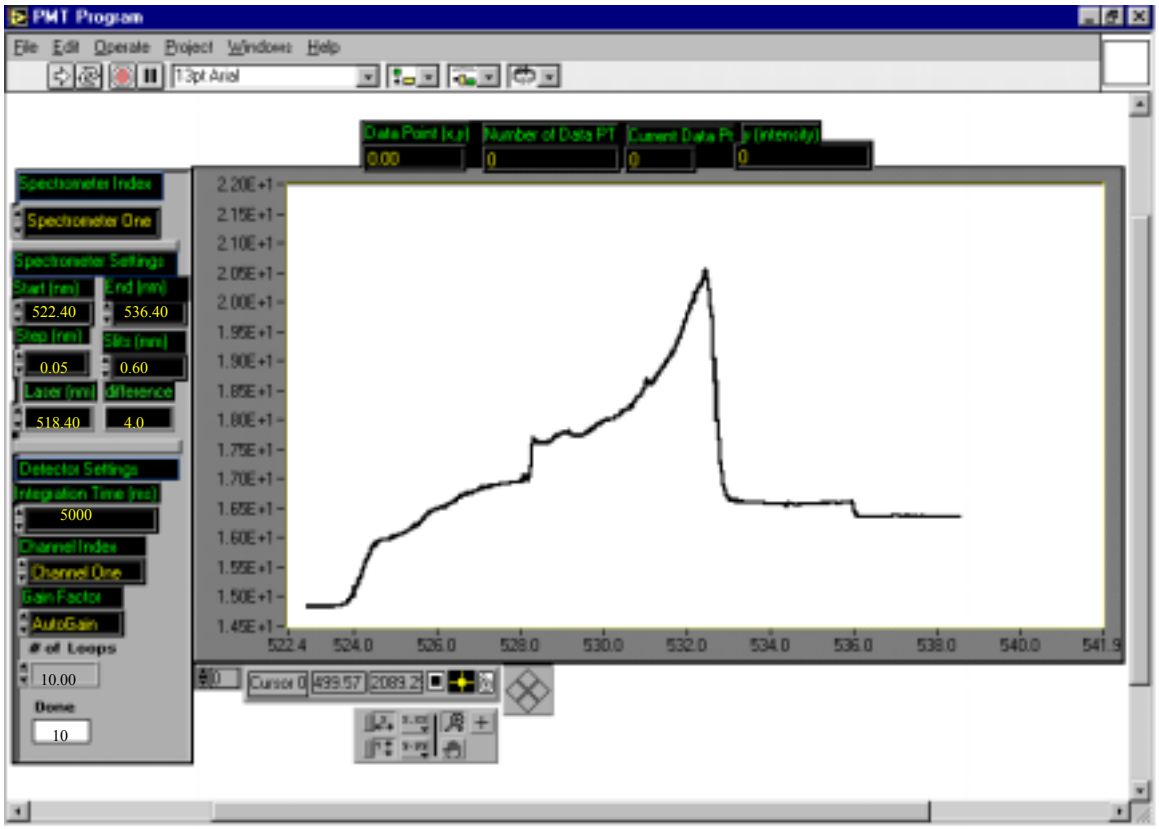

FIGURE 3-8. This is a diagram of the slit controller program in LabView.

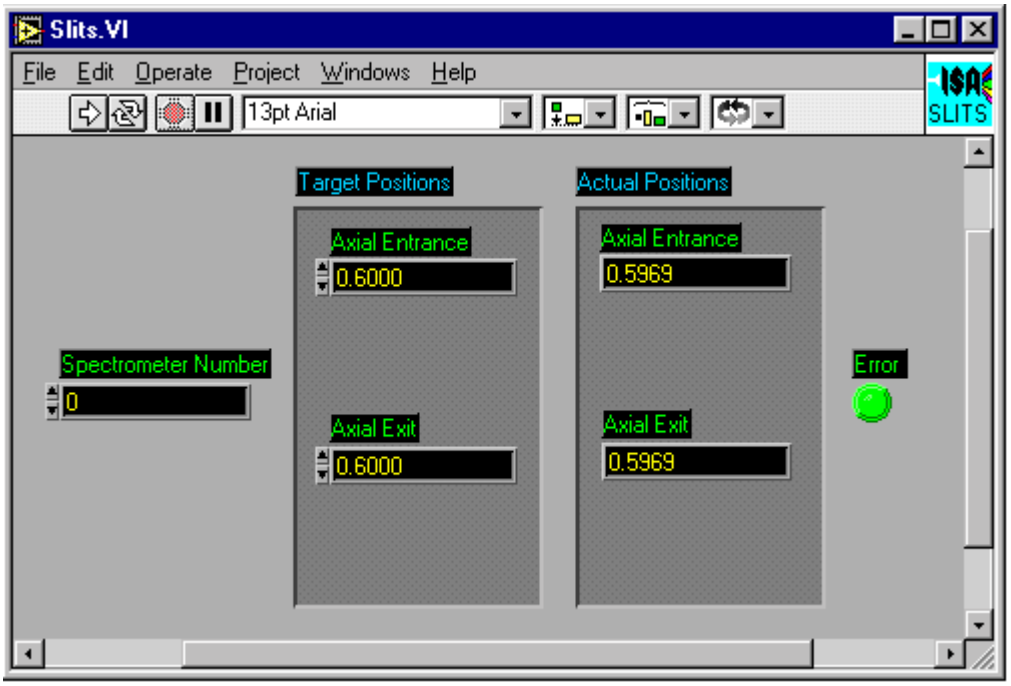

FIGURE 3-9. This is a diagram of the temperature monitoring program in LabView.

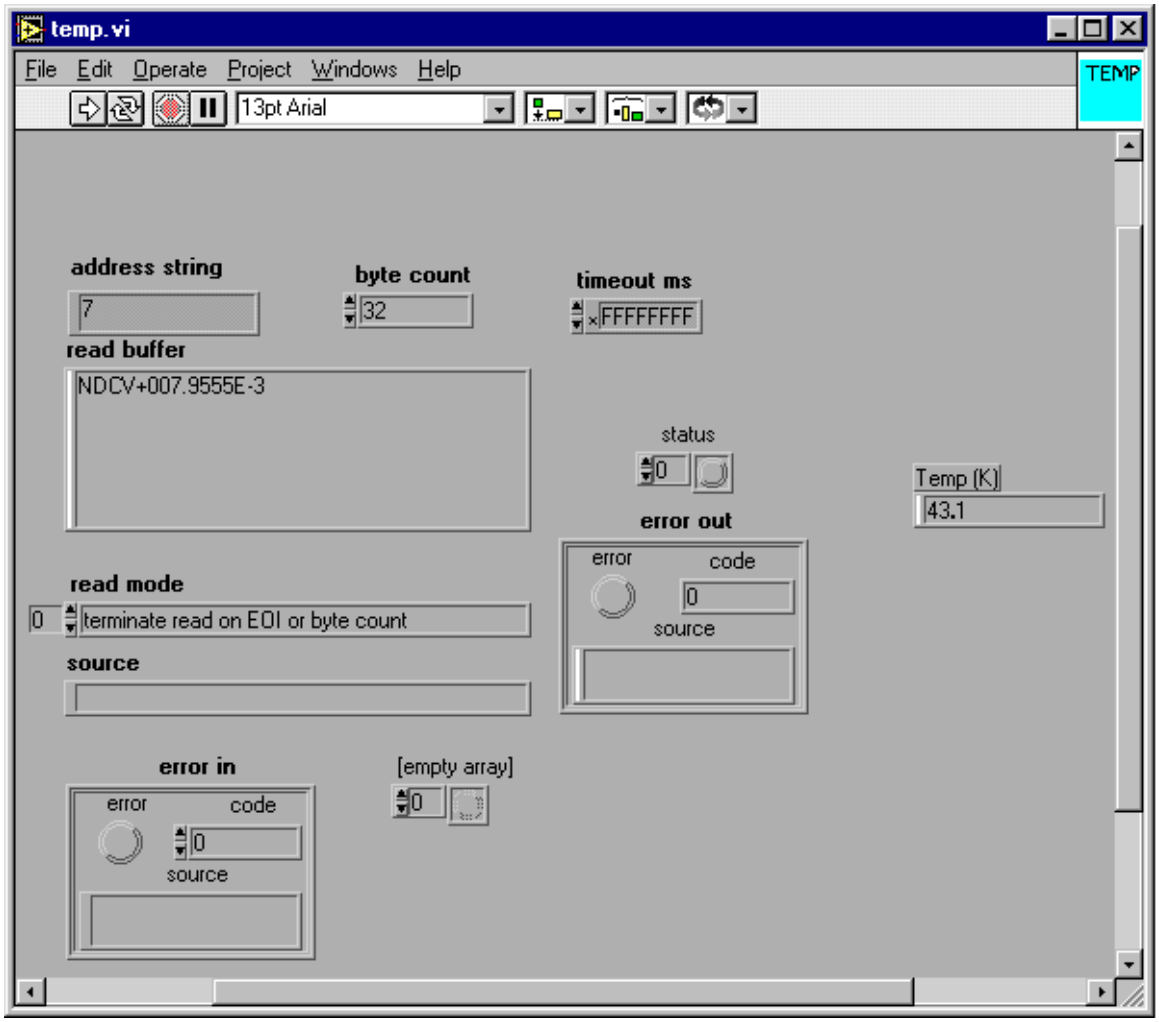

4. Discussion of Results

4.1. Discussion of the Critical Temperature (T_c) Dependence on Nickel Doping

We measured the resistivity of the control sample, $YBa_2Cu_3O_{7-\delta}$, and of the nickel substituted $YBa_2(Cu_{1-x}Ni_x)_3O_{7-\delta}$ samples, as a function of temperature to determine their critical temperatures, T_c. We used a carbon-glass resistor at the sample position to measure the sample temperature, and we used a conventional four probe technique to measure the sample resistivity. In order to better understand the different J_c values measured in all of the nickel-doped samples, the critical temperature, T_c, needed to be determined with certainty for each of the samples. The critical temperature as determined from the resistivity midpoint is at a comparable temperature to that obtained from a magnetic susceptibility midpoint temperature determination [39]. We also measured the critical temperature of the pure (control) sample, $YBa_2Cu_3O_{7-\delta}$, to ensure its quality as the control sample for the experiment.

Figure 4-1 depicts the temperature dependence of the resistivity for all of the samples. The transition width is observed to be around 4 K for all of the doped samples and less than 2 K for the undoped control sample. More specifically, the transition width is 2.0 K (91 K – 89 K), for x = 0.0, 4.0 K (88 K – 84 K) for x = 0.0032, 4.2 K (88 K – 83.8 K) for x = 0.0064, and 4.3 K (86 K – 81.7 K) for x = 0.0096. These results show that the critical temperature is depressed by the nickel doping of the samples. This result is also in agreement with the literature [37,40] as can be seen in Fig. 4-2. The resistivity in the high temperature ($90\ K \leq T \leq 150\ K$) region is linear. This linearity has been linked to the two-dimensional character of the electron transport [8].

FIGURE 4-1. This is the temperature dependence of resistivity for $YBa_2(Cu_{1-x}Ni_x)_3O_{7-\delta}$ ($\delta = 0$), with all doping levels tested.

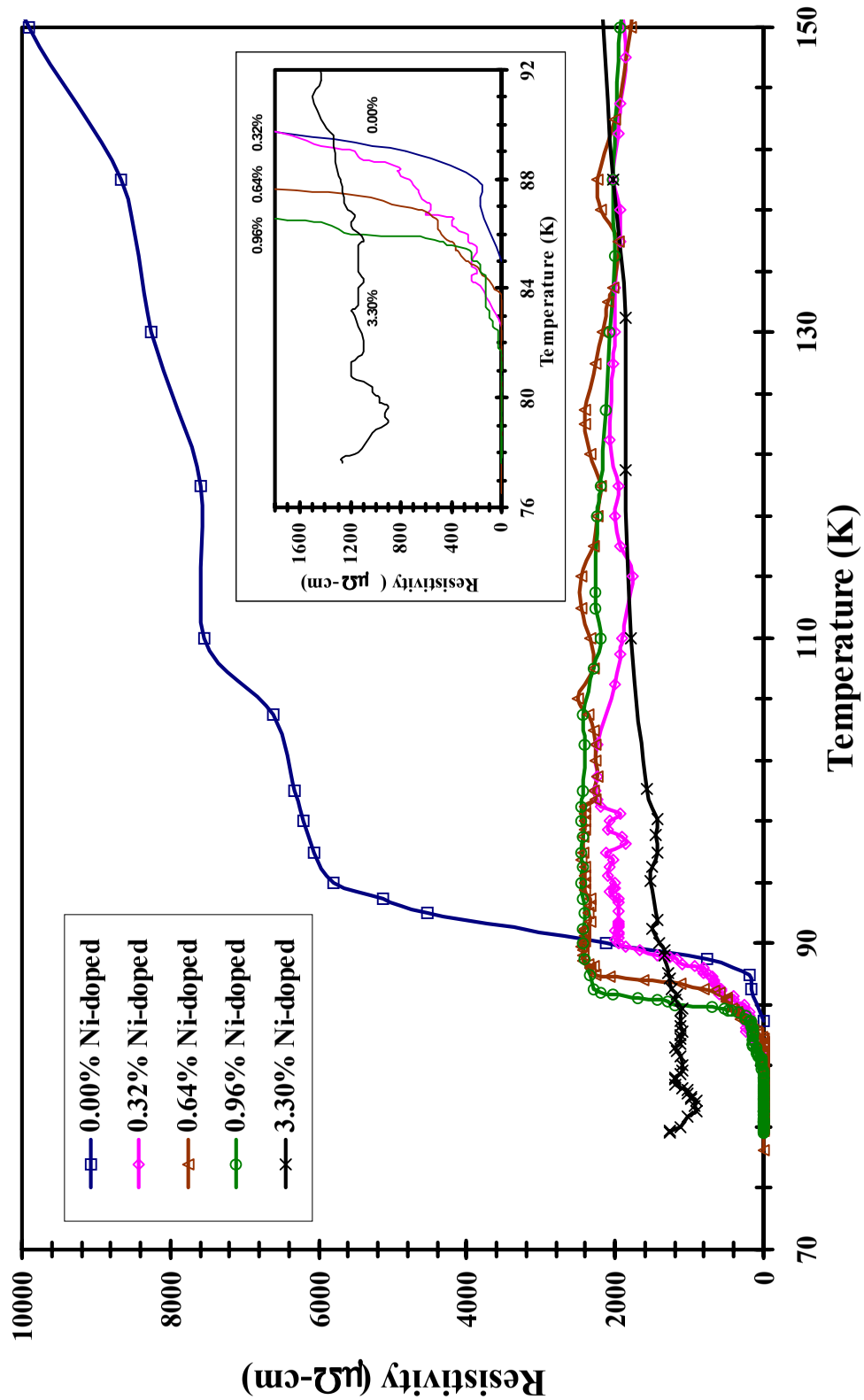

FIGURE 4-2. This shows the superconducting transition temperature, T_c, as a function of the Ni concentration in Y-B-Cu-O(Ni_x) using the corrected Ni concentrations [37]. [By F. Bridges *et al*]

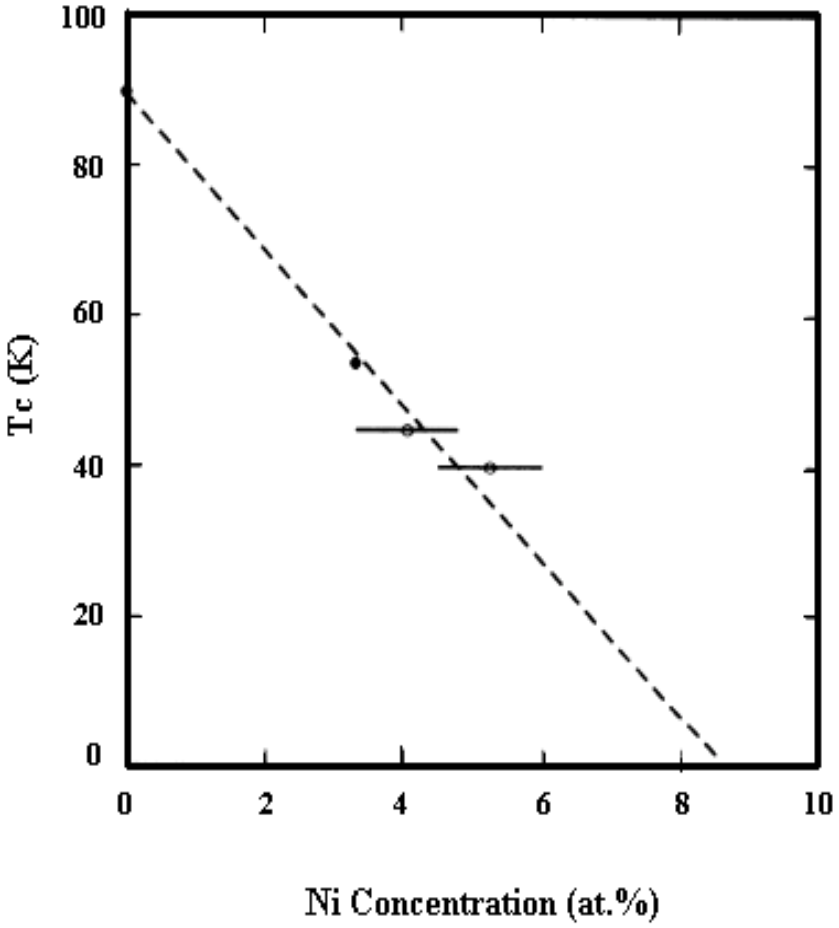

Fig. 4-3 shows the temperature dependence of the resistivity for the control sample. The critical temperature was 91 K with the transition width less than 2.0 K. The smoothness of the normal state resistivity, indicative of high sample quality and purity, should be noted.

Fig. 4-4 represents the temperature dependence of resistivity for the nickel doped sample with x = 0.0032 ($YBa_2[Cu_{0.9968}Ni_{0.0032}]_3O_7$), whose critical temperature was 90 K with a transition width less than 4.0 K. The normal state of this sample is ohmic. The jaggedness of the sample's normal state resistivity is already indicative of reduced sample quality due to impurity phases and of voltage fluctuations due to increasing grain boundary contamination of NiO.

Fig. 4-5 exhibits the temperature dependence of resistivity for the nickel doped sample with x = 0.0064 ($YBa_2[Cu_{0.9936}Ni_{0.0064}]_3O_7$). The critical temperature was 88 K with the transition width less than 4.2 K.

Fig. 4-6 exhibits the temperature dependence of resistivity for the nickel doped sample with x = 0.0096 ($YBa_2[Cu_{0.9904}Ni_{0.0096}]_3O_7$). The transition width, with an onset critical temperature of 86 K, was less than 4.3 K.

In Fig. 4-7, the critical temperature onset was not as readily apparent as for the other samples. Although the sample showed a partial transition around 82 K, the resistivity below 80 K held almost steady at a low value due to the extent of the contamination of NiO at the grain boundaries at this highest dopant level.

FIGURE 4-3. This is the resistivity versus temperature curve for undoped $YBa_2Cu_3O_{7-\delta}$ ($\delta = 0$).

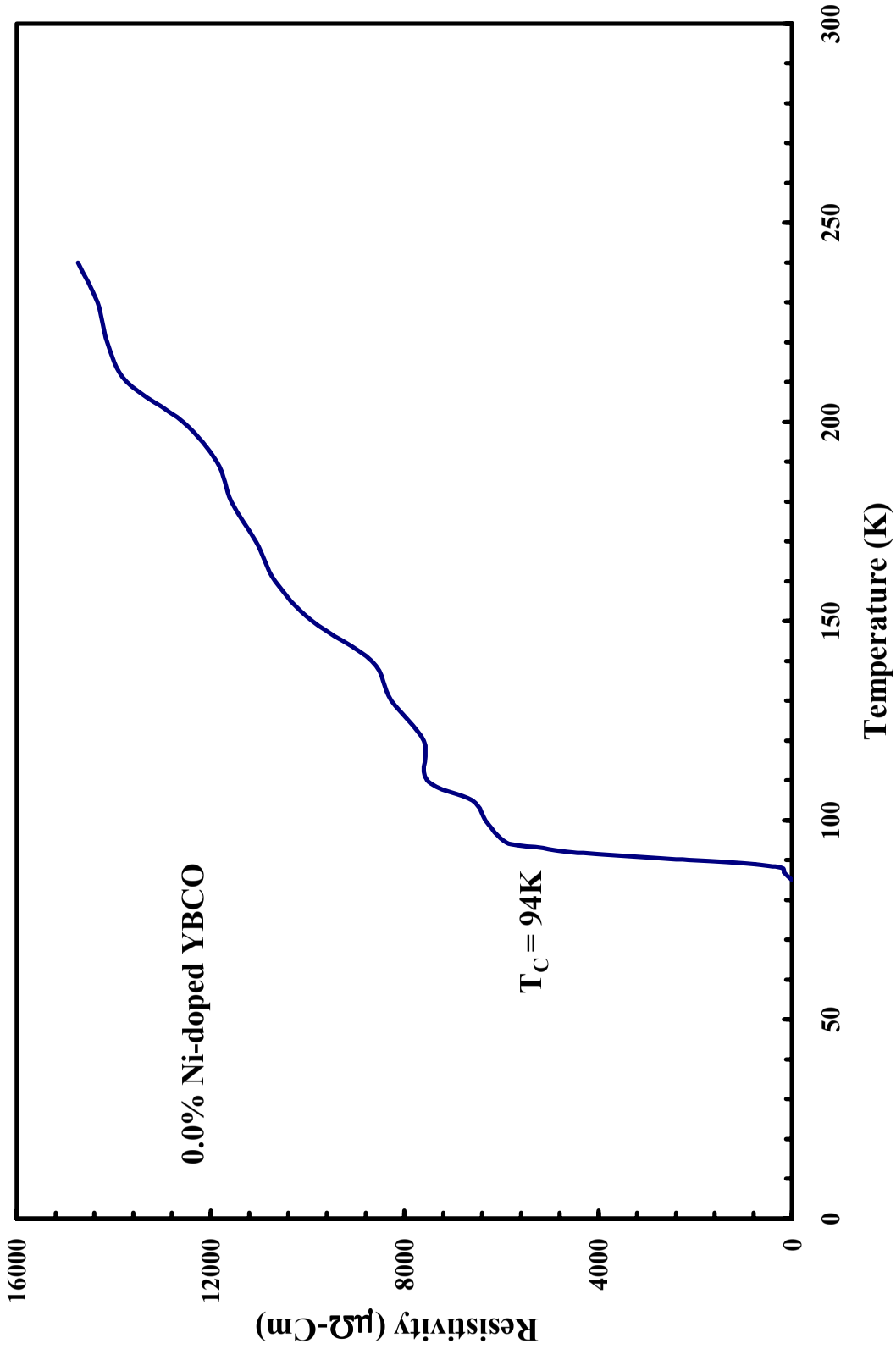

FIGURE 4-4. This is the resistivity versus temperature curve for $YBa_2(Cu_{1-x}Ni_x)_3O_{7-\delta}$ (x = 0.0032, δ=0).

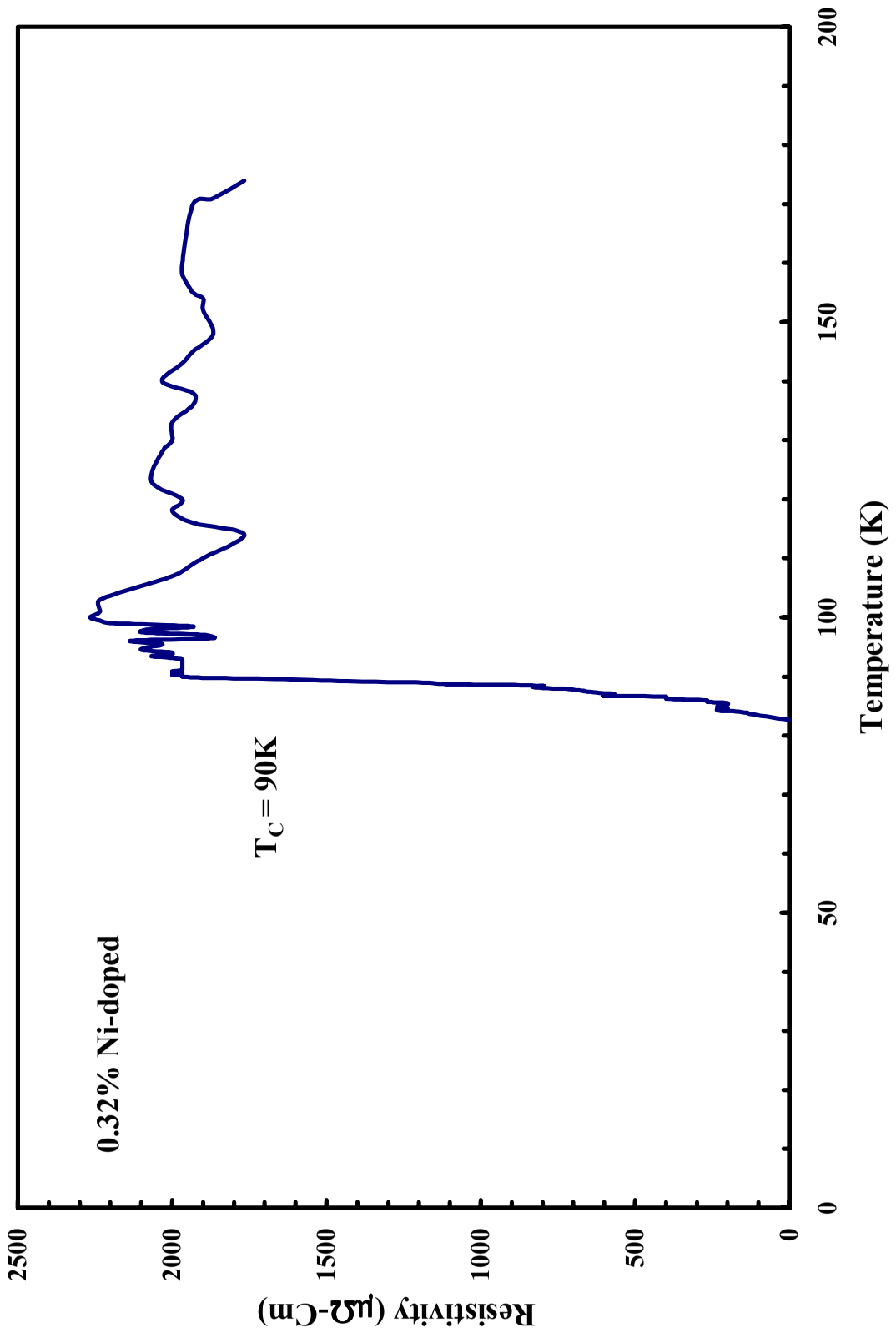

FIGURE 4-5. This is the resistivity versus temperature curve for $YBa_2(Cu_{1-x}Ni_x)_3O_{7-\delta}$ (x = 0.0064, δ=0).

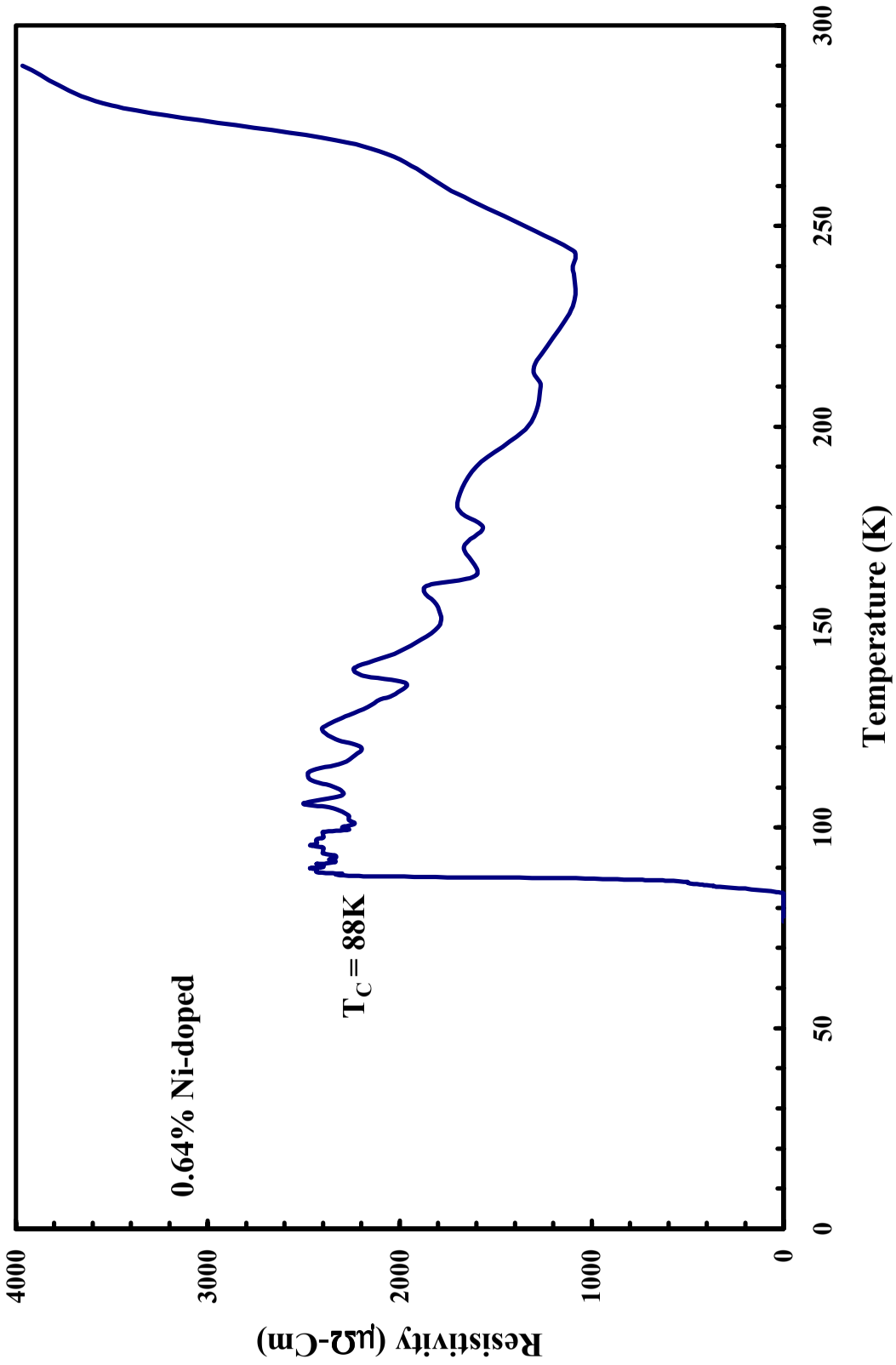

FIGURE 4-6. This is the resistivity versus temperature curve for $YBa_2(Cu_{1-x}Ni_x)_3O_{7-\delta}$ (x = 0.0096, δ=0).

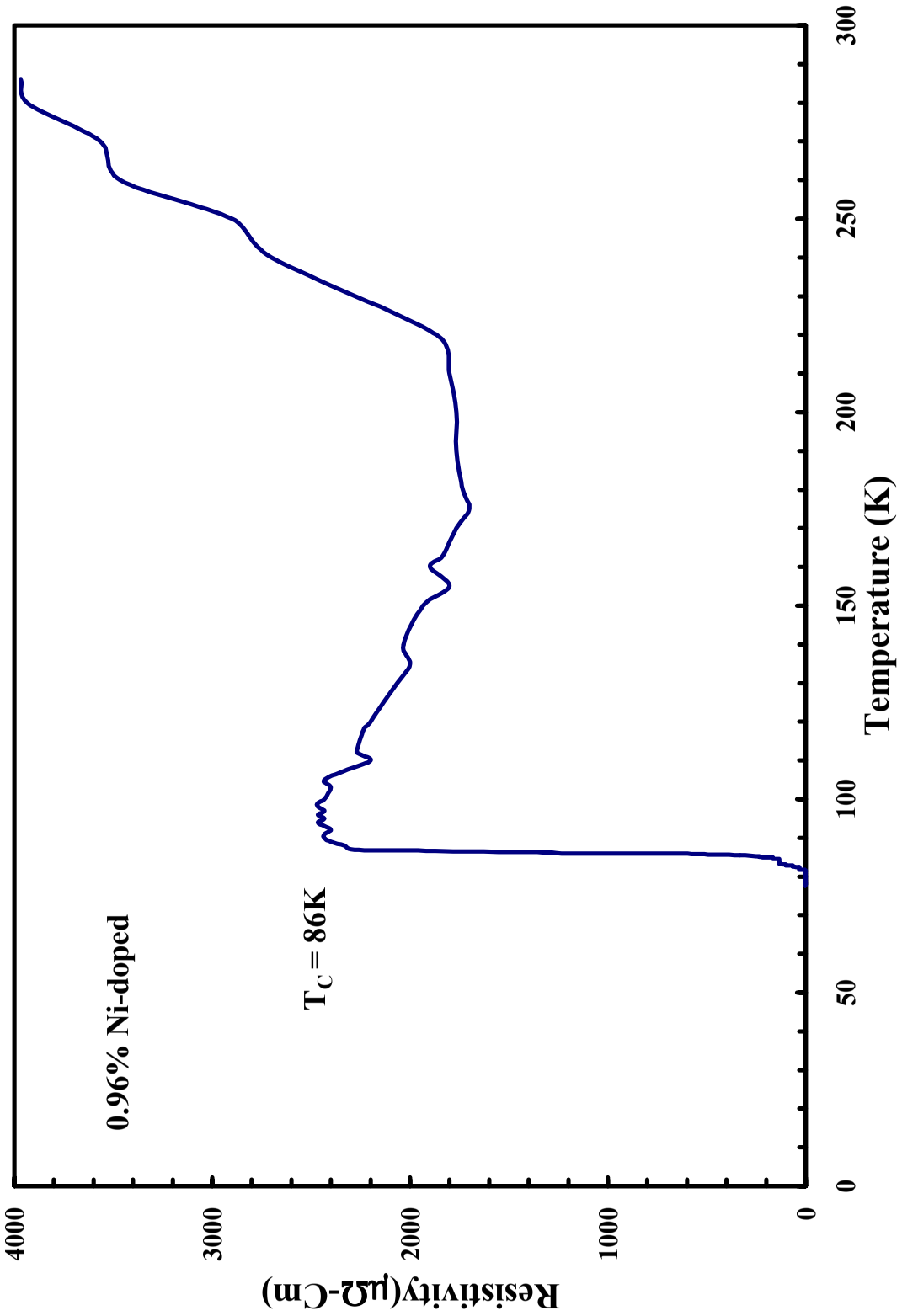

FIGURE 4-7. This is the resistivity versus temperature curve for $YBa_2(Cu_{1-x}Ni_x)_3O_{7-\delta}$ (x = 0.033, δ=0).

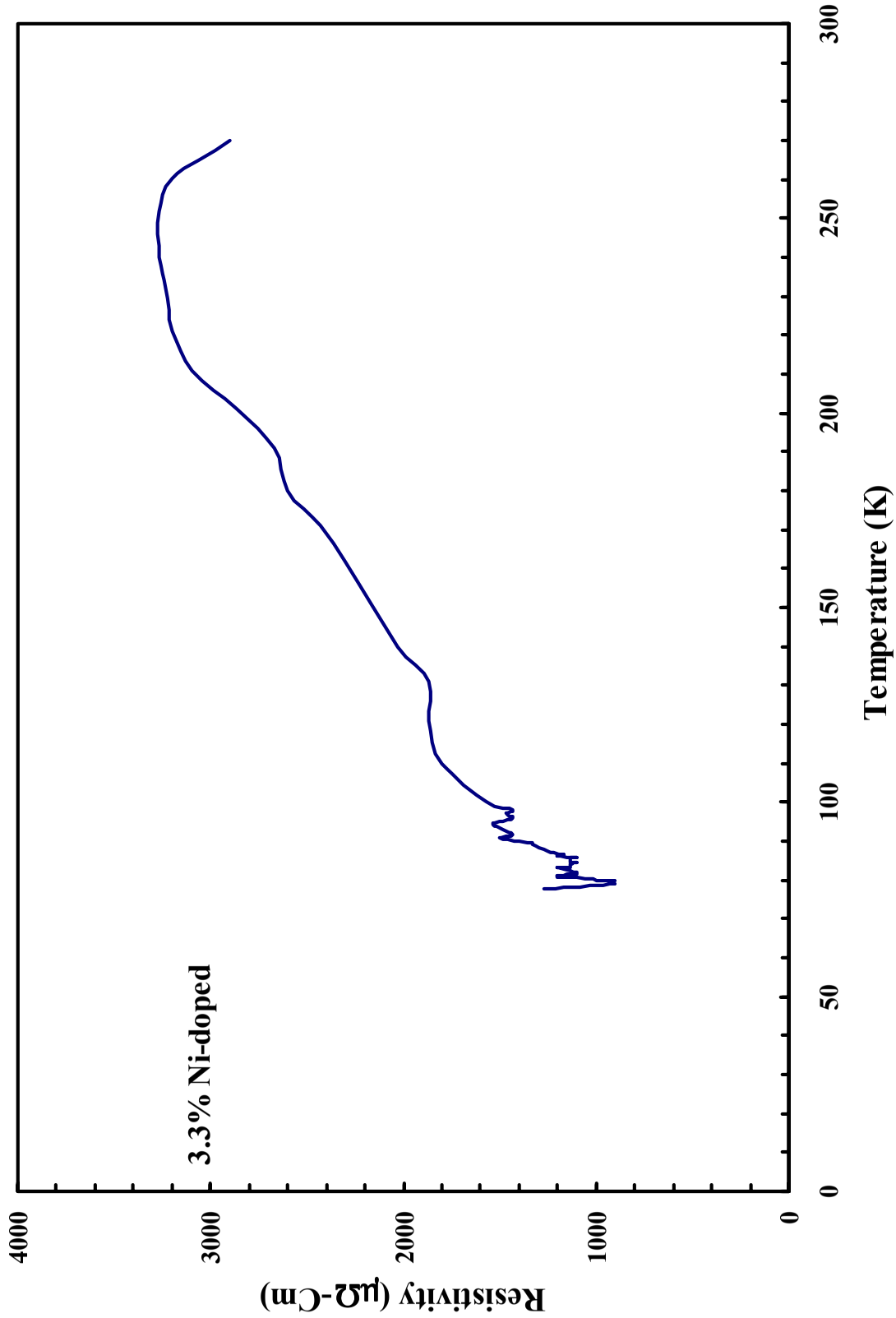

4.2. Discussion of the Critical Current Density (J_c) Dependence on Nickel Doping

Next, we turn to the discussion of the results of our critical current measurements for $YBa_2(Cu_{1-x}Ni_x)_3O_{7-\delta}$. The values of J_c can be determined directly by the four point probe method as discussed in the earlier section. A large enhancement of J_c has been observed at the x = 0.0032 level at 77 K in the lower range of magnetic field values as can been seen in the inset of Fig. 4-8 after comparison to the undoped sample (x = 0). However, the critical current density of the 0.32 % doped sample deteriorated below the control sample for higher magnetic field values. On the contrary, the sample with x = 0.0064 predominates in the higher magnetic field values at 77 K. This figure also shows that the higher doped sample (x = 0.0096) has a lower J_c than the control sample at both lower and higher magnetic fields. At 60 K, the prominent enhancement of J_c was also observed in the lower range of magnetic field values at the x = 0.32 % Ni dopant level. In this case, all samples in the low magnetic field values show an enhancement when compared to the control sample, as can be seen in Fig. 4-9. On the other hand, the sample at x = 0.0064 was superior to the others in the higher magnetic field. The higher doped sample (x = 0.0096) deteriorated in the higher magnetic fields in the same manner as at 77 K, and had lower critical current values than even the undoped sample.

As the samples are cooled down through the transition temperature T_c, the critical current value, theoretically, would be expected to gradually increase to its maximum value when the sample reached 0 K. Figs. 4-10, 11, 12, and 13 are measured at the sample temperatures of 77 K and 60 K. According to our results, the critical current density at 60 K is clearly higher than that at 77 K for all of the Ni-doped samples. As can

FIGURE 4-8. This is the critical current density versus magnetic field for $YBa_2(Cu_{1-x}Ni_x)_3O_{7-\delta}$ (δ=0) at 77K for all doping levels tested and the control sample.

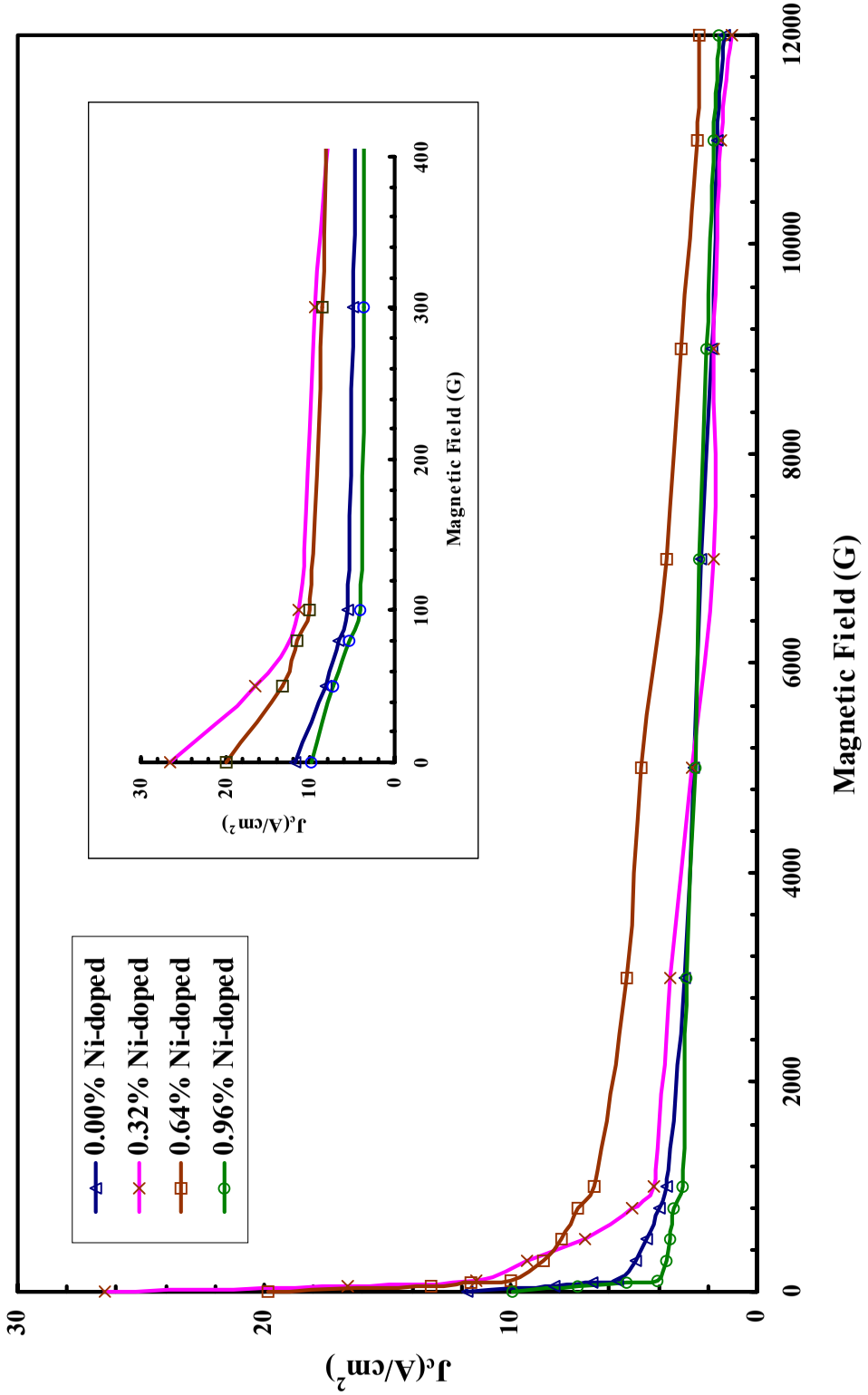

FIGURE 4-9. This is the critical current density versus magnetic field for $YBa_2(Cu_{1-x}Ni_x)_3O_{7-\delta}$ (δ=0) at 60K for all doping levels tested and the control sample.

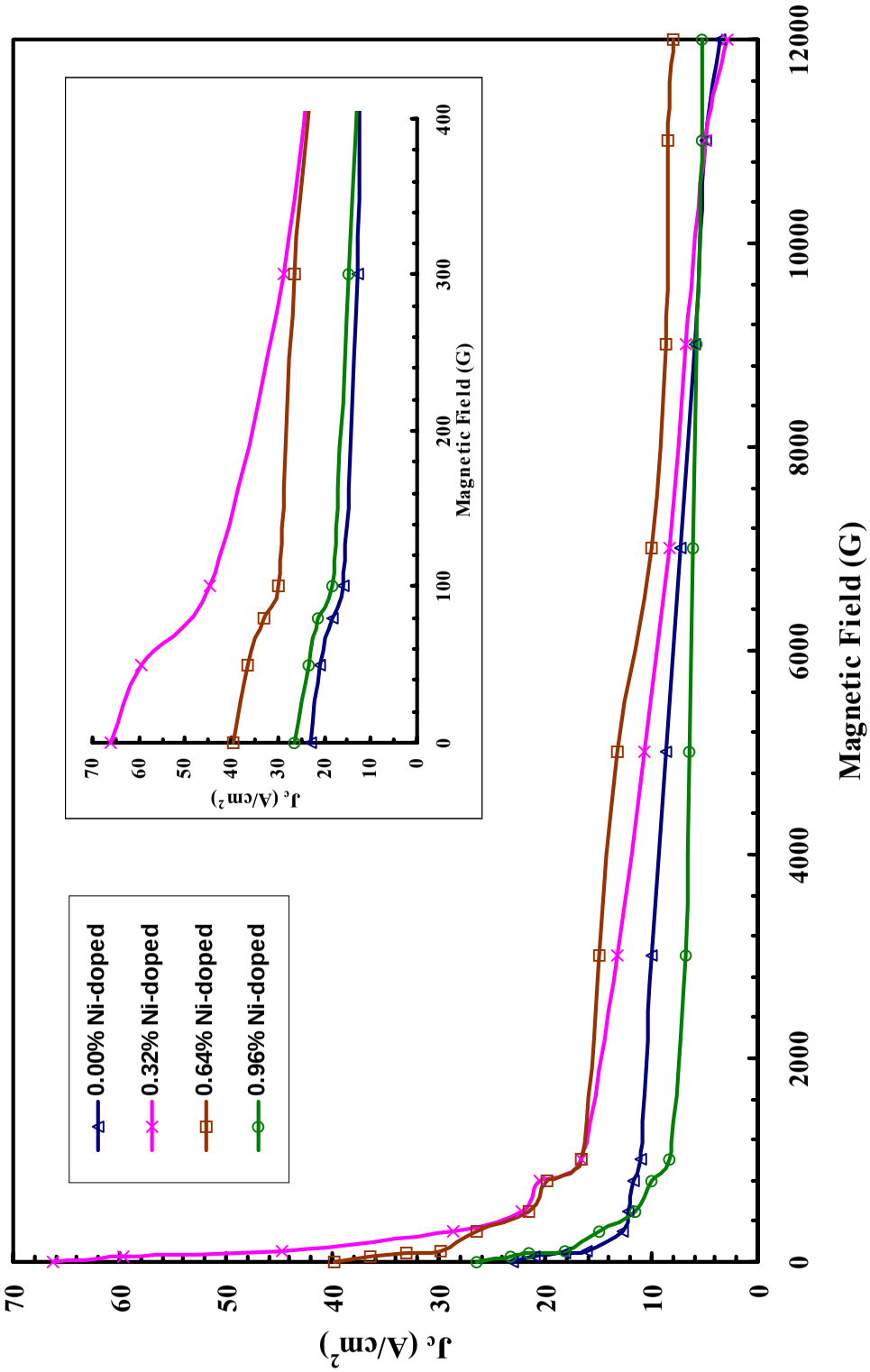

FIGURE 4-10. This is the critical current density versus magnetic field for $YBa_2Cu_3O_{7-\delta}$ (δ=0).

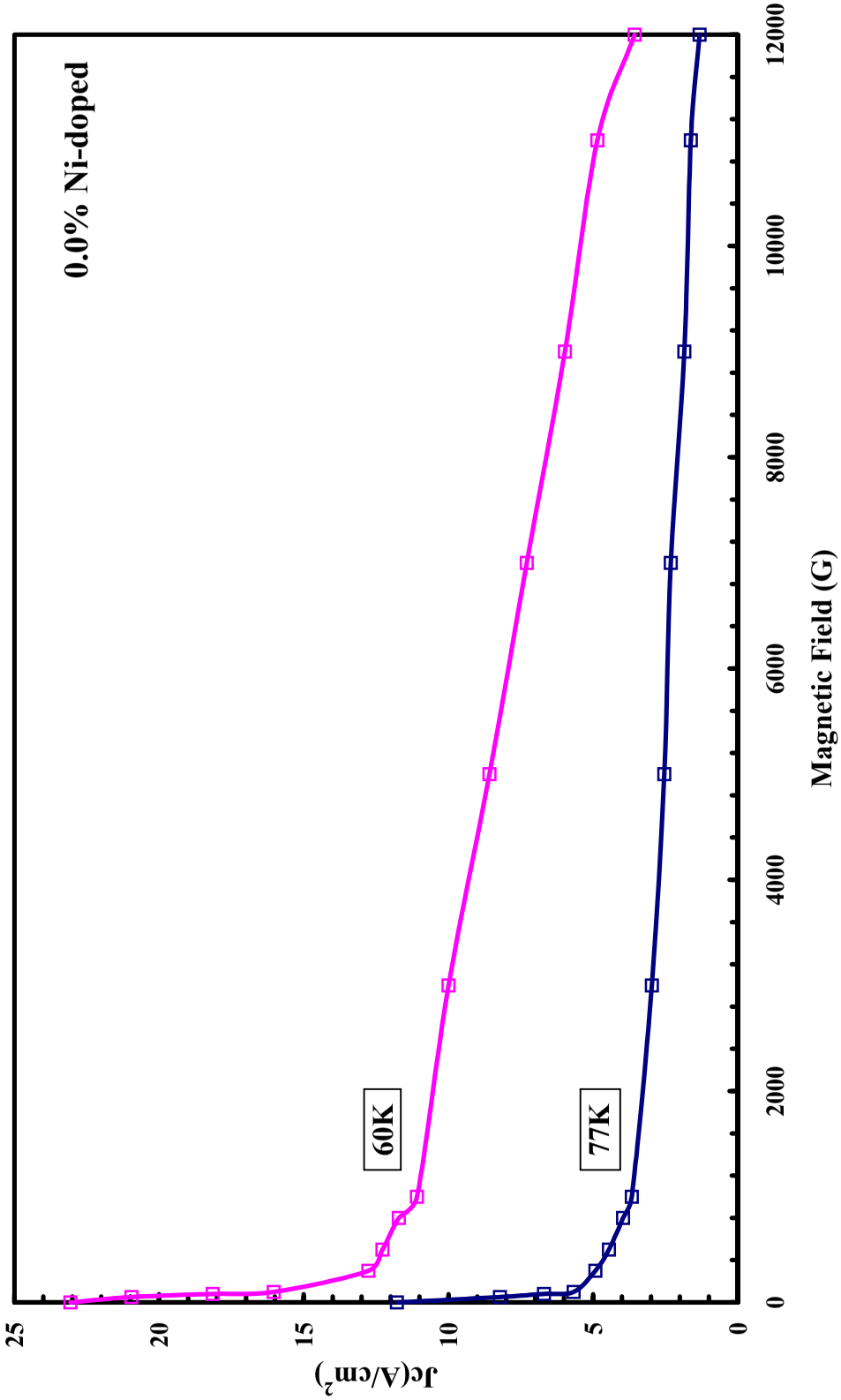

FIGURE 4-11. This is the critical current density versus magnetic field for $YBa_2(Cu_{1-x}Ni_x)_3O_{7-\delta}$ (x = 0.0032, δ=0).

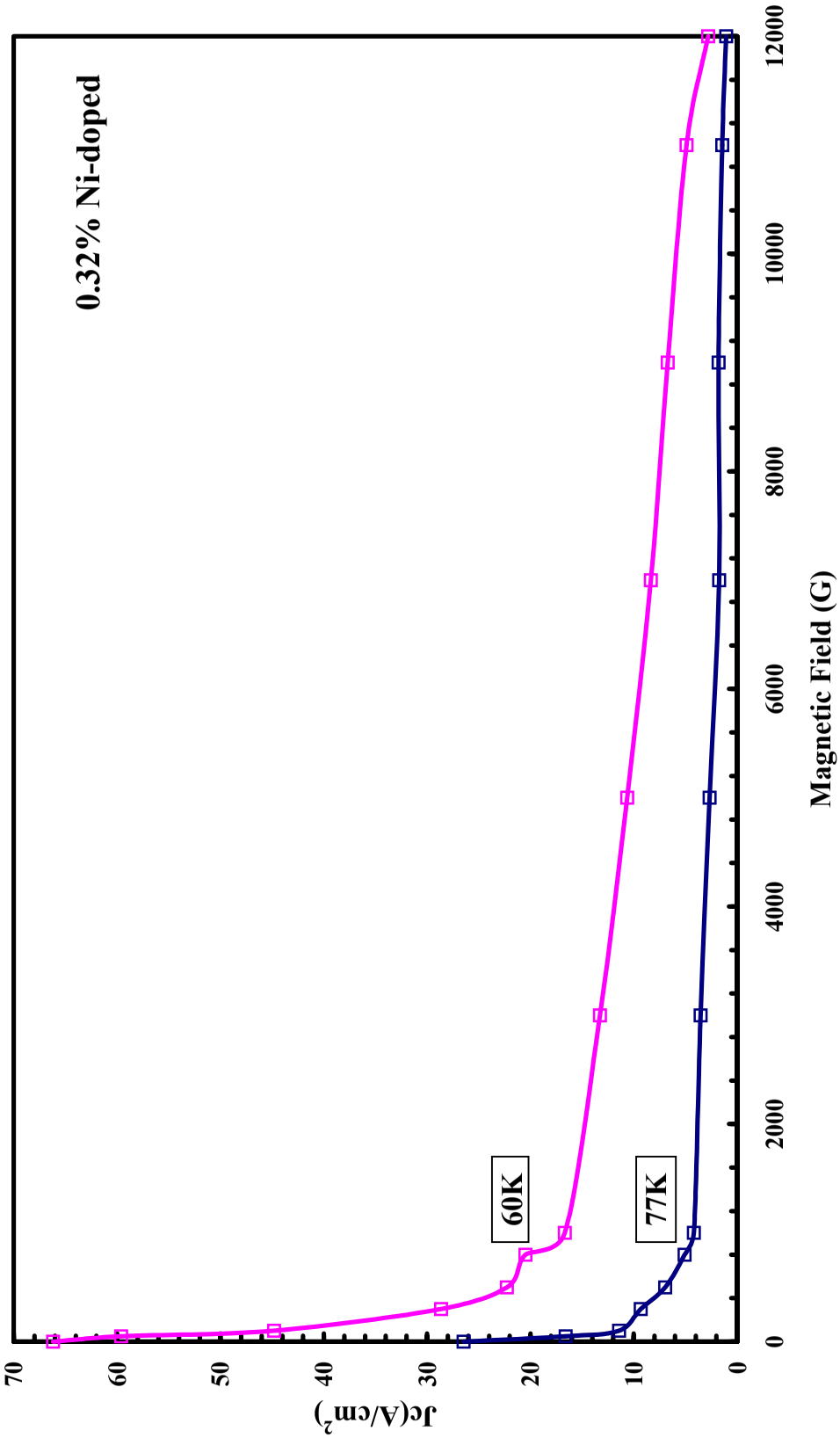

FIGURE 4-12. This is the critical current density versus magnetic field for $YBa_2(Cu_{1-x}Ni_x)_3O_{7-\delta}$ (x = 0.0064, δ=0).

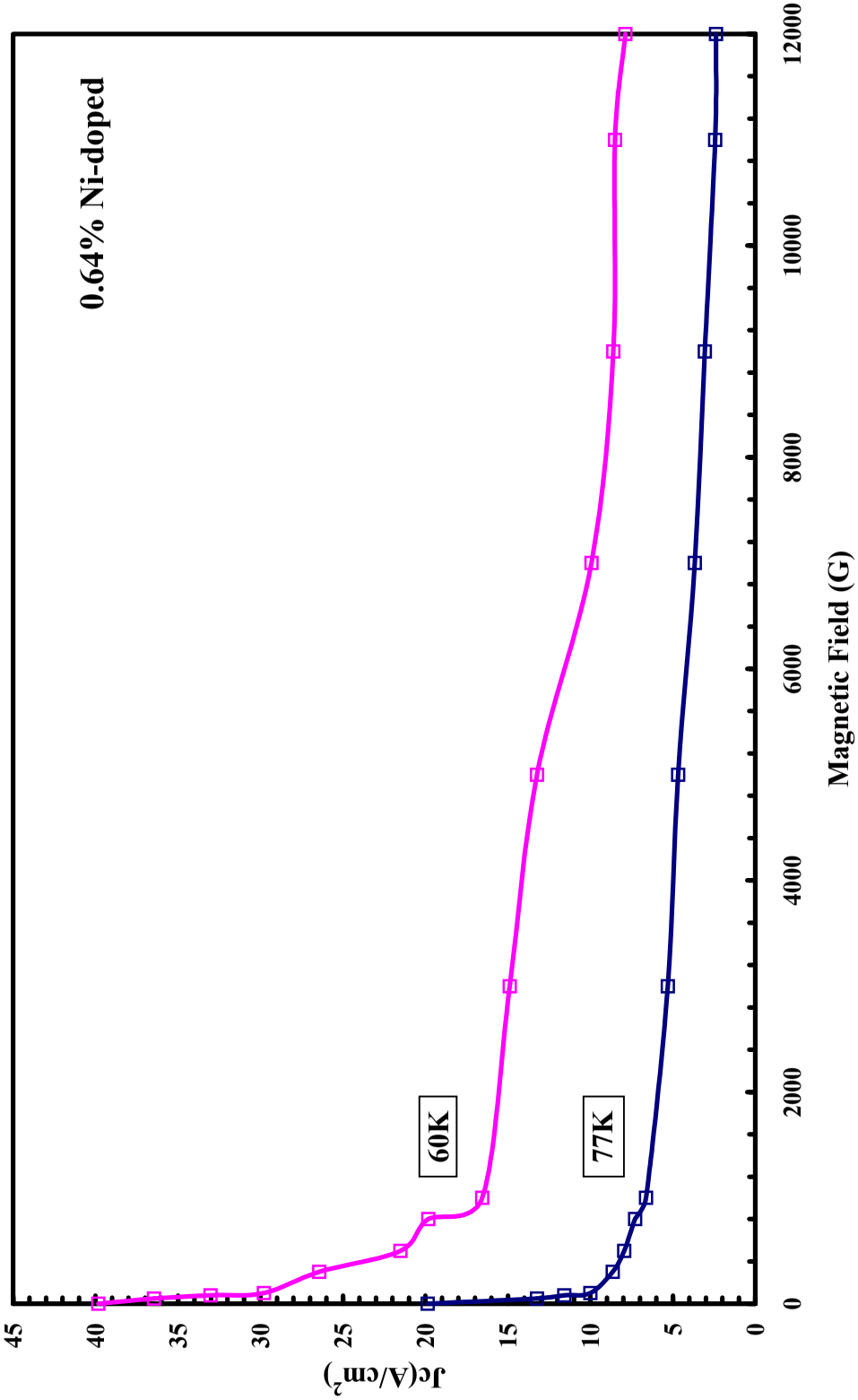

FIGURE 4-13. This is the critical current density versus magnetic field for $YBa_2(Cu_{1-x}Ni_x)_3O_{7-\delta}$ (x = 0.0096, δ=0).

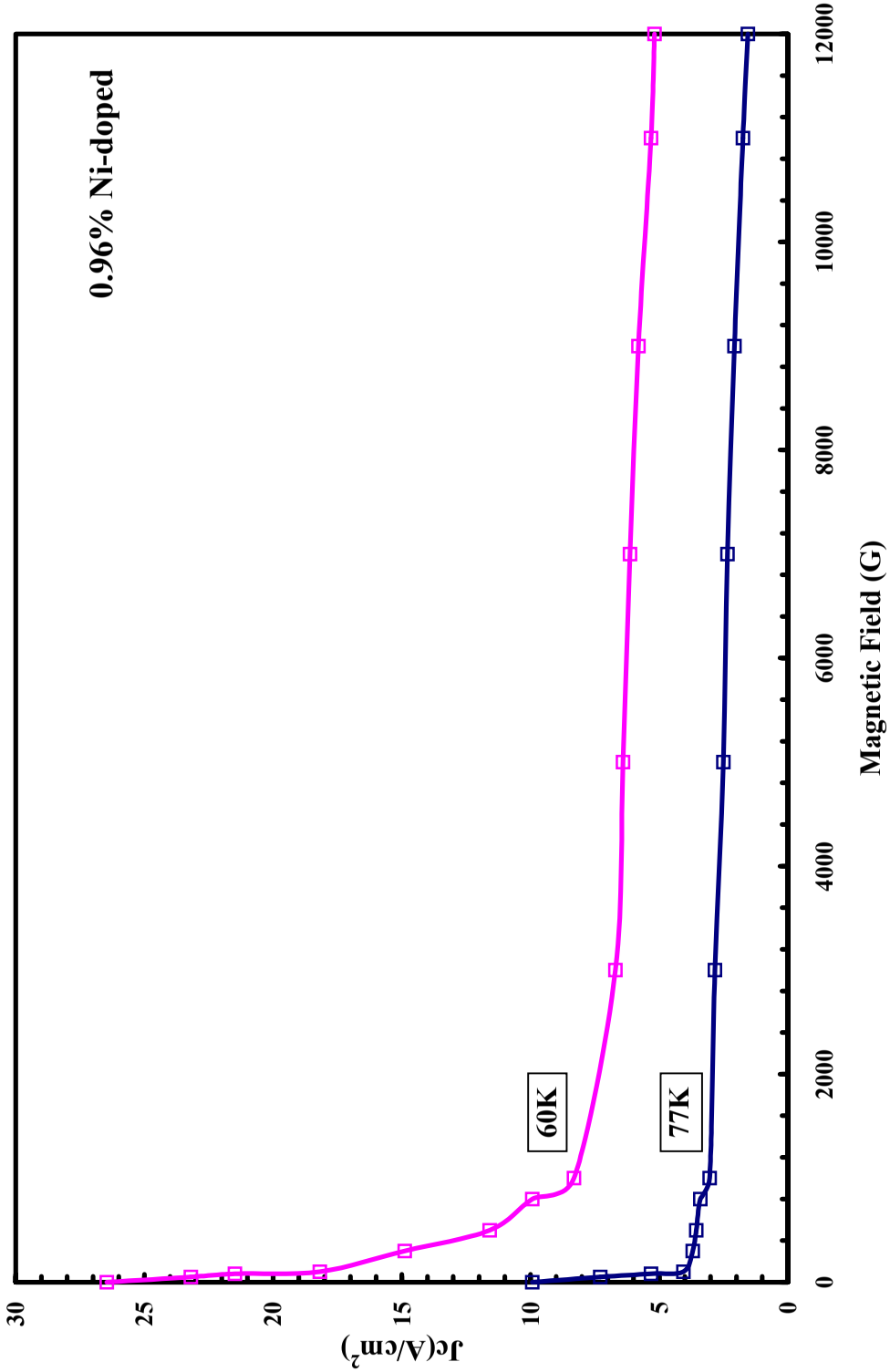

also be seen in Fig. 4-11, the critical current density exhibits the highest values at 60 K in the x = 0.0032 sample, when it is compared to the other dopant levels.

We collected the data for five magnetic field values located at the points of most dramatic change in each plot, and organized this data. Table 4 shows critical current density (J_c) values and corresponding values of the applied magnetic fields due to nickel doping (x = 0.0 %, x = 0.32 %, x = 0.64 %, and x = 0.96 %) at both the temperatures of 77 K and 60 K. Also, Fig. 4-14 illustrates the magnetic field dependence of J_c due to concentration x based on the results tabulated in Table 4. We can readily recognize that the critical current density drastically decreases due to the applied magnetic field, and that it also decreases with the nickel concentration x after surpassing the lowest level of concentration. And we can expect from these results that still higher levels of nickel doping in the $YBa_2Cu_3O_{7-\delta}$ system would only serve to further deteriorate the critical current density values.

TABLE 4. This shows critical current densities with their corresponding measurement temperatures and their values of the externally applied magnetic fields at the different levels of nickel doping used in our samples.
[Here, $\delta = 0$ for $YBa_2(Cu_{1-x}Ni_x)_3O_{7-\delta}$]

Concentration	J_c at 77 K					J_c at 60 K				
	Magnetic Fields **B** (**Gauss**)					Magnetic Fields **B** (**Gauss**)				
	0	100	1000	7000	12000	0	100	1000	7000	12000
x = 0.0000	11.78	4.46	3.66	2.31	1.32	23.07	16.04	11.09	7.29	3.56
x = 0.0032	26.47	11.42	4.19	1.75	1.06	66.20	44.81	16.67	8.35	2.81
x = 0.0064	19.87	10.00	6.63	3.66	2.38	39.83	29.80	16.57	9.93	7.89
x = 0.0096	9.93	4.06	3.04	2.34	1.55	26.47	18.18	8.32	6.14	5.18

FIGURE 4-14. This depicts the variation of the magnetic field dependence of J_c due to concentration x.

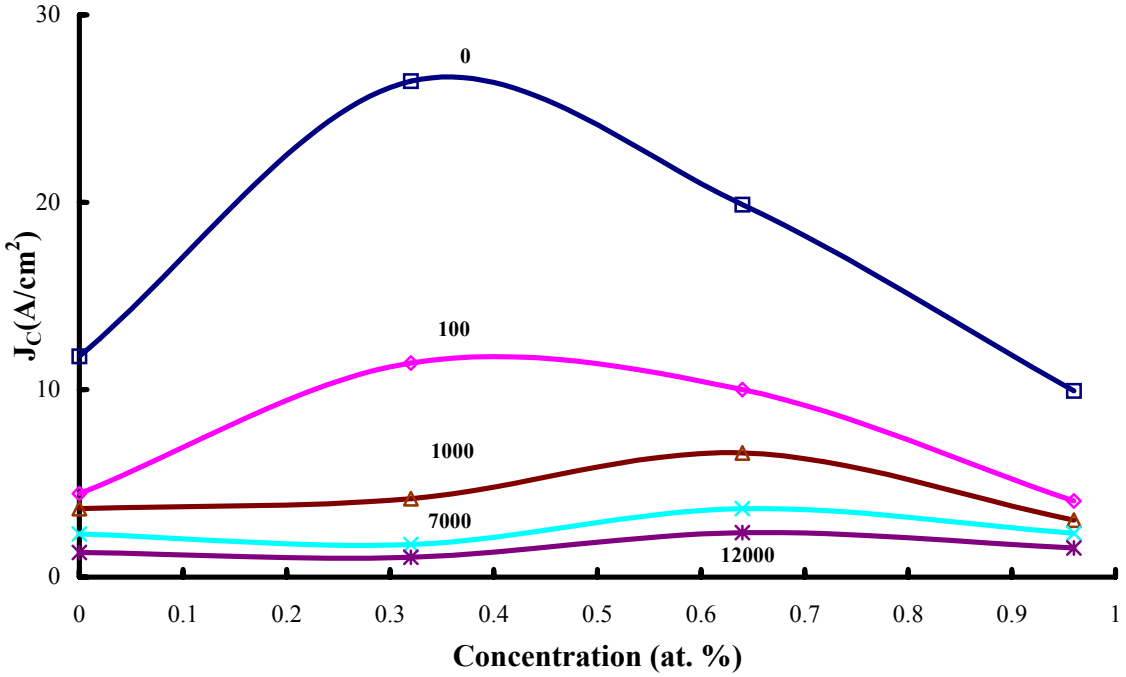

(a) The in-field decrease of J_c is shown at 77 K.

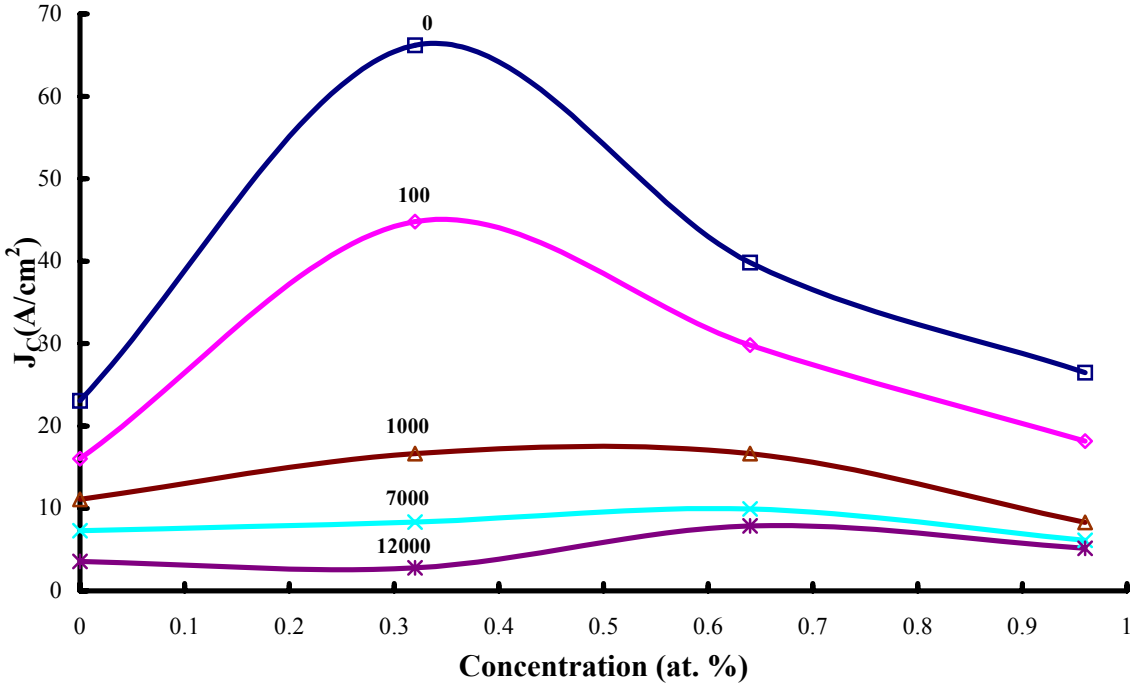

(b) The in-field decrease of J_c in shown at 60 K.

4.3. Discussion of Extended X-ray Absorption Fine Structure (EXAFS)

Along with the Fourier transforms of the Ni-doped $YBa_2Cu_3O_{7-\delta}$ samples, a Fourier transform of a reference NiO sample from a standard EXAFS experiment was taken for comparison [41]. Raw data from the EXAFS experiment had been taken from unpublished data by Lytle, and therefore it is impossible to determine the exact conditions of the EXAFS measurement. The raw reference data had been analyzed with the same method as the Ni-doped $YBa_2Cu_3O_{7-\delta}$ samples. The purpose of this reference sample was to see if the Ni was substituted into the $YBa_2Cu_3O_{7-\delta}$, or if it remained as a NiO impurity. If the situation is the latter, then the distance peaks in all four Fourier transforms should be the same within a degree of error.

The small peaks that precede the first large dominant peak in the experimental results are simply artificial results from noise in the experiment, since it is not possible to have atoms at such a short distance in this material. The distances for the peaks were found using WinXAS 97v1.3 to find the minima and maxima of the plots and then matching to the graphs. The EXAFS spectra for the four samples are included in Figure 4-15, and the NiO spectra is shown in Figure 4-16. There are five peaks of interest in the experimental results and these distances are displayed in Table 5, along with three main peaks of the NiO reference sample, with the distances grouped together for comparison. The heights of the peaks in each graph are included as well in parentheses.

Based on the results in Table 5, the Ni does indeed appear as an impurity in the form of NiO in the Ni-doped $YBa_2Cu_3O_{7-\delta}$ samples, but only to a certain extent. Clearly the second atomic shell in the experimental samples are NiO atoms based on the

FIGURE 4-15. These are the Fourier transforms for the three low Ni-doped samples measured by EXAFS.

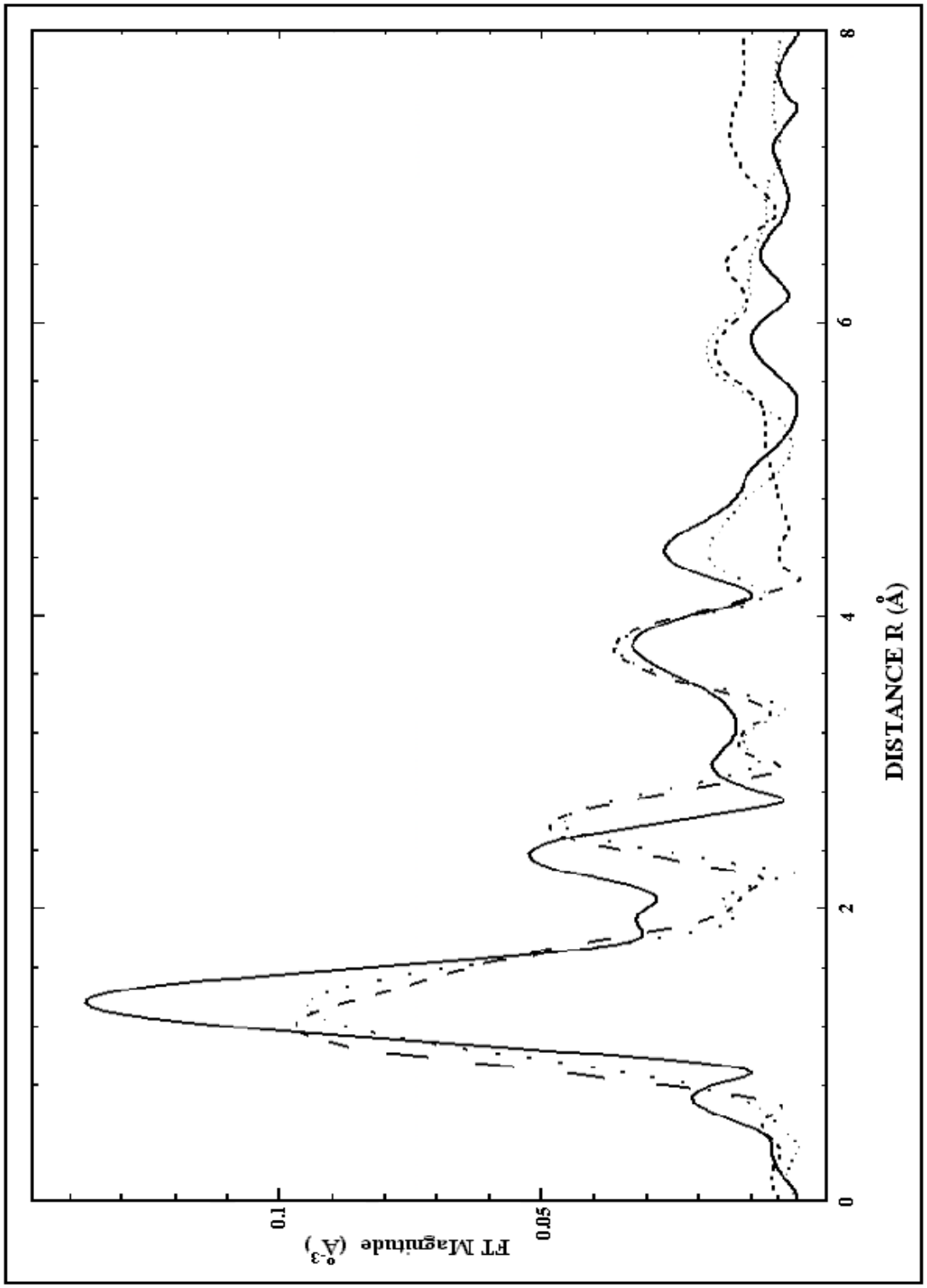

FIGURE 4-16. This is the Fourier transform of a reference NiO sample from a standard EXAFS experiment.

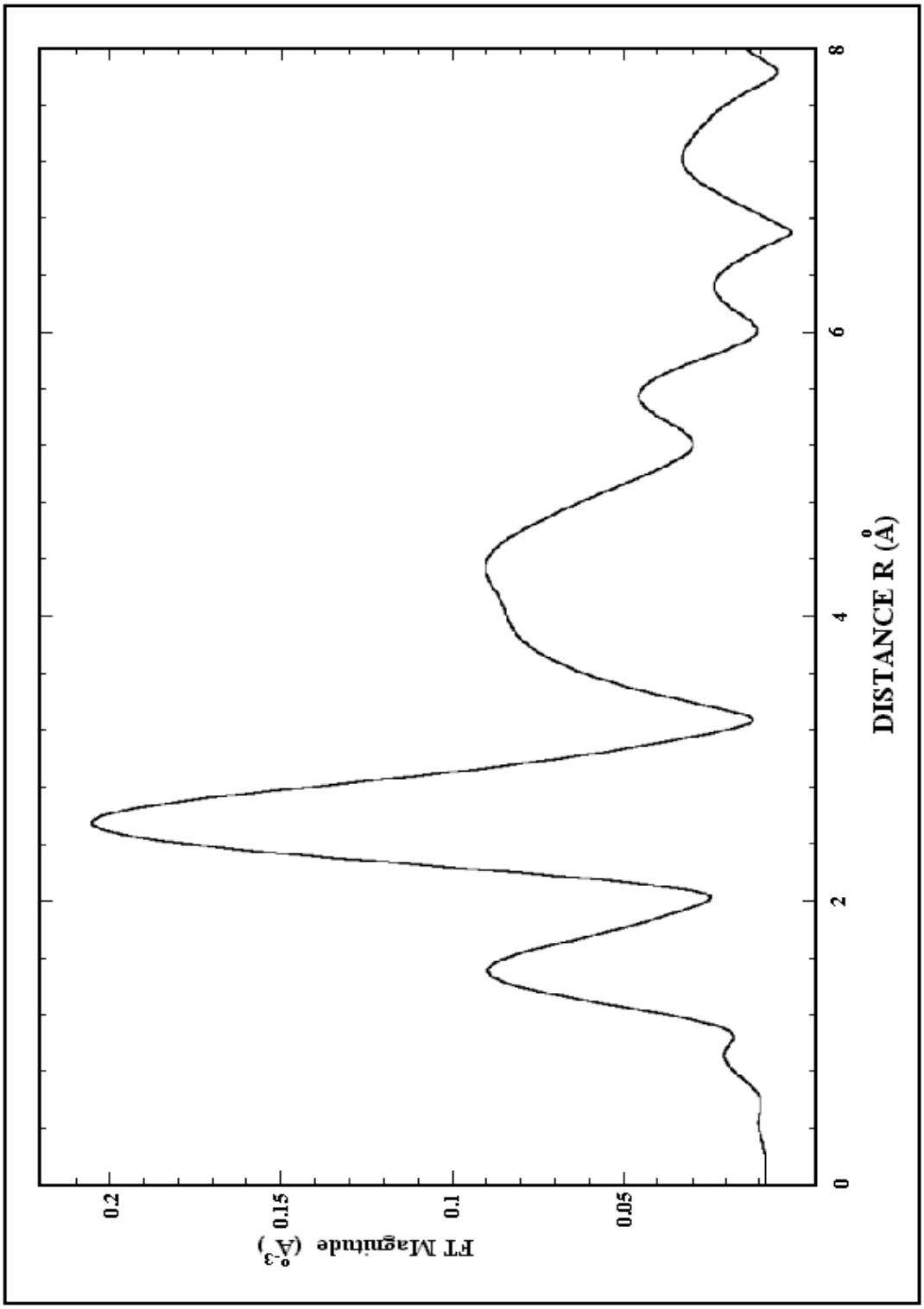

TABLE 5. These are the dominant peak distances from the Fourier transforms of the Ni-doped $YBa_2Cu_3O_{7-\delta}$ samples and the NiO reference sample.

	1st peak distance (Å) (height)	2nd peak distance (Å) (height)	3rd peak distance (Å) (height)	4th peak distance (Å) (height)	5th peak distance (Å) (height)
0.1% Ni	1.36 (0.137)	2.36 (0.052)	2.97 (0.017)	3.80 (0.033)	4.44 (0.027)
0.2% Ni	1.20 (0.097)	2.56 (0.048)	3.14 (0.012)	3.78 (0.036)	4.42 (0.005)
0.3% Ni	1.33 (0.095)	2.60 (0.046)	3.14 (0.011)	3.78 (0.036)	4.43 (0.018)
NiO reference	1.55 (0.088)	2.57 (0.208)	--- ---	--- ---	4.42 (0.090)

close relationship between the distances in the 2nd peak column. However, the 2nd peak heights as related to the 1st peak height in all the experimental samples suggest that more of the Ni is incorporated into the superconductor than appearing as an impurity. Even though the table only shows three peaks for the reference sample, it should be noted that the third peak at 4.42 Å is a very broad peak, which suggests that there is another peak very close to this distance at approximately 4 Å.

An analysis of the transforms appears to be somewhat inconclusive. The broad peak at around 4 Å in the NiO reference transform would suggest that NiO is present in the Ni-doped $YBa_2Cu_3O_{7-\delta}$ samples at approximately 4.42 Å. This is backed by the results in Table 5 as well due to the close relationship between the distances in the fifth column. However, this is somewhat uncertain since it is very difficult to make accurate judgements on nearest-neighborhood atomic shells past the third shell. The first atomic shell in all three samples is at a distance of 1.2 ~ 1.6 Å. Due to the non-order of the graphs, it is somewhat apparent that once Ni is substituted into the $YBa_2Cu_3O_{7-\delta}$, adding even more Ni will not change the structure of the $YBa_2Cu_3O_{7-\delta}$ in any real way. This result is reflected by the results of Bridges *et al* [37]. Their results show a change in interatomic distances between undoped YBCO and Ni-doped YBCO. The amount of Ni seems to be irrelevant when it comes to structure.

The only question remaining then is in regard to the atomic distance in the results. They do not really agree with the distances measured by Bridges *et al*. According to Bridges *et al*, the first atomic shell of significant number is a culmination of Ni(1)-O(1), Ni(2)-O(2), and Ni(2)-O(3) bonds at 1.95 Å [37]. The distance peaks of 1.36, 1.20, and 1.33 Å of the experimental samples do not agree with this result at all. The 1.95 Å value

falls outside of the FWHM standard deviation from the distance peaks. To better match this value, several different $\mu_0(E)$-fits were attempted using varying parameters. In the end, however, it was not possible to fit the first experimental distance peak to the result of Bridges *et al*. The other values measured by Bridges *et al* reveal Ni(2)-Y, Ni(2)-Ba, and Ni(1)-Ba bonds at 3.26, 3.33, and 3.49 Å respectively. In addition to this, the Ni-Cu bonds (Ni(2)-Cu(2), Ni(2)-Cu(2), Ni(1)-Cu(1), and Ni(1)-Cu(1)) are at approximately 3.97 Å. This range of distances appears in Figure 4-15 as a broad peak that could possibly be a summation of several unresolved peaks.

4.4. Raman Scattering Analysis

In general, the selective introduction of impurities through stoichiometric chemical dopants is preferable to other techniques such as radiation damage [42], which introduces a wide variety of scattering centers throughout the cross section of the sample. However, Ni has been thought to substitute preferentially into the Cu(2) plane site [43] in $YBa_2Cu_3O_{7-\delta}$ while there has been some evidence of Ni doping into the Cu(1) chain sites [44] previously as well. In this present study, we have attempted to investigate both of these possibilities at the lower levels of doping.

The sketch of the orthorhombic $YBa_2Cu_3O_{7-\delta}$ unit cell is illustrated in Fig. 4-17. The numbers in parentheses beside the atomic symbols show the valence states of the atoms at those sites. Along the **b** direction are the O(1) atoms that form the Cu(1)-O(1) chains. There are no equivalent oxygen atoms along the **a** direction and hence no Cu(1)-O(1) chains in this direction. Also, a segment of the linear chain used in theoretical

calculations is shown at the left; this is the chain formed by Cu(2) atoms and O(4) atoms, and lies along the **c** direction.

The Raman spectra for nominally pure Y-123 and for $YBa_2(Cu_{1-x}Ni_x)_3O_{7-\delta}$ with low Ni concentrations of x = 0.0032, x = 0.0064, x = 0.0096, and a higher Ni concentration of x = 0.033 are shown in Fig. 4-18(0.00%), Fig. 4-19(0.32%), Fig. 4-20(0.64%), Fig. 4-21(0.96%), and Fig. 4-22(3.3%), respectively. The first phonon spectra, of the pure Y-123 with orthorhombic structure, demonstrates a strong feature at 458 cm^{-1} which can be easily identified from the literature [45] as the phonon corresponding to the in-phase oxygen mode vibration, temperature corrected from the room temperature value of 440 cm^{-1}. The out-of-phase oxygen mode at 352 cm^{-1} can also be clearly identified, again temperature corrected from the room temperature value [45] of 340 cm^{-1}. Both of these peaks correspond to a distribution of oxygen vibration modes which are the O(2) and O(3) in the planes [45] as can be seen in Fig 4-17. Unfortunately, the vibrations involving the Cu-O chains in pure Y-123 cannot be observed by Raman scattering techniques since they have odd parity and are therefore only infrared-active [47]. However, under certain conditions which can destroy the symmetry of the Cu-O chains in the sample, they can again be made Raman-active, as previously shown in the literature for the case of oxygen deficiency [48] in the samples, and more specifically in the Cu-O chains themselves. Fig. 4-19 shows the Raman spectra of $YBa_2(Cu_{1-x}Ni_x)_3O_{7-\delta}$ with nickel doping (x = 0.0032), which was the dopant level producing optimal critical state enhancement, at a temperature of 20 K, and with δ approaching zero, as can be seen

FIGURE 4-17. Primitive unit cell of stoichiometric $YBa_2Cu_3O_{7-\delta}$. The stretching motion is indicated by the arrows on the O(4) atoms. A segment of the linear chain used in theoretical calculations is shown at the left [46]. (Altendorf *et al*)

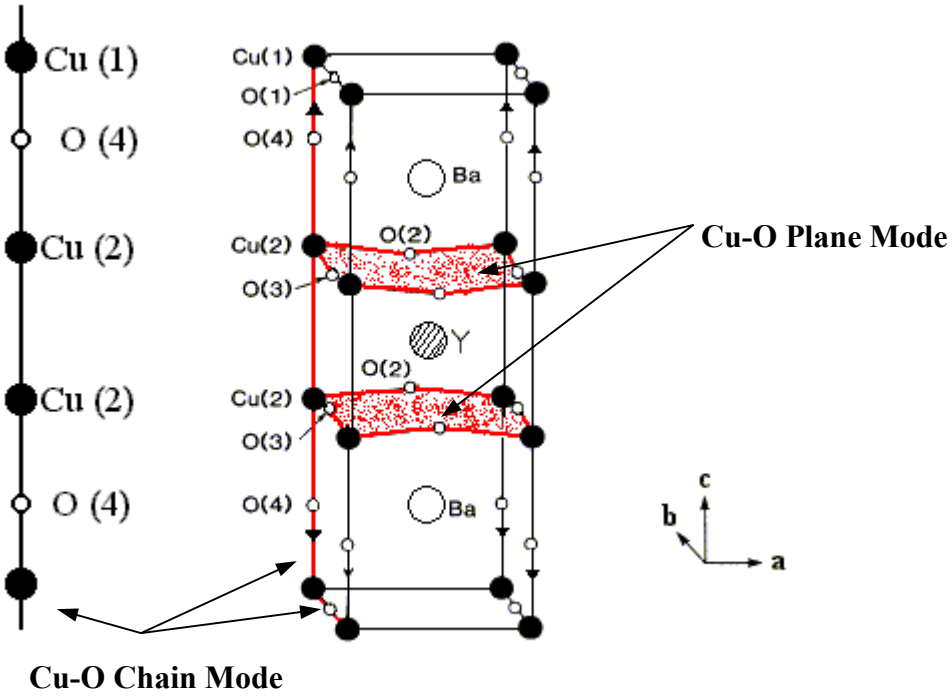

$YBa_2Cu_3O_{7-\delta}$

FIGURE 4-18. This is the Raman spectrum for undoped $YBa_2Cu_3O_{7-\delta}$ ($\delta = 0$).

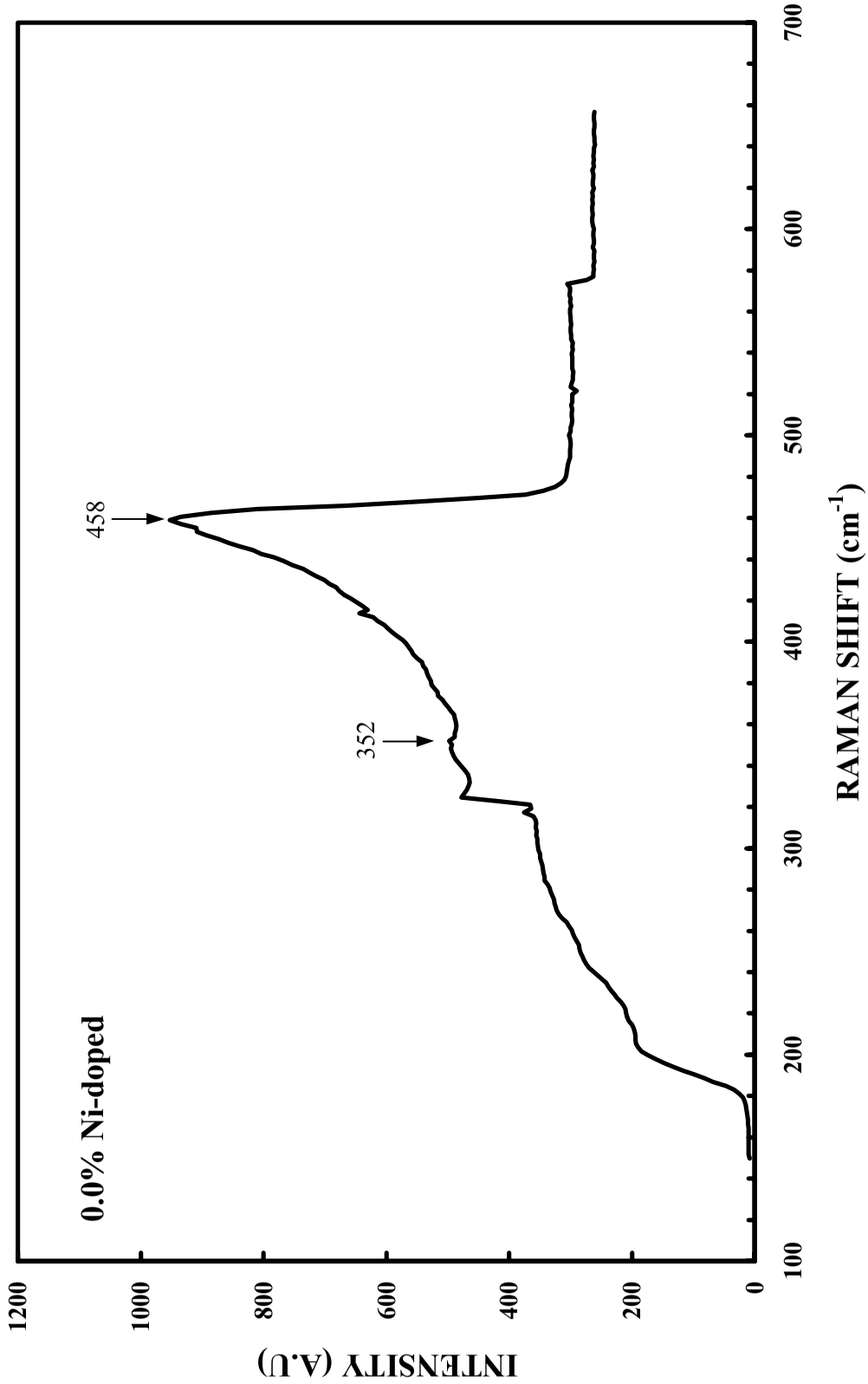

FIGURE 4-19. This is the Raman spectrum for $YBa_2(Cu_{1-x}Ni_x)_3O_{7-\delta}$ ($x = 0.0032$, $\delta = 0$).

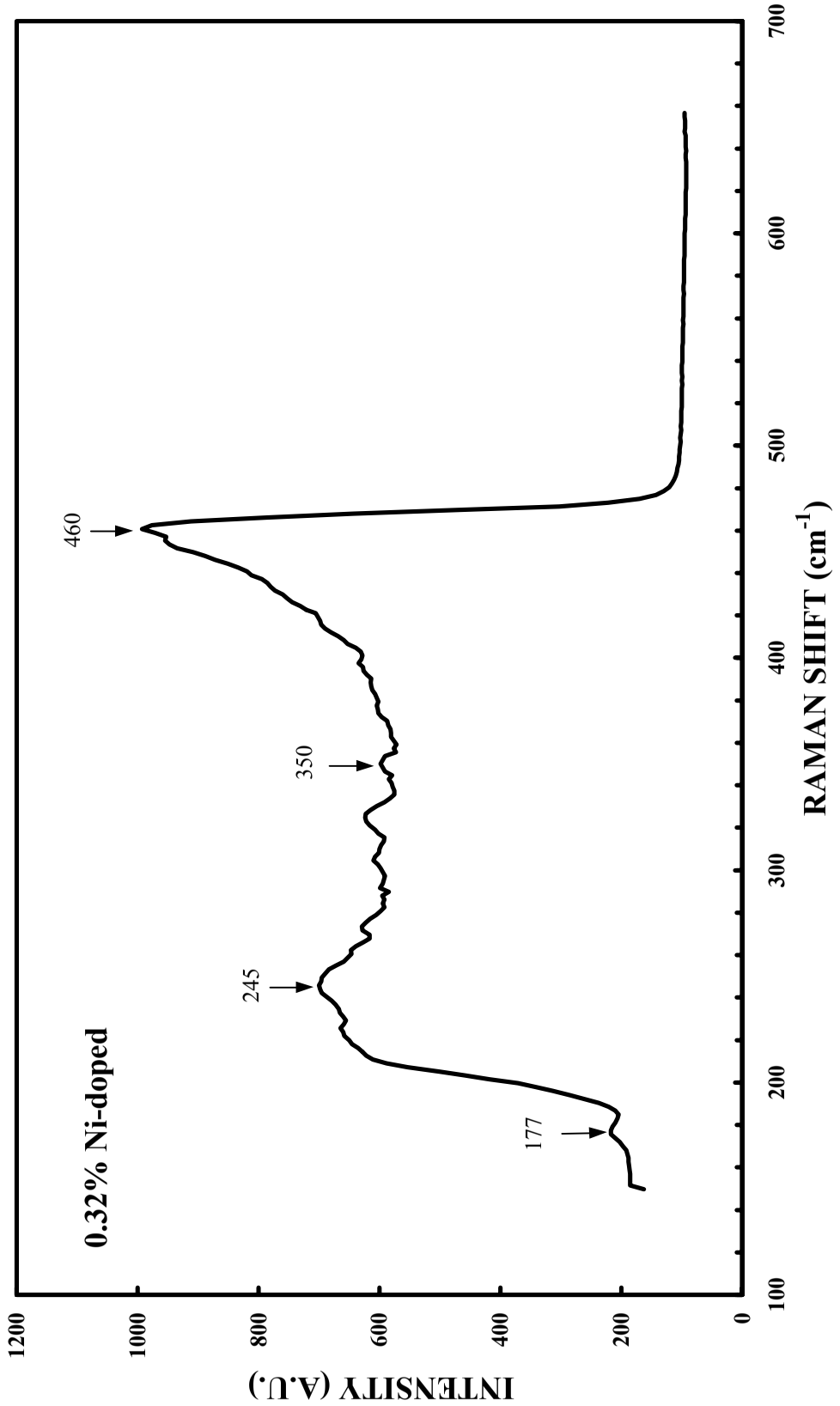

FIGURE 4-20. This is the Raman spectrum for $YBa_2(Cu_{1-x}Ni_x)_3O_{7-\delta}$ ($x = 0.0064$, $\delta = 0$).

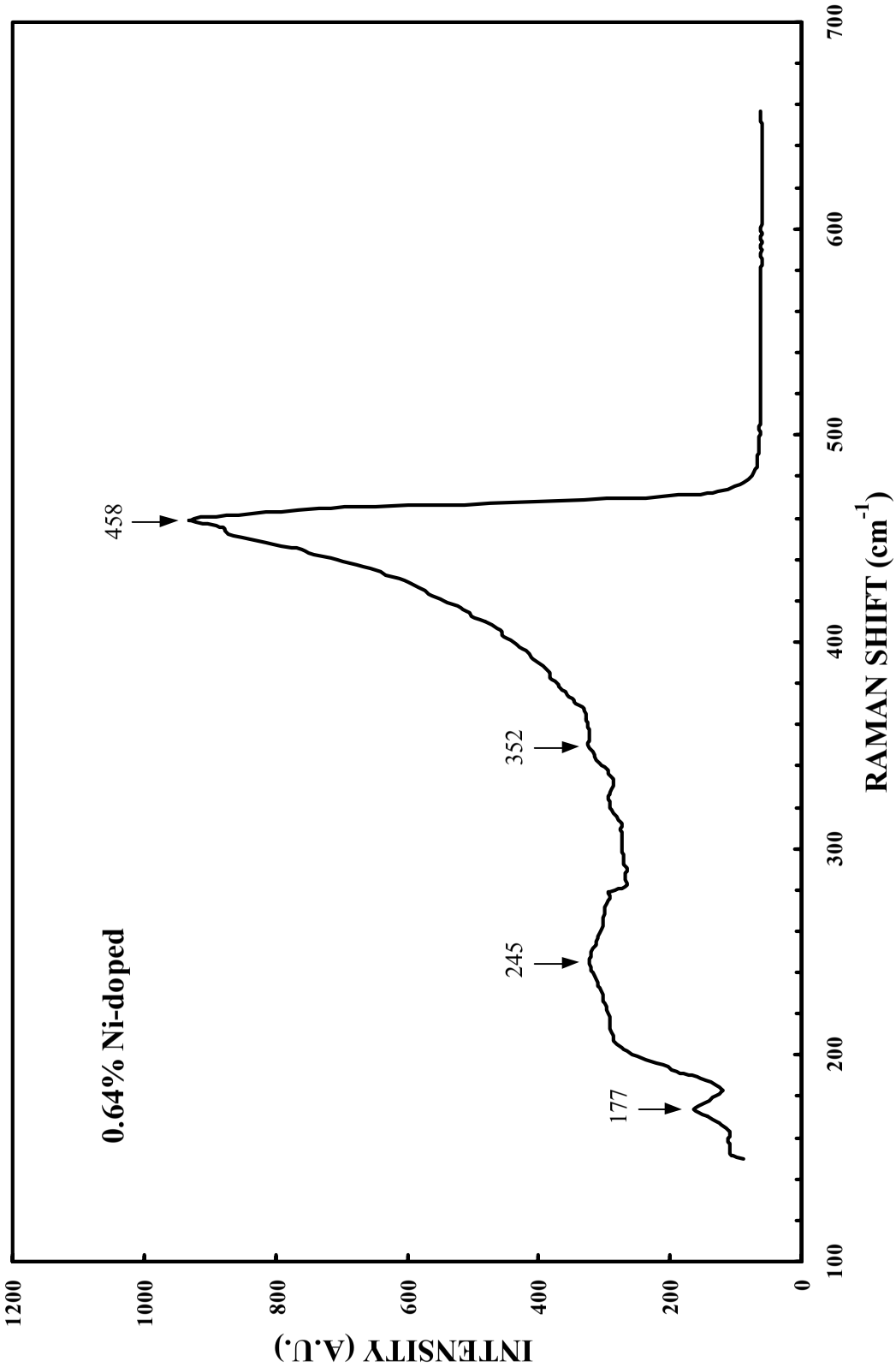

FIGURE 4-21. This is the Raman spectrum for $YBa_2(Cu_{1-x}Ni_x)_3O_{7-\delta}$ (x = 0.0096, δ = 0).

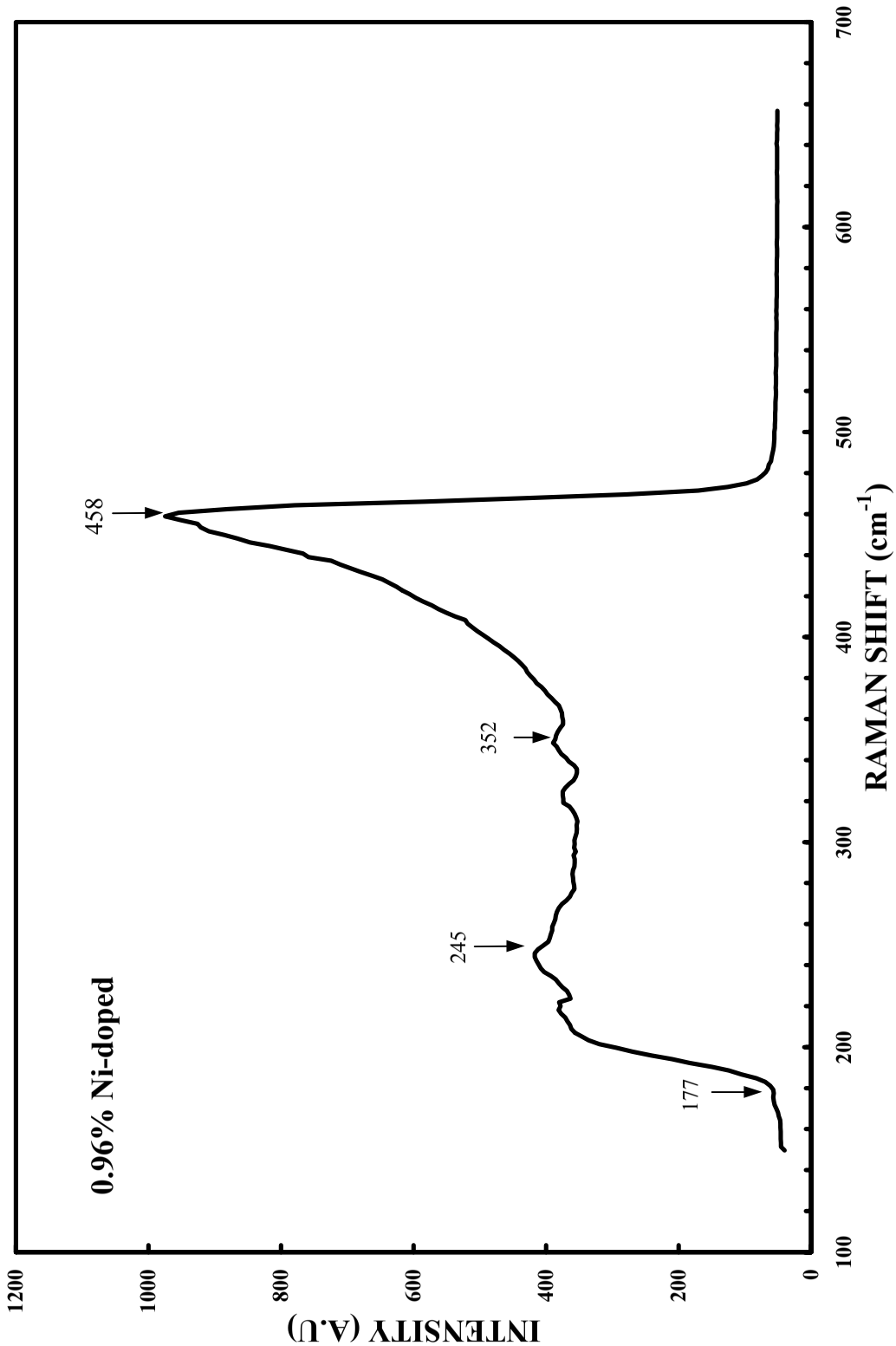

FIGURE 4-22. This is the Raman spectrum for $YBa_2(Cu_{1-x}Ni_x)_3O_{7-\delta}$ (x = 0.033, δ = 0).

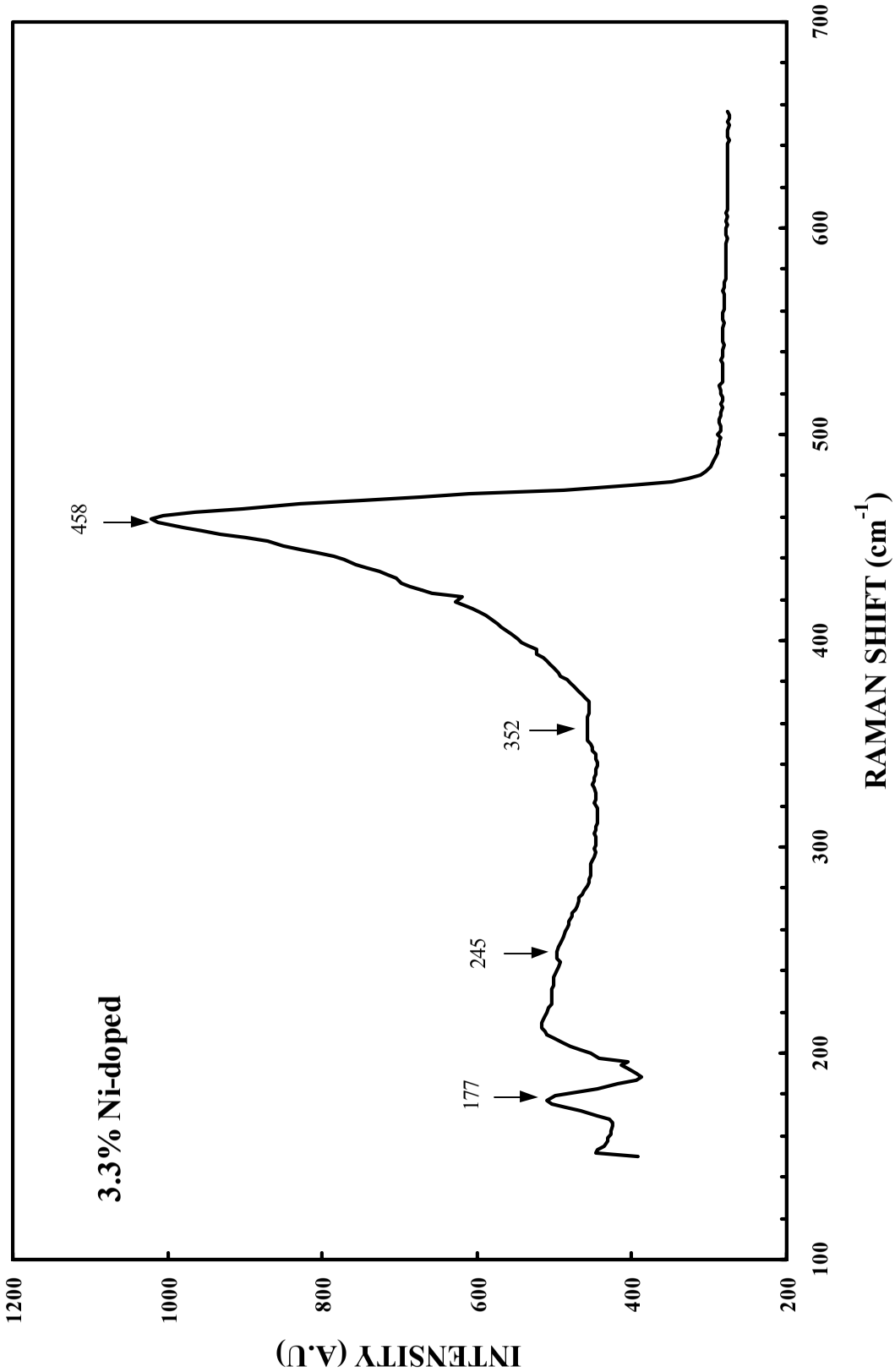

from the sharpness of the T_c and J_c transitions. Certainly, one can see the explicit contributions of nickel doping as compared to the pure Y-123 spectra. The Raman peaks at 460 cm^{-1} and 350 cm^{-1} are again the oxygen in-phase and out-of-phase modes associated with the CuO_2 planes in the pure Y-123. Liu *et al* [44] and others experimentally observed these lines as well at 330 and 440 cm^{-1}, when collecting spectra at room temperature. The theoretical and experimental work on the phonon frequencies and the eigenmodes have been published by a number of groups [44,49,50]. Specifically, at this first and lowest dopant level, the phonon at 350 cm^{-1} now seems to decrease in intensity, comparatively, and enhanced new peaks, not seen in the pure Y-123 material, now appear with even the lowest level of Ni doping. Obviously, the peak at 245 cm^{-1} can be identified as a vibrational mode associated with the Cu-O chain vibration as clearly shown in Figs 4-19 and 4-20, but not seen in the pure Y-123 material. The reason for its appearance in the spectra of the doped samples stems from the breakdown of the chain symmetry via nickel substitution for the copper at locations randomly selected by the nickel atoms in the Cu-O chains. This peak assignment is also borne out in the literature [36].

We also observed the appearance of a new peak at 177 cm^{-1} at $x = 0.0032$ that appeared for all values of x, the nickel dopant level. According to the theoretical and experimental analysis of the frequencies of Raman-active vibrational modes for YBCO as can be seen in Table 6, this peak is clearly not identified as any peak associated with YBCO. Yet it does correspond to the calculated peak for a Ni-O impurity, from Raman spectra tabulated in the literature for metal oxides [50], lending credence to our belief that not all of the nickel incorporates into the structure, especially at the higher dopant levels.

Rather, much of it shows up as a separate compound of Ni-O, most likely distributed throughout the sample at the grain boundaries. Furthermore, the peak at 177 cm^{-1} is enhanced in its relative size as the amount of Ni increases. From our own calculations based on the literature [51,52], this peak represents a Ni-O impurity mode of oscillation.

Because there were only negligible shifts in the vibrational modes at the higher x-values from the lower x-values, we can conclude that little Ni probably incorporated into the structure at the Cu sites. This becomes even more apparent at x = 0.033, as shown in Fig. 4-22, where this new Ni-O peak is strongly rising above the background, and likely large amounts of the doped nickel are located at the grain boundaries as a Ni-O impurity. With nickel breaking the symmetry at the chain sites, the chain modes of oscillation do indeed appear in all of the doped samples. Additionally, in most cases in the literature, there has been controversy about Raman features with frequencies less than 200 cm^{-1}, primarily due to the difficulty of obtaining signals in such close proximity to the laser line frequency. However, in our case, this spectral peak clearly appears only after Ni doping has taken place, lending credence to our belief that this is indeed a Ni-O phonon mode. It can be clearly noted that the x = 0.0032 Ni substituted sample has a Cu-O chain mode of oscillation that is larger in relative size than any of the other spectra. This would indicate that when nickel is first doped into the YBCO structure, that it at first preferentially substitutes into the chain sites, but that additional nickel doping simply results in increasing the amounts of Ni-O compound forming at the grain boundaries, and thus overshadowing the Cu-O chain substitutions that would have resulted in an enhancement of the superconducting in-field critical state current density, due to the ferromagnetic ordering of these chains.

TABLE 6. These are the experimental and calculated frequencies of Raman-active modes for YBCO below T_c.

Assignment	Ag			B_{2g}			B_{3g}		
	Exp.*	TEC**	LDC***	Exp.	TEC	LDC	Exp.	TEC	LDC
Ba	112	116	116	70	70	73	83	72	92
Cu	154	157	157	142	142	142	140	133	137
O out of phase	340	364	355	579	568	564	526	524	544
O in Phase	440	411	378	--	365	429	303	335	412
Bridging Oxygen	500	495	508	210	185	356	--	257	496

* Experimental Data : D.R. McCarty, J.Z. Liu, R.N. Shelton and H.B. RaDousky, Phys. Rev. B **41**, 8792(1990).

** The results of total-energy calculation (TEC) : R.E. Cohen, W.E. Pickett and H. Krakauer, Phys. Rev. Lett. **64**, 25751 (1990).

*** The Lattice-Dynamical Calculations (LDC) : W. Kress, U. Schroder, J. prade, A.D. Kulkarni and F.W. de Wette, Phys. Rev. B **38**, 2906(1988).

However, large amounts of Ni-O forming at the grain boundaries obviously cause a rapid degradation of the superconducting properties as the nickel doping level increases.

By comparison of all of the Raman spectra as shown in Fig. 4-23, the phonon peaks at 460 cm^{-1} and at 350 cm^{-1} for x = 0.0032 are observed to occur within ± 2 cm^{-1} of their position in all of the other samples, both in the doped samples and in the control sample, whose plane modes are observed at 458 cm^{-1} and 352 cm^{-1}. We can therefore assume that the substitution of nickel in $YBa_2Cu_3O_{7-\delta}$ has little or no effect on the plane modes of oscillation according to the Raman spectra obtained in our experiments, and thus that the nickel substitutes for copper preferentially in the chain sites rather than in the plane sites. For further information on the analysis of the Raman spectra, the reader should consult the M.S. Thesis by No Soung Myoung, May 2002, WIU Physics Department.

FIGURE 4-23. These are the Raman spectra for $YBa_2(Cu_{1-x}Ni_x)_3O_{7-\delta}$ at different concentrations x (at. %).

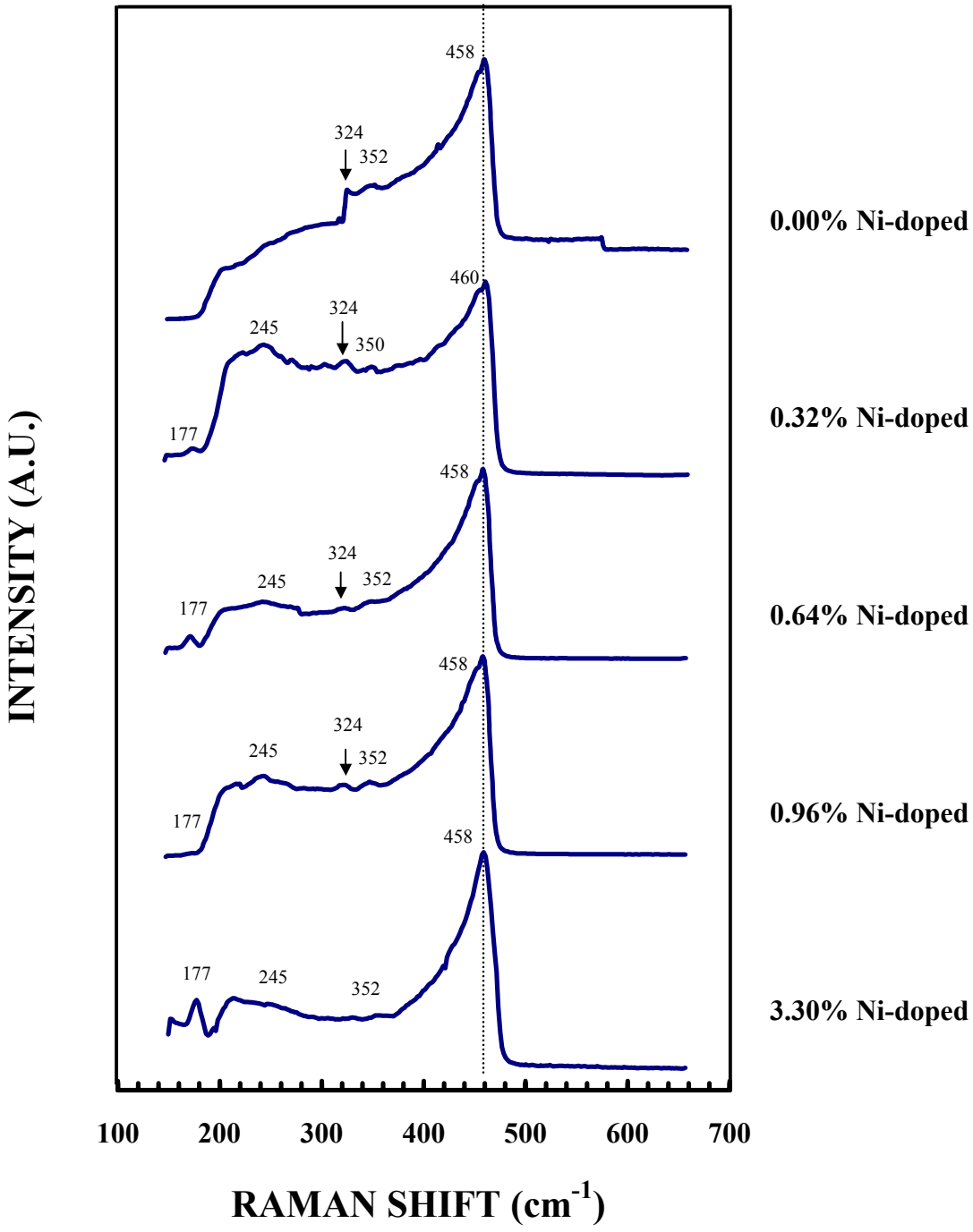

5. Conclusions

We have reported the observation of the optically active phonon modes in a pure YBCO and in low Ni-doped YBCO. The Cu-O chain vibrations in pure Y-123 cannot be observed by Raman scattering techniques due to odd parity. A chain mode does appear, however, in our doped samples, with a few Ni atoms replacing Cu atoms on the chains and destroying the symmetry that normally precludes their observation in pure YBCO. It can be concluded from our results that at very low-level concentrations of Ni-doping, the Ni is substituting into the Cu(1) chain sites. This substitution is most likely responsible for the enhancement in the in-field J_c, due to ferromagnetic ordering in the Cu-O chains with the Ni doping. Therefore, the relatively enhanced chain mode peak for x = 0.0032 is caused by nickel substitution, and the optimal enhancement of the in-field J_c for x = 0.0032 comes from this nickel substitution as well. However, as the amount of doped Ni increases, the nickel starts appearing at the grain boundaries as unreacted NiO, and the deteriorating effect of the NiO impurities on the critical current density overcomes the enhancing effect of the Ni in the Cu chain sites. This conclusion also sufficiently explains the degradation of the superconductivity for values of x greater than 0.0032, especially for x = 0.033. This conclusion is borne out by our observation of the Raman vibrational mode attributed to NiO at 177 cm^{-1}, as well as its growth in intensity with increasing dopant level.

The results of the EXAFS data collected from our samples were shown alongside a Fourier transform of raw data from an EXAFS experiment on NiO by Jose A. Rodriguez [53], who was using the same method of analysis as used for our Ni-doped samples. From Figs. 4-15 and 4-16, it was clear that the Ni appeared as an unreacted

impurity in the form of NiO in the $YBa_2(Cu_{1-x}Ni_x)_3O_{7-\delta}$ samples. The Ni-doped samples all share a peak at about 2.5 Å on their EXAFS Fourier transform graph, which is, by comparison, clearly a NiO peak. This peak corresponds to the peak at 2.6 Å in the Fourier transform graph of the NiO sample. The non-order of the graphs indicates that once Ni is doped into the YBCO, adding more Ni will not change the local atomic structure of the $YBa_2(Cu_{1-x}Ni_x)_3O_{7-\delta}$, but will only result in the formation of more impurity phases, which agrees with the results by Bridges *et al* [37]. Although it proved impossible to corroborate peak distances with Bridges *et al*, it should be noted in this connection that there was a large amount of noise in our EXAFS experimental results due to the extremely low-level Ni concentrations. The Ni-edge is at 8.333 keV, while the Cu-edge is at 8.979 keV, which made it impossible to fully measure the EXAFS normal spectral range, since oscillations from the Cu atoms would dominate over the Ni in the more extended energy range usually scanned in such experiments.

Thus, the results from both EXAFS and Raman spectroscopies are in agreement in terms of their explanation of low-level in-field J_c enhancement in YBCO due to Ni-doping. However, further studies in these areas will have to be done to determine the extent to which other ferromagnetic elements would produce similar enhancement effect in the in-field J_c. For example, in Fig. 4-15, there is an additional smaller peak in the 0.32% EXAFS spectra that does not appear in the other two spectra. This peak may correspond to the Ni substitution for Cu in the Cu(1) sites for the 0.32% sample, and for higher samples, this peak is diminished to nothing by the interference waves corresponding to NiO impurities, which would have larger peaks. This is definitely one observation that needs to be further investigated. Additionally, more theoretical

calculations will be necessary to determine the extent of the role that ferromagnetic ordering can play in such an enhancement of J_c in the presence of both weak and strong externally applied magnetic fields.

References

[1]. S. L. Cooper, D. Reznik, A. Kotz, M. A. Karlow, R. Liu, M. V. Klein, W. C. Lee, J. Giapintkis, D. M. Ginsberg, B. W. Veal, and A. P. Paulikas, Phys. Rev. B **47**, 8233 (1993).

[2]. H. Kamerlingh Onnes, Leiden Comm. **120b. 122b. 124c** (1911).

[3]. "High Temperature Superconductivity", ed. by Jeffrey W. Lynn, pp 4-6.

[4]. H. Frohlich, Proc. Royal. Soc. A **223**, 296 (1954).

[5]. E. Maxwell and C. E. Chase, Physica **24**, 5139 (1958).

[6]. M. K. Wu, J. R. Ashburn, C. J. Torng, P. H. Hor, R. L. Meng, L. Gao, Z. J. Huang, Y. Q. Wang, and C. W. Chu, Phys. Rev. Lett. **58**, 908–910 (1987).

[7]. "Introduction to Superconductivity"- 2nd Edition, Edited by Michale Tinkham, McGraw-Hill, Inc, pp. 44-46 (1996).

[8]. "Copper Oxide Superconductors" – Edited by Charles P. Pooler, Jr., Timir Datta, and Horacio A. Farach (A Wiley Interscience Publication) (1988).

[9]. "Quantum Physics of Atoms, Molecules, Solids, Nuclei, and Particles"- 2nd Edition, Robert Eisberg, and Robert Resnick, pp.484-487 (1985).

[10]. "Introduction to Superconductivity" – 2nd Edition, Michale Tinkham, McGraw-Hill, Inc., (1995).

[11]. "Introduction to Superconductivity" – Vol. **6**, A. C. Rose-Innes and E. H. Rhoderick, (1969).

[12]. Y. Yacoby, E. A. Stern. in *X-ray and inner-shell process: 17th international conference*, ed. R. L. Johnson, H. Schmidt-Böcking, B. F. Sonntag. 535-555 (1996).

[13]. B. K. Teo, in *Inorganic Chemistry Concepts*, **9**, ed. C. K. Jørgensen, M.F. Lappert, S. J. Lippard, J. L. Margrave, K. Niedenzu, H. Nöth, R. W. Parry, H. Yamatera. (1986).

[14]. E. A. Stern, in *X-Ray Absorption: Principles, Applications, Techniques of EXAFS, SEXAFS, and XANES*, ed. D. C. Koningsberger and R. Prins, *Chemical Analysis*, **92**, ed. J. D. Winefordner and I. M. Kolthoff. 3-51 (1988).

[15]. H. Fricke, Phys Rev. **16**, 202 (1920).

[16]. G. Hertz, Z. Phys. **3**, 19 (1920).

[17]. R. de L. Kronig, Z. Phys. **70**, 317 (1931).

[18]. E. A. Stern, Phys. Rev. B. **10**, 3027 (1974).

[19]. R. de L. Kronig, Z. Phys. **75**, 468 (1932).

[20]. H. Peterson, Z. Phys. **76**, 768 (1932); **80**, 258 (1933); **98**, 569 (1936).

[21]. A. I. Kostarev, Zh. Eksp. Teor. Fiz. **11**, 60 (1941); **19**, 413 (1949).

[22]. M. Sawada, Rep. Sci. Workshop Osada Univ. **7**, 1 (1959); T. Shiraiwa, T. Ishimura, and M. Sawada, J. Phys. Soc. Jpn. **12**, 788 (1957).

[23]. V. V. Schmidt, Bull. Acad. Sci. USSR, Phys. Ser. **25**, 998 (1961); **27**, 392 (1963).

[24]. D.E. Sayers, E.A. Stern, and F.W. Lytle, Phys. Rev. Lett. **27**, 1204 (1971).

[25]. F. W. Lytle, D. E. Sayers, and E. A. Stern, Phys. Rev. B **11**, 4825 (1975).

[26]. P. Eisenberger, B. Lincaid, S. Hunter, D. Sayers, E.A. Stern, and F. Lytle, in Proceedings of the IV International Conference on Vacuum Ultraviolet Radiation Physics, E. E. Koch, R. Haensel and C. Kunz (Eds.), Pergamon, Oxford, 1974, p. 806.

[27]. "Raman Spectroscopy for Catalysis", ed. by John M. Stencel, (1990).

[28]. Lei Wang and Shirshak K. Dhali, Supercond. Sci. Techol. **6**, 199-202 (1993).

[29]. "Magnetic Field Dependence of the Transport Critical Current Density in the Superconductor Family $ReBa_2Cu_3O_{7-x}$", a Thesis by Christopher M. Martin, Physics Department, Physical Sciences Library, WIU, pp.113-130 (1997).

[30]. Center for X-Ray Optics, Materials Sciences Division, E.O. Lawrence Berkeley National Lab. http://www-cxro.lbl.gov/optical_constants/filter2.html.

[31]. T. Ressler. WinXAS97v1.3 manual. (1998).

[32]. T. Ressler. WinXASv2 tutorial. (1998).

[33]. B. K. Teo and P. A. Lee, J. Am. Chem. Soc. **101**, 2815 (1979).

[34]. C. Thomsen, in "Light Scattering in High-Tc Superconductors", edited by M. Cardona and G. Guntherodt, Vol. **68** of Topics in Applied Physics (Springer, Berlin, 1991), pp. 285-359.

[35]. M. Limonov, D. Shantsev, and S. Tajima, Phys. Rev. B **65**, 24515 (2001).

[36]. C. C. Homes, D. A. Bonn, Ruixing Liang, and W. N. Hardy, Phys. Rev. B **60**, 9782 (1999).

[37]. F. Bridges, J. B. Boyce, T. Claeson, T. H. Geballe, and J. M. Tarascon, Phys. Rev. B **42**, 2137 (1990).

[38]. J. Essick, "Advanced LabView Labs", Prentice-Hall (1999).

[39]. Couach M. and Khoder A. F, in "Magnetic Susceptibility of Superconductors and other Spin Systems", ed. R. A. Hein, T. L. Francavilla, and D. H. Liebenberg, Plenum, New York pp. 35 (1992).

[40]. B. Jayaram, S. K. Agarwal, C. V. Rao, and A. V. Narlikar, Phys. Rev. B **38**, 2903 (1988).

[41]. F. Lytle, nio.359.Z, NIO IN DUCO CO FILT NI K EDGE 7 7 7-2-85. http://ixs.csrri.iit.edu/database/data/Farrel_Lytle_data/RAW/Ni/index.html.

[42]. D. N. Basov, A. V. Puchkov, R. A. Hughes, T. Strach, T. Preston, T. Timusk, D. A. Bonn, R. Liang, and W. N. Hardy, Phys. Rev. B **49,** 12165(1994).

[43]. S. A. Hoffman, M. A. Castro, G. C. Follis, and S. M. Durbin, Phys. Rev. B **49**, 12170 (1994).

[44]. R. S. Howland, T. H. Geballe, S. S. Laderman, A. Fischer-Colbrie, M. Scott, J. M. Tarascon, and P. Barboux, Phys. Rev. B **39**, 9017(1989).

[45]. R. Liu, C. Thomsen, W. Kress, M. Cardona, B. Gegenheimer, F. W. de Wette, J. Parade, A. D. Kulkarni, and U. Schroder, Phys. Rev. B **37**, 7971 (1988).

[46]. Altendorf, J. Chrzanowski, and J. C. Irwin, Phys. Rev. B **43**, 2771 (1991).

[47]. E. T. Heyen, R. Liu, C. Thomsen, R. Kremer, and M. Cardona, Phys. Rev. B **41**, 11058 (1990).

[48]. J. D. Jorgensen, B. W. Veal, W. K. Kwok, G. W. Crabtree, A. Umezawa, L. J. Nowicki, and A. P. Paulikas. Phys. Rev. B. **36**, 5731 (1987).

[49]. D. M. Krol, M. Stravola, W. Weber, L. F. Schneemayer, J. V. Waszczak, S. M. Zahurak, and S. G. Konsinski, Phys. Rev. B **36**, 8325 (1987).

[50]. D. Krillov, J. P. Collman, J. T. McDevitt, G. T. Yee, M. J. Holcomb, and J. Bozovic, Phys. Rev. B **37**, 3660 (1988).

[51]. R. E. Cohen, W. E. Pickett, and H. Krakauer, Phys. Rev. Lett. **64**, 25751 (1990).

[52]. W. Kress, U. Schroder, J. Prade, A. D. Kulkarni, and F. W. de Wette, Phys. Rev. B **38**, 2906 (1988).

[53]. Jose A. Rodriguez, Jonathan C. Hanson, Anatoly I. Frenkel, Jae Y. Kim, and Manuel Perez, J. Am. Chem. Soc. **124**, 9 (2002).

Appendix A. A Diagram the of LabView Program used for the Raman Scattering Measurements..

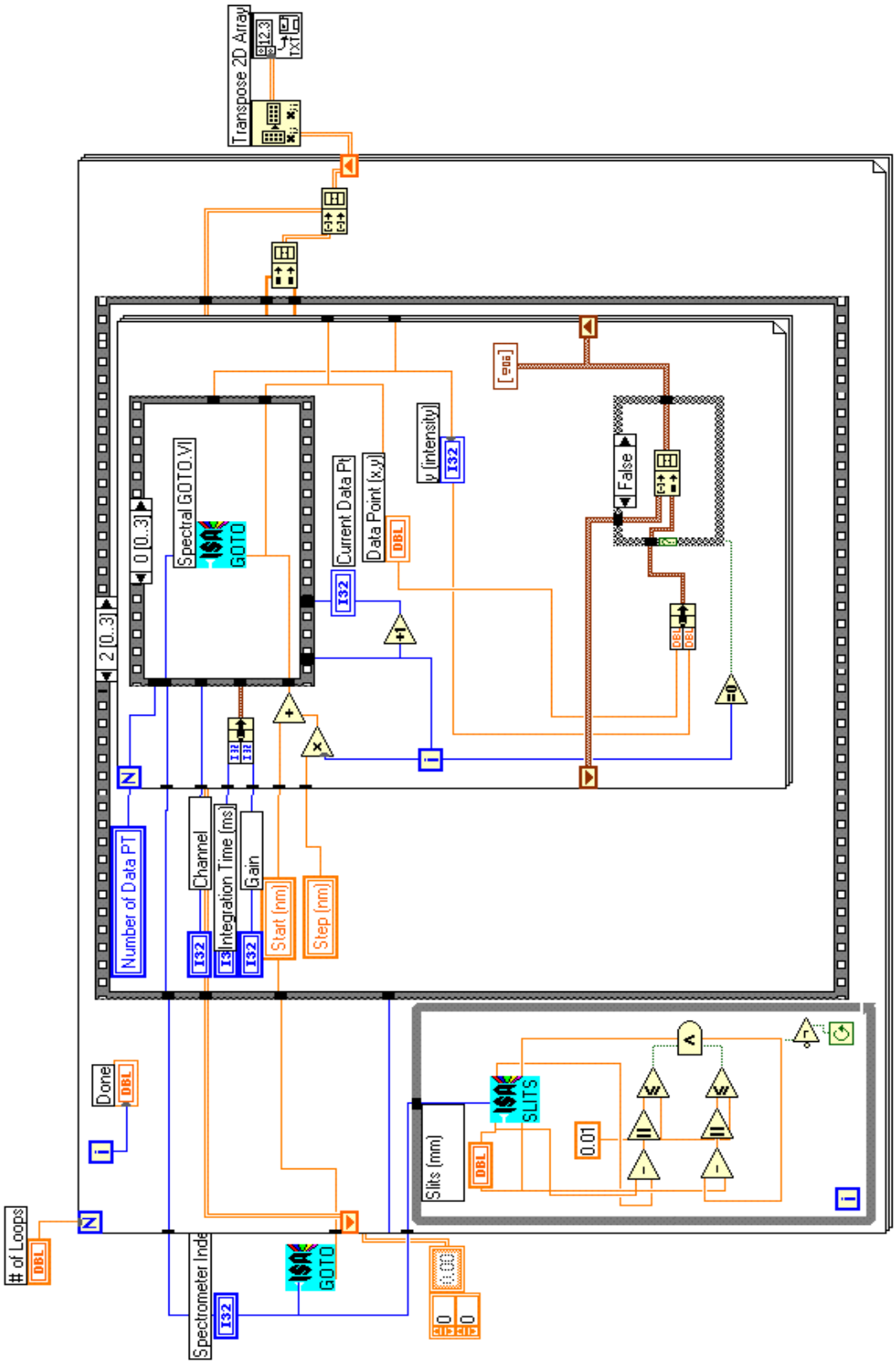

Acknowledgements

First and foremost, I would like to thank Dr. Mark S. Boley for his guidance and support over the past three years of this project. From dresses and liquid nitrogen to graduate school applications, I have always been able to look to Dr. Boley for knowledge and assistance, and for that I am thankful. I would also like to at this time extend my infinite gratitude to Mr. No Soung Myoung for making this thesis possible. No Soung's research of the literature of superconductivity and Raman spectroscopy as well as his analysis of the Raman spectra proved to be vital assets to the completion of this thesis.

I would like to thank several people for their assistance throughout the EXAFS experiments at Argonne; from UNI-CAT: Paul Zschack, Pete Jemian, Hawoong Hong, Jenia Karapetrova, and Curtis Benson; from COM-CAT: Steve Wasserman and Rachel Binyamin; and from MR-CAT: Holger Tostmann. In addition to these people, I would like to thank the Illinois Board of Higher Education (IBHE) and the EXCITE group for making the Argonne internship possible through their funding, and the Honors Council of the Illinois Region as well as the WIU Illinois Centennial Honors College for the grants provided to assist in the research at WIU. Finally, I would like to thank a variety of people who assisted me both technically and personally throughout my three years of research: Dr. Harold B. Hart, Daniel Pratt, Matthew Walker, Professor Doug Franklin, Won-Chul Shin, Daniel Johnson, Tom Boyle, Laurie Pichla, and Sybil Doran. Each of these people contributed assistance and advice throughout my undergraduate research, which were very beneficial to me.